Towards coupling a mechanical resonator to a superconducting flux-qubit

Itamar Holzman

Department of Physics

Ph.D. Thesis

Submitted to the Senate of Bar-Ilan University

Ramat-Gan, Israel October 2025

This work was carried out under the supervision of

Dr. Michael Stern

Department of Physics, Bar-Ilan University

Contents

List of Figures

List of Tables

Table of Acronyms

Acronym	Meaning	Acronym	Meaning
AC	Alternating current	RB	Randomized benchmarking
AFM	Atomic force microscope	RIE	Reactive ion etching
BAW	Bulk acoustic wave	RMS	Root mean square
CPW	Coplanar waveguide	RWA	Rotating wave approximation
DC	Direct current	SAW	Surface acoustic wave
FIB	Focused ion beam	SEM	Scanning electron microscope
FID	Free induction decay	SMP	Sub miniature push-on
GFQ	Gradiometer flux qubit	SOI	Silicon-on-insulator
HBAR	High-overtone bulk acoustic wave	SPAM	State preparation and measurement
HEMT	High Electron Mobility Transistor	SQUID	Superconducting quantum interference device
IR	Infrared	TWPA	Traveling wave parametric amplifier
IRB	Interleaved randomized benchmarking	USC	Ultra strong coupling
PCB	Printed circuit board	UV	Ultraviolet
QED	Quantum electrodynamics	VNA	Vector network analyzer
QPT	Quantum process tomography	ZPF	Zero-point fluctuation

Table of Key Variables

Variable	Description	unit
$\widetilde{\boldsymbol{C}}_{\boldsymbol{G}}$	Geometric capacitance matrix	F
$\widetilde{\boldsymbol{C}}_{\boldsymbol{J}}$	Junction capacitance matrix	F
$\hat{\boldsymbol{a}}^{\dagger}, \hat{\boldsymbol{a}}$	Creation and annihilation operators of microwave cavity	
$\hat{\boldsymbol{b}}^{\dagger}, \hat{\boldsymbol{b}}$	Creation and annihilation operators of mechanical resonator	
$\bar{\boldsymbol{n}}_{\boldsymbol{th}}$	Number of thermal photons	
$\hat{\boldsymbol{\sigma}}_{\boldsymbol{i}}$	Pauli operator i	
$\boldsymbol{\nabla}^{\mathbf{2}}$	Laplacian operator	
$\boldsymbol{\mathcal{H}}_{\mathbf{int}}$	Interaction Hamiltonian	J
$\boldsymbol{\mathcal{H}}_{\mathbf{int}}^{\mathbf{lin}}$	Linearized interaction Hamiltonian	J
$\mathbf{i}_{\boldsymbol{m}}$	Sequence of m Clifford operations	
$\boldsymbol{\mathcal{L}}_{\boldsymbol{k}}, \boldsymbol{\mathcal{L}}_{\boldsymbol{g}}$	Kinetic and geometric inductance per unit length	H/m
$\tan \boldsymbol{\delta}$	Loss tangent	
$\boldsymbol{\Gamma}_{\mathbf{1}}$	Relaxation rate	Hz
$\boldsymbol{\Gamma}_{\boldsymbol{2,E}}^{(\mathbf{2})}$	Second order Hahn-Echo decay rate	Hz
$\boldsymbol{\Gamma}_{\boldsymbol{2,E}}$	Hahn-Echo decay rate	Hz
$\boldsymbol{\Gamma}_{\boldsymbol{2,R}}$	Ramsey decay rate	Hz
$\boldsymbol{\Gamma}_{\mathbf{2}}$	Dephasing rate	Hz
$\boldsymbol{\Gamma}_{\boldsymbol{\phi}}$	Pure dephasing rate	Hz

$\boldsymbol{\Gamma_P}$	Purcell decay rate	Hz
$\boldsymbol{\Gamma_m}$	Damping rate of mechanical resonator	Hz
$\boldsymbol{\Gamma_\varphi^{\bar{n}}}$	Photon noise dephasing rate	Hz
$\boldsymbol{\Gamma_\varphi^C}$	Charge noise dephasing rate	Hz
$\boldsymbol{\Delta_d}$	Detuning between mechanical resonator and microwave cavity or qubit	rad/s
$\boldsymbol{\Lambda_{i_j,j}}$	Error channel	
$\boldsymbol{\Phi_0}$	Magnetic flux quantum	Wb
$\boldsymbol{\Phi_{ZPF}}$	Magnetic flux fluctuation due to x_{ZPF}	Wb
$\boldsymbol{\Phi_d}$	Differential flux of the GFQ, $\Phi_t - \Phi_b$	Wb
$\boldsymbol{\Phi_t}$ $(\boldsymbol{\Phi_b})$	Magnetic flux through the top (bottom) loop of the GFQ	Wb
$\boldsymbol{A^{\rightarrow}}$ $(\boldsymbol{A^{\leftarrow}})$	Forward (backward) traveling wave amplitude	$A/Hz^{1/2}$
$\boldsymbol{A_{eff}}$	Effective mode area	m^2
$\boldsymbol{B_{\parallel}, B_{\perp}}$	Parallel, perpendicular magnetic field	T
$\boldsymbol{B_{ext}}$	External magnetic field amplitude	T
$\boldsymbol{C_{i_j}}$	Clifford operation	
$\boldsymbol{C_J}$	Capacitance of a Josephson junction	F
$\boldsymbol{C_{ij}}$	Parasitic capacitances between superconducting islands	F
$\boldsymbol{C_n}$	Clifford group	
$\boldsymbol{C_q}$	Capacitance of qubit	F
$\boldsymbol{C_u}$ $(\boldsymbol{\mathcal{C}})$	Capacitance per unit cell (length)	F/m
$\boldsymbol{\hat{D}(\alpha)}$	Displacement operator, $e^{(\alpha\hat{a}^\dagger - \alpha^*\hat{a})}$	
$\boldsymbol{E_\psi}$	Positive operator-valued measure element for detecting the state ψ	
$\boldsymbol{E_C}$	Charging energy	GHz
$\boldsymbol{E_J}$	Josephson energy	GHz
$\boldsymbol{\hat{I}}$	Identity operator	
$\boldsymbol{I_0}$	Critical current of a Josephson junction	A
$\boldsymbol{I_{DC}}$	Direct current bias of the GFQ	A
$\boldsymbol{I_{DC}^{optimal}}$	Current bias at the optimal point of the GFQ	A
$\boldsymbol{I_c}$	Superconducting critical current	A
$\boldsymbol{I_p}$	Persistent current of the flux qubit	A
$\boldsymbol{J_m}$ / $\boldsymbol{I_m}$	Normal / modified Bessel functions	
$\boldsymbol{L_B}$	Length of Bragg filter segment	m
$\boldsymbol{L_u}$ $(\boldsymbol{\mathcal{L}})$	Inductance per unit cell (length)	H/m
$\boldsymbol{\hat{P}(\hat{a})}$	Parity operator, $e^{i\pi a^\dagger a}$	

P_i, P_j	Pauli operators	
Q_C	Quality factor of the resonator	
$Q_{clamping}$	Clamping quality factor	
Q_m	Quality factor of mechanical resonator	
Q_{tot}	Total quality factor	
R_n	Normal state resistance of Josephson junction	Ω
R_s	Sheet resistance	Ω
S_{i_m}	Noisy RB sequence	
$\hat{S}$	Schrieffer-Wolff transformation operator	
S_{21}	Transmission coefficient	
T_1	Relaxation time	s
T_2	Decoherence time	s
T_c	Superconducting critical temperature	K
U_0	Ground energy of mechanical resonator	J
U_b	Bending energy	J
V_{DC}	Direct current voltage	V
V_i	Electrostatic potential of the i-th superconducting island	V
Z_0	Characteristic impedance	Ω
Z_1, Z_2	Impedances of Bragg filter segments	Ω
Z_S	Scattering element impedance	Ω
Z_{eff}	Effective impedance of the Bragg filter	Ω
c_s	Transverse wave propagation speed	m/s
$f_{\rightarrow}(x, \omega)$	Spatial distribution function	
$f_E(t)$	Hahn-Echo decay function	
$f_R(t)$	Ramsey decay function	
$f_{m,n}$	Circular membrane resonance frequency of mode m, n	Hz
g_0	Single photon coupling strength	rad/s
g_x	Transverse coupling strength	rad/s
g_z	Longitudinal coupling strength	rad/s
i_j	Specific operation from i_m	
k_B	Boltzmann constant	J/K
m_{eff}	effective mode mass	Kg
$\bar{n}$	Average number of photons in a cavity	
n_j	Conjugate charge variable	

p_{i_m}	Survival probability	
p_{gate}	Depolarization parameter of the interleaved gate	
p_{ref}	Depolarization parameter of the entire IRB set	
$r_{\leftarrow}$ ($t_{\rightarrow}$)	Reflection (transmission) coefficient	
r_{gate}	Average error rate of the interleaved gate	
$r_{interface}$	reflection of an interface between different impedances	
t_{Bragg}	Transmission coefficient of the Bragg filter	
$t_{segment}$	Phase delay of a transmission line segment	
u_{ZPF}	Zero-point fluctuation of mechanical resonator	m
v_e	Speed of sound	m/s
v_{ph}	Phase velocity	m/s
x_{ZPF}	Amplitude of the zero-point motion of mechanical resonator	m
$\bar{\alpha}$	Average coherent drive amplitude	
α_T	Attenuation factor between different temperature stages	
β_n	Mechanical frequency parameter	
κ_C	Decay rate of the resonator	Hz
λ_B	Center frequency of the Bragg filter	m
λ_s	Shear wavelength	m
φ_{acc}	Accumulated phase during a round-trip in the resonator	rad
φ_i	Superconducting phase difference across the i-th Josephson junction	rad
ω_{IR}	Frequency cut-off	Hz
ω_c	Microwave cavity resonance frequency	rad/s
ω_{ge}	Transition frequency of the qubit	rad/s
ω_m	Mechanical resonator resonance frequency	rad/s
ω_n	Mechanical natural frequency of mode n	rad/s
ω_r	resonance frequency of the resonator	rad/s
E_Y	Young's modulus	Pa
$\mathcal{H}$	Hamiltonian	J
$\hbar$	Reduced Planck's constant	J·s
Γ	Damping rate	Hz
Δ	Minimal transition frequency of the qubit	rad/s
Φ	Magnetic flux	Wb
A	Cross section area of a beam	m^2
$C(u)$	Deflection dependent capacitance	F

$\boldsymbol{F(m)}$	Sequence fidelity	
$\boldsymbol{I}$	Moment of inertia	Kg·m^2
$\boldsymbol{I(x,t)}$	Current along transmission line	A
$\boldsymbol{K}$	Kerr constant	m/V^2
	Kinetic energy of a flux qubit	J
	Complete elliptic integral of the first kind	
$\boldsymbol{L}$	Inductance of microwave cavity	H
	Length of a beam	m
	Length of transmission line	m
$\boldsymbol{L(\Phi)}$	Magnetic flux dependent inductance	H
$\boldsymbol{M}$	Mutual inductance	H
$\boldsymbol{M(x,t)}$	Bending momentum	N·m
$\boldsymbol{P}$	Pressure	Bar
	Absolute to junction voltage transformation matrix	
$\boldsymbol{P(t)}$	State preservation probability	
$\boldsymbol{Q}$	Quality factor	
$\boldsymbol{R}$	Radius of circular membrane	m
$\boldsymbol{T}$	Temperature	K
$\boldsymbol{U}$	Potential energy of flux qubit	J
$\boldsymbol{V(x,t)}$	Voltage along transmission line	V
$\boldsymbol{c}$	Speed of light	m/s
$\boldsymbol{e}$	The electron charge	1.602×10^{-19} C
$\boldsymbol{f}$	Frequency	Hz
$\boldsymbol{g}$	Coupling strength	rad/s
$\boldsymbol{m}$ $\boldsymbol{(n)}$	Number of doublets (internal interfaces) in the Bragg filter	
$\boldsymbol{p}$	Depolarization parameter	
$\boldsymbol{r}$	Average error rate of the entire RB set	
$\boldsymbol{u(x,t)}$	Displacement of mechanical resonator	m
$\boldsymbol{w,h}$	width and height of a beam	m
$\boldsymbol{z}$	Normalized impedance, $\frac{Z_S}{Z_0}$	
$\boldsymbol{\alpha}$	Asymmetry parameter of Josephson junctions	
$\boldsymbol{\gamma}$	Mechanical mode shape scaling factor	
	Bragg filter enhancement factor	
$\boldsymbol{\delta\hat{a}}$	Vacuum fluctuations of coherent drive	

$\boldsymbol{\delta A}$	Area difference between the loops of the GFQ	m^2
$\boldsymbol{\delta I}$	Amplitude of current fluctuation in the resonator	A
$\boldsymbol{\theta}$	External magnetic field angle	rad
$\boldsymbol{\kappa}$	Decay rate of microwave cavity	Hz
	Wave number, ω/c	1/m
$\boldsymbol{\lambda}$	Center wavelength of microwave cavity	m
$\boldsymbol{\nu}$	Poisson's ratio	
$\boldsymbol{\rho}$	Density	Kg/m^3
$\boldsymbol{\tau}$	Mechanical resonator coherence time	s
	Round-trip time inside the resonator	s
$\boldsymbol{\chi}$	Dispersive coupling strength	rad/s
$\boldsymbol{\omega}$	Angular frequency	rad/s
$\boldsymbol{\epsilon}$	Electric permittivity	F/m
	GFQ's magnetic flux energy bias, $\frac{2I_p}{\hbar}\left(\Phi - \frac{\Phi_0}{2}\right)$	rad/s

Abstract

The exploration of macroscopic quantum phenomena is a compelling frontier in modern physics, driving both fundamental investigations into the nature of quantum mechanics and the development of novel quantum technologies. While superconducting qubits have emerged as a leading platform for quantum computing due to their fast operation and strong coupling to microwave fields, they face limitations such as short coherence times and crosstalk. Mechanical resonators, conversely, offer exceptional coherence properties, with coherence times reaching milliseconds. However, in most implementations their inherent linearity and weak coupling to external control fields present significant challenges. Hybrid quantum systems, which combine the complementary strengths of different physical platforms while mitigating their individual limitations, offer a promising solution to these challenges.

This thesisa a hybrid electromechanical quantum system where interaction is mediated by magnetic field quantum fluctuations. To maximize this interaction, we propose a coupling scheme that integrates gradiometer superconducting flux qubits with mechanical resonators. This approach circumvents some limitations of conventional optomechanical and electromechanical schemes by exploiting the enhanced flux sensitivity of flux qubits while leveraging mechanical resonators' exceptional coherence properties.

The work begins with the design and fabrication of high-quality mechanical resonators using both silicon membranes and diamond nanobeams. To effectively couple to these resonators, a gradiometer flux qubit was developed, as its design enables the application of a uniform magnetic field to enhance the coupling.

As the gradiometer qubit's design makes it insensitive to global external magnetic fields, it cannot be magnetically biased by an external coil. Therefore, we developed a Bragg-terminated resonator, which allows the application of a DC current for the generation of a local magnetic flux, thus enabling the magnetic flux biasing of the qubit.

The gradiometer flux qubits demonstrated quantum coherent operation with relaxation rated down to 33 kHz, and Hahn echo coherence rates down to 80 kHz at optimal

point. The primary limitation was identified as flux noise attributed to fabrication-induced contamination and direct transmission line coupling.

Quantum gate fidelities were characterized with randomized benchmarking, achieving average gate fidelities of 99.3%. Interleaved randomized benchmarking yield fidelity of 99.7% for $X_{\pi/2}$ gate.

1. Scientific Background

1.1 Quantum Behavior of Macroscopic Objects

The interpretation of quantum mechanics and its transition to the macroscopic world can be fundamentally reformulated into the question: "Can a macroscopic object be put in a quantum superposition?"[1] This question, first illustrated by Schrödinger's famous thought experiment in 1935, has evolved from philosophical speculation to experimental reality. While quantum mechanics traditionally describes microscopic phenomena[2] such as atoms, electrons, and photons, the exploration of quantum effects in macroscopic systems has emerged as a compelling frontier in modern physics[3–5]. In contrast to passively observing naturally occurring phenomena, the research field of macroscopic objects takes a proactive, engineering-driven approach. The primary motivation for this approach, and its most significant advantage over studies of natural quantum systems like atoms or molecules, is the prospect of control. Whereas the properties of an atom are fixed by nature, the parameters of an artificial macroscopic object—its resonance frequency, its coupling strength to other systems, its intrinsic nonlinearity, and its dissipative environment—can be precisely designed and fabricated using modern lithographic techniques. This design flexibility provides an unprecedented toolkit for both fundamental investigations into quantum mechanics and the development of novel quantum technologies.

To coax a macroscopic object, composed of billions of constituent atoms, into displaying its underlying quantum nature, two stringent prerequisites must be met. First, the temperature of the object, typically a resonator, must be tuned well below the characteristic energy scale defined by the resonance frequency: $k_B T \ll \hbar\omega$, where k_B is the Boltzmann constant, T is the temperature, $\hbar$ is the reduced Planck constant, and ω is the resonance frequency. This condition ensures that thermal fluctuations do not overwhelm the quantum nature of the system. Achieving this regime necessitates working at dilution refrigerator temperatures, typically in the millikelvin range (5-20 mK). Even at these extremely low temperatures, additional cooling strategies, such as sideband cooling and active feedback cooling, are often required to bring the macroscopic object to its quantum ground state. Second, the quality factor of the resonator is much greater than unity: $Q = \frac{\omega}{\Gamma} \gg 1$, where Γ is the damping rate. A high quality-factor ensures that the resonator can maintain its quantum coherence for

sufficiently long times to enable meaningful quantum operations and measurements. This requirement translates to minimizing all sources of energy dissipation and decoherence in the system along with careful engineering of the resonator materials, geometry, and coupling to the environment.

1.2 Superconducting Qubits

Among the different technologies, superconducting qubits have emerged as one of the leading platforms for near-term quantum computing applications, with major demonstrations of quantum advantage achieved using this technology[6–8]. Superconducting qubits are macroscopic electronic circuits fabricated from superconducting materials like aluminum or niobium, which exhibit quantum mechanical behavior when cooled to millikelvin temperatures. A critical component in these circuits is the Josephson junction, a tunnel barrier between two superconducting electrodes that introduces nonlinearity to the circuit without dissipation, effectively transforming classical harmonic oscillators into anharmonic quantum systems. The anharmonicity allows to isolate two distinct energy levels suitable for qubit operation. These systems are often referred to as "artificial atoms" because, unlike natural atoms with fixed properties, their quantum characteristics can be precisely engineered and controlled through circuit design parameters[9]. By adjusting the inductance, capacitance, and critical current of the Josephson junctions, researchers can tune fundamental properties of the "atom" such as the transition frequency between energy levels and the circuit's characteristic impedance, allowing for tailored performance for specific quantum computing applications.

The significant advantage offered by superconducting qubits is their strong coupling to microwave radiation, which enables fast and efficient quantum operations[10–12]. The large electric dipole moments inherent to these artificial atoms facilitate rapid gate operations, typically executed within nanoseconds, while simultaneously allowing for high-fidelity quantum state readout through dispersive coupling to microwave resonators. This strong microwave coupling also enables straightforward integration with conventional microwave electronics and control systems, providing a practical interface between the quantum processor and classical control infrastructure. Furthermore, the ability to coherently couple multiple qubits through shared microwave cavities or transmission line resonators forms the

foundation for scalable quantum architectures, where entangling operations and quantum information transfer can be efficiently mediated by the electromagnetic field modes. Indeed, recent advances have demonstrated processors exceeding 100 qubits, with Google's Willow[13] and China's Zuchongzhi 3.0[8].

Despite their advantages, superconducting qubits face several significant challenges that limit their current quantum computing applications[11,12]. Qubit lifetime remains a primary concern, as decoherence processes including relaxation (T_1) and dephasing (T_2) typically limit coherence times to tens of microseconds, constraining the depth of quantum circuits that can be executed before quantum information is lost to the environment. Cross-talk between neighboring qubits presents another major obstacle, as the strong coupling that enables fast gates can also lead to unwanted interactions and frequency shifts that reduce gate fidelities and complicate multi-qubit operations[11,14].

1.3 Mechanical Resonators

Mechanical resonators have emerged as a cornerstone technology for both advanced sensing and fundamental quantum physics. These versatile platforms bridge the classical and quantum regimes, providing tools for probing fundamental physics at the intersection of quantum mechanics and gravity[15–17]. Modern implementations, ranging from vibrating membranes to suspended beams, demonstrate remarkable performance with quality factors exceeding 10^9 at MHz to GHz frequencies, leading to quantum coherence times approaching 100 milliseconds—a significant leap beyond typical electromechanical systems[18].

These exceptional coherence properties enable a wide array of applications. For instance, resonators are coupled to superconducting qubits to achieve control over mechanical motion, enabling phonon-number-resolved measurements that extend quantum electrodynamics into new frequency regimes[19]. This has been shown with strong dispersive coupling between fluxonium superconducting qubits and mechanical oscillators at approximately 700 MHz, achieving coupling rates of $g \approx 2\pi \times 14$ MHz[15].

Moreover, these devices offer extraordinary force sensitivity, with resonant force noise spectral densities as low as 650 zN/Hz$^{1/2}$. This opens applications in fields such as magnetic resonance force microscopy, single molecule detection, and dark matter detection[18]. Beyond sensing applications, these resonators provide unique platforms for testing fundamental

physics theories, with their long lifetimes and large zero-point fluctuations making MHz-frequency drums excellent candidates for testing gravitational collapse phenomena postulated by Diósi-Penrose models and enabling tests of the boundary between classical and quantum physics, including constraints on continuous spontaneous localization[20].

In the context of quantum information processing, mechanical oscillators typically comprise micro- and nano-resonators with masses down to femtograms[19,21]. These resonators possess several characteristics that make them suitable for quantum applications. Their isolation from the environment results in high quality factors, enabling long coherence times essential for quantum state preservation[22]. The frequency range of these resonators spans from kilohertz to gigahertz, providing flexibility in system design and integration[19]. Additionally, their small physical dimensions allow for compact integration with other quantum components[23].

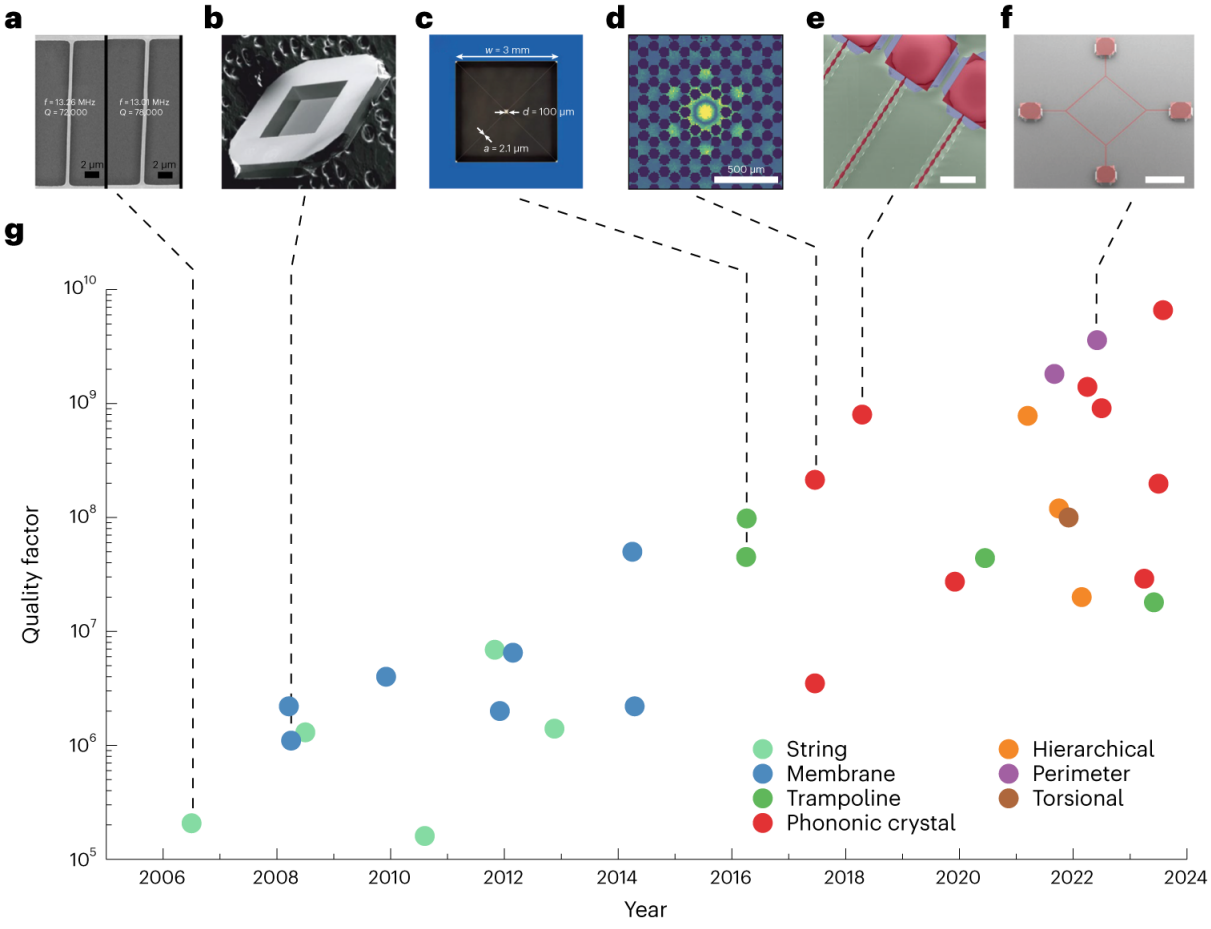

Figure 1 – Quality factor of different mechanical resonators over the years | The quality factor has doubled about every 14 months. Adapted from reference 22.

The performance of a mechanical oscillator is characterized by two fundamental parameters. The first is the coherence time τ, which is directly associated with thermal fluctuations and is

approximated by $\tau \approx \frac{\hbar}{k_B T} Q$, where Q is the quality factor of the resonator. The second is the $Q \times f$ product, where f is the mechanical resonance frequency, and this metric quantifies the resonator's energy storage capability.

For optimal performance in quantum applications, the condition $Q \times f > \frac{k_B T}{\hbar}$ (~10^{11} at 1K) must be fulfilled to overcome thermal decoherence with higher values indicating superior performance for quantum applications. A summary of recent experimental demonstrations that have achieved high $Q \times f$ systems can be found in Table 1.

Table 1 – Properties of various mechanical resonators

Resonator type	Material	f [Hz]	Q	$Q \times f$ [Hz]
Membrane[24]	AlGaAs	5.00×10^{6}	3.00×10^{5}	1.50×10^{12}
HBAR[25]	AlN/Al_2O_3	6.68×10^{9}	7.11×10^{5}	4.75×10^{15}
HBAR[26]	AlN/Al_2O_3	6.06×10^{9}	9.00×10^{5}	5.45×10^{15}
Cantilever[27]	Diamond	2.00×10^{6}	1.63×10^{5}	3.26×10^{11}
Nanobeam[28]	Diamond	5.76×10^{9}	4.40×10^{5}	2.53×10^{15}
Ring[29]	Diamond	2.97×10^{9}	4.29×10^{4}	1.27×10^{14}
Nanobeam[30]	GaP	2.80×10^{9}	4.18×10^{4}	1.17×10^{14}
Nanobeam[31]	$LiNbO_3$	1.80×10^{9}	1.70×10^{4}	3.06×10^{13}
Hierarchical[32]	Si_3N_4	1.07×10^{5}	7.80×10^{8}	8.35×10^{13}
Membrane[18]	Si_3N_4	1.49×10^{6}	1.50×10^{9}	2.23×10^{15}
Membrane[33]	Si_3N_4	1.14×10^{6}	1.09×10^{9}	1.24×10^{15}
Nanobeam[34]	Si_3N_4	1.10×10^{6}	2.00×10^{7}	2.20×10^{13}
Nanobeam[35]	Si_3N_4	1.33×10^{6}	8.00×10^{8}	1.06×10^{15}
Polygon-shaped[36]	Si_3N_4	3.50×10^{5}	3.60×10^{9}	1.26×10^{15}
Spiderweb[37]	Si_3N_4	1.34×10^{5}	1.82×10^{8}	2.44×10^{13}
Trampoline[38]	Si_3N_4	4.09×10^{4}	4.50×10^{6}	1.84×10^{11}
Nanobeam[39]	SiC	2.80×10^{5}	2.90×10^{6}	8.12×10^{11}
Trampoline[40]	Silicon	1.41×10^{5}	1.20×10^{6}	1.69×10^{11}
Nanobeam[41]	Silicon	5.00×10^{9}	4.92×10^{10}	2.46×10^{20}

Membrane[42]	Silicon	4.13×10^{6}	5.34×10^{6}	2.21×10^{13}
Nanobeam[43]	sSi	1.46×10^{6}	1.30×10^{10}	1.90×10^{16}

The isolation from the environment that enables high Q-factors simultaneously present challenges for controllability and readout of mechanical systems. The weak coupling to external fields necessitates sophisticated phonon-to-photon transducers which are usually lossy. Additionally, the intrinsic linearity of mechanical oscillators restricts their utility for quantum information processing.

To overcome these limitations, mechanical resonators can be coupled to other quantum systems in hybrid architectures[23]. These hybrid systems, that we will present in the following sections, combine the long coherence times of mechanical oscillators with the controllability and nonlinearity of other quantum platforms.

1.4 Hybrid Systems

The future of quantum computing will likely involve hybrid approaches that leverage the complementary strengths of different quantum platforms while mitigating their individual weaknesses[23,44–46].

Mechanical oscillators present compelling advantages for quantum information processing. As discussed previously, they offer exceptional coherence properties. Additionally, these mechanical resonators operate at MHz-GHz frequencies with micron-scale footprints, making them significantly more compact than alternative superconducting cavities in these range of frequencies.

However, mechanical systems face three key limitations. First, their MHz-range operation corresponds to energy scales of ~10^{-5} K, preventing passive cooling to the quantum ground state since cryogenic refrigerators typically reach only ~10^{-3} K. Second, the environmental isolation that preserves their superior coherence inherently limits coupling rates to external control systems, creating a fundamental trade-off between coherence and controllability. Third, mechanical oscillators have evenly spaced energy levels, preventing their direct use as qubits, which require anharmonicity to isolate specific two-level transitions.

Hybrid architecture offers promising solutions to these challenges. By coupling mechanical oscillators to more controllable quantum systems—through optical fields in optomechanical

schemes or electrical signals in electromechanical approaches—researchers can exploit their superior storage capabilities while circumventing their native limitations in control and nonlinearity.

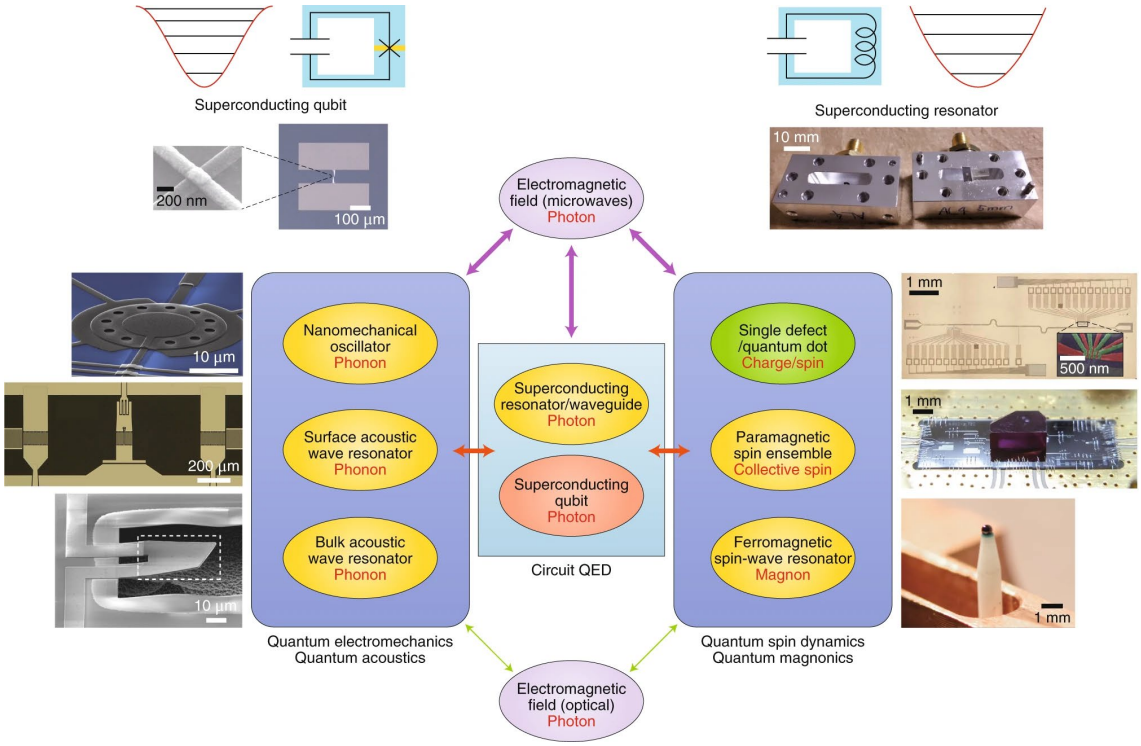

Figure 2 – Hybrid quantum systems | The schematics show the different paths to couple mechanical systems, such as nanomechanical, SAW or BAW resonators, to optical, microwave or spin systems. The figure was adopted from reference 45.

1.4.1 Quantum Optomechanics and Electromechanics

Quantum optomechanics and electromechanics constitute research fields investigating the interaction between electromagnetic radiation and mechanical motion at the quantum level[19]. These systems explore the coupling between electromagnetic radiation and nanomechanical or micromechanical motion, where a mechanical oscillator is coupled to a quantum harmonic oscillator associated with electromagnetic fields at optical or microwave frequencies through radiation pressure forces or electrostatic interactions. The quantum regime is achieved when the thermal energy scale $k_B T$ becomes comparable to or smaller than the mechanical resonance energy $\hbar\omega_m$, enabling the observation of quantum phenomena in macroscopic mechanical systems.

The theoretical frame work of cavity optomechanics is used to describe the coupling to optical photons while analogous physical principles apply to microwave and radio frequencies falls

under circuit quantum electrodynamics (cQED)[47]. For simplicity, we refer only to electromechanical systems, though the underlying physics applies equally to optical frequencies. The mechanical motion modulates the cavity resonance frequency, while intracavity photons exert radiation pressure forces on the mechanical element. For electromechanical systems, the coupling between mechanical displacement and microwave cavity modes occurs mainly through capacitive interaction. Both platforms enable investigation of quantum phenomena in mechanical systems, including ground state cooling[18,48–50], quantum state preparation[51,52], and entanglement generation[53,54].

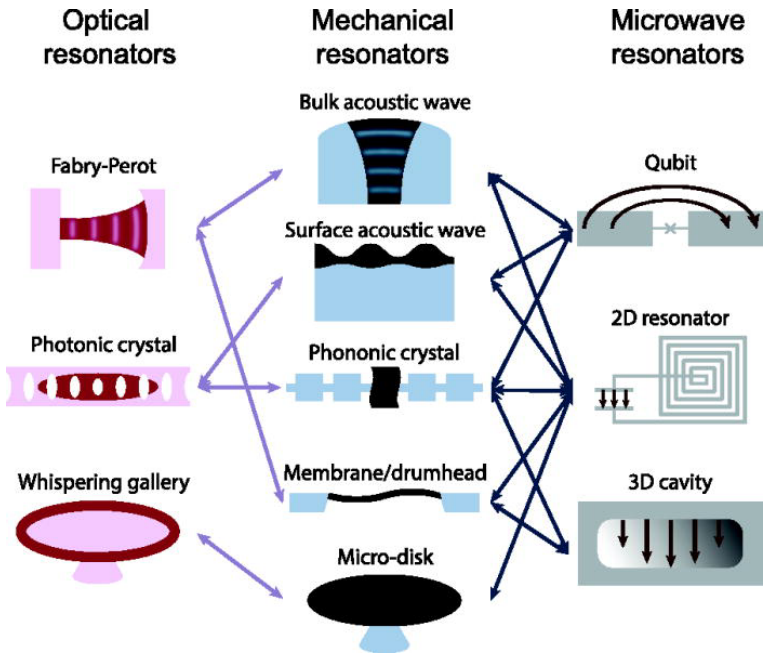

Figure 3 – Different experimental systems used for optomechanics and electromechanics demonstrations | The arrows indicate the achieved coupling. The image was adopted from reference 23.

The theoretical framework describing both optomechanical and electromechanical systems relies on similar Hamiltonians, differing primarily in the coupling mechanisms and frequency regimes. The electromechanical interaction is described by the Hamiltonian:

$$\mathcal{H} = \hbar\omega_c \hat{a}^\dagger \hat{a} + \hbar\omega_m \hat{b}^\dagger \hat{b} - \hbar g_0 \hat{a}^\dagger \hat{a}\left(\hat{b} + \hat{b}^\dagger\right) \quad (1)$$

where $\hat{a}$ and $\hat{b}$ represent the microwave and mechanical annihilation operators, respectively, ω_c is the microwave cavity frequency, ω_m is the mechanical frequency, and $g_0 \propto x_{ZPF}$ is the vacuum electromechanical coupling[19]. Here, x_{ZPF} is the amplitude of the zero-point motion of the mechanical resonator. The coupling term $-\hbar g_0 \hat{a}^\dagger \hat{a}\left(\hat{b} + \hat{b}^\dagger\right)$ describes how the photon number modulates the mechanical oscillator position and vice versa.

For coherent drive $\hat{a} = \bar{\alpha} + \delta\hat{a}$ the electromechanical interaction can be linearized when the cavity average drive amplitude $\bar{\alpha}$ significantly exceeds the vacuum fluctuations $\delta\hat{a}$. The interaction Hamiltonian takes the form:

$$\mathcal{H}_{int} = -\hbar g_0(\bar{\alpha} + \delta\hat{a})^{\dagger}(\bar{\alpha} + \delta\hat{a})\left(\hat{b} + \hat{b}^{\dagger}\right) \quad (2)$$

The term proportional to $|\bar{\alpha}|^2$ can be omitted by shift of the displacement's origin, and the term proportional to $\delta\hat{a}^{\dagger}\delta\hat{a}$ is negligible. Thus, the linearized interaction Hamiltonian becomes:

$$\mathcal{H}_{int}^{lin} = -\hbar g_0\sqrt{\bar{n}}(\delta\hat{a} + \delta\hat{a}^{\dagger})\left(\hat{b} + \hat{b}^{\dagger}\right) \quad (3)$$

with the electromechanical coupling strength defined as $g = g_0\sqrt{\bar{n}}$, and $\bar{n} = |\bar{\alpha}|^2$ is the average number of photons in the cavity. When the condition $\kappa \ll \omega_m$, where κ is the cavity decay rate, is satisfied, the modulation of the cavity frequency results with visible individual sidebands. In this so-called resolved sideband regime different terms in the interaction Hamiltonian are dominant, depending on the detuning $\Delta_d = \omega_c - \omega_m$. To make it clear, let us move to the interaction picture where $\delta\hat{a}(t) = \delta\hat{a}e^{-i\Delta_d t}$, $\hat{b}(t) = \hat{b}e^{-i\omega_m t}$ and the interaction Hamiltonian takes the form:

$$\mathcal{H}_{int}^{lin} = -\hbar g_0\sqrt{\bar{n}}\left[e^{-i(\Delta_d+\omega_m)t}\left(\delta\hat{a}^{\dagger}\hat{b} + \delta\hat{a}\hat{b}^{\dagger}\right) + e^{-i(\Delta_d-\omega_m)t}\left(\delta\hat{a}^{\dagger}\hat{b}^{\dagger} + \delta\hat{a}\hat{b}\right)\right] \quad (4)$$

In the red-detuned case, where $\Delta_d \approx -\omega_m$, provoking the rotating wave approximation (RWA) yields the "beam-splitter" interaction $\mathcal{H} = -\hbar g\left(\delta\hat{a}^{\dagger}\hat{b} + \delta\hat{a}\hat{b}^{\dagger}\right)$. This interaction enables the negatively detuned drive photons to scatter into the cavity's high-energy resonance, effectively cooling the mechanical resonator by transferring its thermal energy away[55]. For blue detuning, $\Delta_d \approx +\omega_m$, the RWA leads to the "two-mode squeezing" interaction $\mathcal{H} = -\hbar g\left(\delta\hat{a}^{\dagger}\hat{b}^{\dagger} + \delta\hat{a}\hat{b}\right)$, which is used for parametric amplification and to entangle the optical and the mechanical modes[54].

For electromechanical systems the coupling is usually capacitive. The vibrating element, such as a cantilever or a membrane, is incorporated in a capacitor C. The change in capacitance is translated to a change in the cavity frequency $\omega_c = \frac{1}{\sqrt{LC(u)}}$ with L the inductance of the cavity. The resulting single-photon coupling rate is $g_0 = \frac{\partial\omega_c}{\partial x}x_{ZPF}$. In the case of a capacitor made of parallel plates at distance d from each other, if $x_{ZPF} \ll d$, the capacitive response is given by $\left|\frac{\partial\omega_c}{\partial x}\right| \approx \frac{\omega_c}{2d}$ and the coupling is thus $g_0 = \frac{\omega_c}{2d}x_{ZPF}$.

Experimentally, $g_0/2\pi$ ranges from 10^0 – 10^2 Hz for both optical and microwave electromagnetic systems[18,48–51,53,54,56–58]. This weak coupling ($g_0 \ll \kappa, \Gamma_m$, where Γ_m is the mechanical damping rate) fundamentally limits the ability to generate non-Gaussian quantum states directly in the mechanical degree of freedom. To put these values in context, typical experimental parameters include cavity decay rates $\frac{\kappa}{2\pi}$ ranging from kHz to MHz, and mechanical quality factors $Q_m = \frac{\omega_m}{\Gamma_m}$ between 10^4 and 10^6, depending on the operating environment and device design[19].

Although coupling strength g can be enhanced by driving the cavity with many photons, this amplification strategy introduces fundamental limitations. In optical systems, intense laser drives cause unwanted heating that degrades the mechanical coherence and pushes the system away from the quantum regime. In microwave electromechanical systems, the coupling is typically capacitive, constrained by the physical dimensions of the coupling capacitor. Larger capacitors yield stronger coupling but result in lower mechanical frequencies, creating a fundamental trade-off between coupling strength and mechanical performance.

An alternative strategy employs magnetic coupling mechanisms to overcome these limitations[59]. The fundamental mechanism relies on the transduction of mechanical displacement into magnetic flux variations that modulates the inductance of a superconducting quantum interference device (SQUID) embedded within a microwave cavity. By making one arm of the SQUID's loop a free-standing beam (See Figure 4 for example) and applying a parallel magnetic field $B_{\parallel}$, the mechanical motion of the beam determines the magnetic flux threading the SQUID's loop resulting in a position-varying inductance of the resonator. This approach circumvents the geometric limitations inherent to capacitive coupling schemes and provides a pathway toward single-photon strong-coupling regimes.

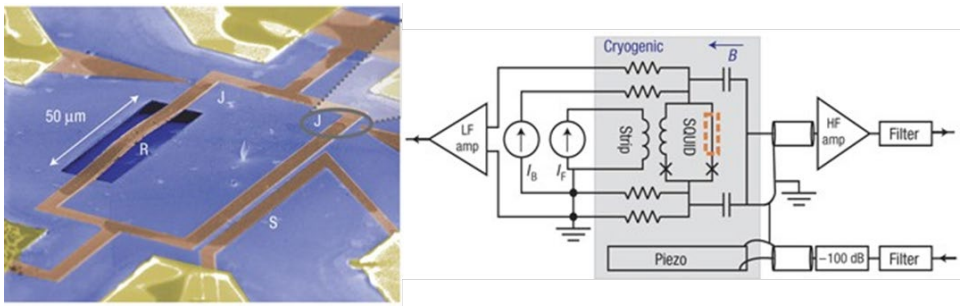

Figure 4 – Experimental realization of a superconducting quantum interference device (SQUID) with a free-standing arm embedded in an LC resonator | Left panel: colorized scanning electron microscope micrograph. The beam resonator (R),

Josephson junctions (J) and SQUID bias line (S) are shown in red. Right panel: Schematics of the measurement system with coupling magnetic field B applied parallel to the SQUID. Adopted from reference 60.

The theoretical model follows the optomechanics Hamiltonian, but with different single-photon coupling g_0. The resonance frequency of the microwave cavity is modulated by the flux-dependent inductance $\omega_c = \frac{1}{\sqrt{L(\Phi)C}}$. Consequently, the single-photon coupling becomes $\frac{\partial \omega_c}{\partial \Phi}\Phi_{ZPF}$, where $\frac{\partial \omega_c}{\partial \Phi}$ is the flux responsivity of the cavity and Φ_{ZPF} is the magnetic flux fluctuation induced in the SQUID due to zero-point fluctuations of the mechanical resonator. For a parallel magnetic field $B_{\parallel}$ acting on a SQUID with a vibrating beam of length L as an arm $\Phi_{ZPF} = \gamma B_{\parallel} L x_{ZPF}$, where γ is a scaling factor that depends on the mechanical mode shape. Hence, the single-photon coupling is $g_0 = \frac{\partial \omega_0}{\partial \Phi}\gamma B_{\parallel} L x_{ZPF}$. Reported values[61,62] in the range of $g_0/2\pi \approx$ kHz set an improvement of one order of magnitude compared to the capacitive coupling. However, these purely magnetic coupling mechanism, regardless of their strength, remain fundamentally linear interaction that preserve the Gaussian character of quantum states, thereby precluding the generation of exotic non-Gaussian mechanical states essential for advanced quantum information processing. Non-Gaussian states like cat states and squeezed states are essential because they provide quantum advantages that classical or Gaussian quantum states cannot achieve, enabling applications such as quantum computational advantage[63,64], and quantum sensing with improved precision[65,66]

Achieving single-photon ultra-strong coupling (USC), where the coupling strength is comparable to the system's resonant frequencies, can also unlock the ability to generate exotic quantum states, such as two-mode squeezed states, macroscopic "cat" states, and the photon blockade effect[67–69]. Yet, the fundamental obstacle to reaching USC is the inherently weak nature of radiation pressure coupling, which is further constrained by device geometry and material properties. Because achieving strong single-photon coupling through purely electromagnetic means is so difficult, a different approach is needed to create non-Gaussian mechanical states. A promising alternative involves coupling the mechanical oscillator to a nonlinear artificial atom. This method bypasses the limitations of linear electromagnetic coupling by using the artificial atom's anharmonicity to introduce the necessary nonlinearity for advanced quantum state engineering. The details of this hybrid approach will be discussed in the next section.

1.4.2 Coupling to Artificial Atoms

Following the limitations of the linear interaction discussed in the previous section, artificial atoms offer a fundamentally different approach to generating non-classical mechanical states. Unlike linear optomechanical interactions that preserve the Gaussian character of the coherent drive, the intrinsic anharmonicity of artificial atoms, i.e. superconducting qubits, enables direct access to non-Gaussian quantum states through nonlinear coupling mechanisms. The integration of artificial atoms with mechanical resonators constitutes an extension of cavity optomechanics where the mechanical element couples to a nonlinear superconducting qubit rather than a harmonic electromagnetic cavity.

The system Hamiltonian for the qubit-mechanical oscillator configuration is:

$$\mathcal{H} = \hbar\omega_m \hat{b}^\dagger \hat{b} + \hbar\frac{\Delta}{2}\hat{\sigma}_z + \hbar\left(\hat{b} + \hat{b}^\dagger\right)(g_x\hat{\sigma}_x + g_z\hat{\sigma}_z) \tag{5}$$

where ω_m represents the mechanical oscillator frequency, $\hat{b}$ and $\hat{b}^\dagger$ denote the mechanical mode annihilation and creation operators, respectively. The parameter Δ is the energy splitting between the two lowest energy levels of the superconducting qubit, and $\hat{\sigma}_{x,z}$ are the Pauli operators within the qubit subspace. The coupling term exhibits both transverse (g_x) and longitudinal (g_z) components, where the dominant coupling mechanism depends on the specific superconducting qubit implementation and the coupling scheme employed. For convenience we will denote the coupling strength g.

This Hamiltonian is formally equivalent to the cQED model, with the mechanical resonator substituting for the microwave cavity. Following established cQED analysis[47], the rotating wave approximation remains valid under typical experimental conditions[70] where $g \ll \omega_m, \Delta$. The rapidly oscillating, non-energy-conserving terms $\hat{b}\hat{\sigma}_-$ and $\hat{b}^\dagger\hat{\sigma}_+$ can be neglected, reducing the Hamiltonian to the Jaynes-Cummings form:

$$\mathcal{H} = \hbar\omega_m \hat{b}^\dagger \hat{b} + \hbar\frac{\Delta}{2}\hat{\sigma}_z + \hbar g\left(\hat{b}^\dagger\hat{\sigma}_- + \hat{b}\hat{\sigma}_+\right)$$

where g denotes the coupling strength and $\hat{\sigma}_-$, $\hat{\sigma}_+$ represent the qubit ladder operators.

For nanomechanical resonators coupled to superconducting qubits, the system typically operates in the dispersive regime, characterized by $g \ll \Delta_d$ where the detuning parameter is

defined as $\Delta_d = |\Delta - \omega_m|$. In this regime, the qubit and mechanical system are far detuned, preventing direct energy exchange while enabling measurements of the mechanical state[71].

The Jaynes-Cummings Hamiltonian can be diagonalized to first order in $\frac{g}{\Delta_d}$ through application of the Schrieffer-Wolff transformation[72]. By selecting the transformation operator $\hat{S} = -\frac{g}{\Delta_d}\left(\hat{b}^\dagger\hat{\sigma}_- - \hat{b}\hat{\sigma}_+\right)$ the effective Hamiltonian becomes:

$$\mathcal{H} = \hbar\omega_m\hat{b}^\dagger\hat{b} + \hbar\frac{\Delta}{2}\hat{\sigma}_z + \hbar\chi\left(\hat{b}^\dagger\hat{b} + \frac{1}{2}\right)\hat{\sigma}_z \quad (6)$$

where $\chi = \frac{g^2}{\Delta_d}$ represents the dispersive coupling strength. The resulting interaction term indicates that the qubit transition frequency depends linearly on the phonon occupation number of the mechanical resonator. This dispersive frequency shift has magnitude $\pm\frac{\chi}{2}$.

The coupling strength for charge-based mechanisms[73] is $g = \frac{x_{ZPF}V_{DC}}{C_q}\frac{\partial C}{\partial x}\frac{(2e)}{\hbar}$, where V_{DC} is the voltage applied to the mechanical resonator, C_q is the capacitance of the qubit, and $\frac{\partial C}{\partial x}$ is the position dependent qubit-mechanical resonator capacitance.

Most demonstrations employ electromechanical coupling where mechanical motion modulates the charge state of the qubit. For Cooper-pair box (CPB) qubits, mechanical displacement changes the gate capacitance, resulting in a charge-dependent coupling that is predominantly longitudinal (g_z coupling). A vibrating cantilever or membrane changes the capacitive coupling between the mechanical element and the qubit island, leading to coupling strengths on the order of 10 MHz depending on the applied gate voltage and device geometry.[71,74]

For transmon qubits, the coupling mechanism differs due to their charge-insensitive design. Transmons operate in the regime where the Josephson energy E_J significantly exceeds the charging energy E_C, reducing sensitivity to charge noise.[75] However, mechanical motion can still couple to transmons through modulation of the qubit transition frequency via capacitive interactions[76]. In transmon-based systems, the coupling is typically transverse (g_x coupling) rather than longitudinal with strength up to the order of 10^2 MHz.[77]

A different approach is to use piezoelectric coupling that utilizes strain-induced electric fields to couple mechanical motion to the qubit charge. The strain associated with acoustic waves

generates electric fields that couple to the qubit via capacitive interactions.[78] The coupling strength is proportional to $g \propto \frac{C_q}{C}\frac{e_{pz}}{\epsilon}\sqrt{\frac{1}{\rho v_e}}$, with e_{pz} the piezoelectric coupling, ϵ, ρ and v_e the substrate permittivity, density and speed of sound, respectively. The realization of such systems is via surface acoustic wave (SAW) and high-overtone bulk acoustic wave (HBAR) resonators fabricated on piezoelectric substrates such as lithium niobate ($LiNbO_3$) or gallium arsenide. These systems have shown coupling strength on the MHz range achieving the strong coupling regime[79,80]

Overall, coupling mechanical resonators to artificial atoms offers significant advantages over purely electromagnetic approaches. The intrinsic nonlinearity of superconducting qubits enables the storage of non-Gaussian quantum states, that remain inaccessible through linear optomechanical interactions, in the mechanical resonator. Experimental achievements include dispersive coupling with transmons and successful demonstrations of quantum state tomography[80], multi-phonon entanglement, and Fock state preparation[81]. However, fundamental limitations persist, including decoherence from thermal environments and finite mechanical quality factors.

1.4.3 Encoding a Qubit In a Cavity

A qubit can be encoded in the infinite Hilbert space of the quantum harmonic oscillators were the logical basis composed of superposition of coherent states also known as a 'cat state'[2]. This approach is advantageous because of the redundant encoding of information and the need for only a single ancilla qubit is to control the cavity state[82,83] and to detect the dominant error syndrome (a photon loss) in a quantum non-demolition measurement[84]. Yet, the scalability of microwave cavities is questionable due to their large physical dimensions. Recently a ‘cat-state’ was demonstrated in a high-overtone bulk acoustic-wave resonator (HBAR)[85], showing the potential use of compact mechanical “cats”.

The energy levels of the quantum mechanical oscillator are equidistant and therefore at first sight, it is not possible to specifically address two levels in the energy manifold. However, a qubit can be encoded in cavities with logical basis composed of superposition of coherent states also known as a 'cat state'[2]. In the following, we will explain briefly how such a qubit called a “cat state” can be formed in a cavity.

Let's introduce two operators acting on the cavity eigenstates, namely the displacement operator $\widehat{D}$ and the parity operator $\hat{P}$. The displacement operator $\widehat{D}(\alpha) = e^{(\alpha\hat{a}^\dagger - \alpha^*\hat{a})}$ is a unitary operator and its action is to map the ground state of the cavity to a state called coherent state $|\alpha\rangle = \widehat{D}(\alpha)|0\rangle$ which is an eigenvector of the annihilation operator a. The parity operator $\hat{P} = e^{i\pi a^\dagger a}$ is unitary ($\hat{P}^2 = \hat{I}$) and its action on a Fock state is given by $\hat{P}|n\rangle = (-1)^n|n\rangle$. Let's now consider a superposition of two coherent states of equal amplitude α and phase difference of π:

$$\left|\Psi_\alpha^\pm\right\rangle = \mathrm{N}_\alpha^\pm(|\alpha\rangle \pm |-\alpha\rangle) \approx \frac{1}{\sqrt{2}}(|\alpha\rangle \pm |-\alpha\rangle) \tag{7}$$

$$\mathrm{N}_\alpha^\pm = \left[2\left(1 \pm \mathrm{e}^{-2|\alpha|^2}\right)\right]^{-\frac{1}{2}}$$

The two states $\left|\Psi_\alpha^\pm\right\rangle$ are often referred as the 'even' and 'odd' π-cat-states. They are eigenstates of the parity operator $\hat{P}$ with different eigenvalue, namely $\hat{P}\left|\Psi_\alpha^\pm\right\rangle = \pm\left|\Psi_\alpha^\pm\right\rangle$ and thus, with parity measurement can distinguish between these two states. One method to prepare cat states is by introducing nonlinearities in the Hamiltonian of the resonator $\mathcal{H}_k = -K(\hat{a}^\dagger\hat{a})^2$. When a coherent state $|\alpha\rangle$ propagates through the Kerr medium, it evolves according to

$$|\Psi_\alpha(\tau)\rangle = e^{-\frac{|\alpha|^2}{2}}\sum_n \frac{\alpha^n}{\sqrt{n!}}e^{iKn^2\tau}|n\rangle \tag{8}$$

Consequently, after time interval $\tau = \frac{2\pi}{K}$ the system comes back to its initial state. However, after time intervals $\tau = \frac{\pi}{qK}$ a q-component cat state is generated. For example, if $q = 2$:

$$\left|\Psi_\alpha\left(\tau = \frac{\pi}{2K}\right)\right\rangle = e^{-\frac{|\alpha|^2}{2}}\sum_n \frac{\alpha^n}{\sqrt{n!}}e^{i\frac{\pi}{2}n^2}|n\rangle = \frac{1}{\sqrt{2}}\left(e^{i\frac{\pi}{4}}|\alpha\rangle + e^{-i\frac{\pi}{4}}|-\alpha\rangle\right) \tag{9}$$

An alternative route to create the desired cat states consists of using an ancilla qubit[86]. For example, a superconducting transmon qubit can be placed at the center of two 3D machined microwave cavities[87,88] as shown in Figure 5. One cavity is the quantum harmonic oscillator that stores the information, and the second cavity is used to manipulate and readout of the transmon. Transmission line antenna couples the qubit to the TE101 mode of the cavities.

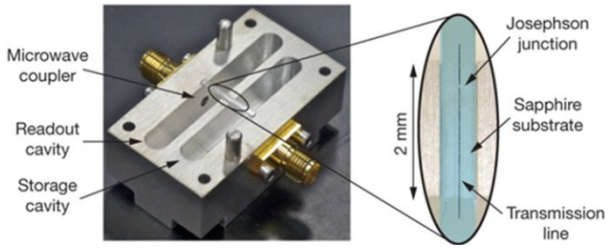

Figure 5 – Three-dimensional aluminum microwave cavities coupled to a superconducting transmon qubit | The coupling of the transmon to the cavities is via transmission line antennas. The figure is adopted from reference 88.

The Hamiltonian of the Josephson junction in the center of the transmon qubit is given by:

$$\mathcal{H} = -E_J \cos(\Phi) \tag{10}$$

with E_J the Josephson energy and Φ the magnetic flux threading the transmon. Excitations of the microwave modes cause current fluctuations in the Josephson junction that in turn are translated to fluctuations in the magnetic flux Φ. Consequently, the total magnetic flux is $\Phi = \Phi_{ZPF}^{q}(\hat{a}_q + \hat{a}_q^\dagger) + \Phi_{ZPF}^{s}(\hat{a}_s + \hat{a}_s^\dagger) + \Phi_{ZPF}^{r}(\hat{a}_r + \hat{a}_r^\dagger)$ with Φ_{ZPF}^{i} the magnetic flux fluctuation due to current fluctuation from element i and $\hat{a}_i^\dagger/\hat{a}_i$ the creation/annihilation operator of element i. The result Hamiltonian that describes the system is:

$$\mathcal{H} = -E_J \cos\left[\Phi_{ZPF}^{q}(\hat{a}_q + \hat{a}_q^\dagger) + \Phi_{ZPF}^{s}(\hat{a}_s + \hat{a}_s^\dagger) + \Phi_{ZPF}^{r}(\hat{a}_r + \hat{a}_r^\dagger)\right] \tag{11}$$

where Φ_{ZPF}^{i} is the magnetic flux change due to excitation in element i. The operators of the qubit and the storage and readout cavities are denoted with the subscripts "q", "s" and "r", respectively. By taking the Taylor expansion of the cosine term up to fourth order and omitting high-order and rotating terms the Hamiltonian becomes[88,89]:

$$\mathcal{H} = \hbar\omega_q \hat{a}_q^\dagger \hat{a}_q + \hbar\omega_s \hat{a}_s^\dagger \hat{a}_s + \hbar\omega_r \hat{a}_r^\dagger \hat{a}_r - \hat{b}^\dagger \hat{b}\left(\frac{\chi_{qs}}{2}\hat{a}_s^\dagger \hat{a}_s - \frac{\chi_{qr}}{2}\hat{a}_r^\dagger \hat{a}_r\right) - \frac{\chi_{sr}}{2}\hat{a}_s^\dagger \hat{a}_s \hat{a}_r^\dagger \hat{a}_r \tag{12}$$

The first three terms describe each element as a harmonic oscillator with resonance frequency ω_i. The last three terms are dispersive shifts χ_i of each element. During the interaction between the transmon qubit and the storage cavity the readout resonator is not populated $\left(\hat{a}_r^\dagger \hat{a}_r \approx 0\right)$. In addition, the transmon is considered as a two-level system, so the effective Hamiltonian is:

$$\mathcal{H} = \hbar\omega_q |e\rangle\langle e| + \left(\hbar\omega_s - \chi_{qs}|e\rangle\langle e|\right)\hat{a}_s^\dagger \hat{a}_s \tag{13}$$

In the off-resonance strong dispersive regime[90] the detuning Δ and coupling between the qubit and resonator g obey $\frac{g^2}{\Delta} > \max\left\{\frac{1}{T}, \Gamma, \kappa\right\}, g > \max\left\{\frac{1}{T}, \Gamma, \kappa\right\}$ with T the coherence time

of the qubit and Γ and κ the decay rate of the storage and readout cavities, respectively. In this regime the dispersive shift of the cavity resonance due to change in the qubit's state is larger than its width. If the qubit is in the ground/excited state and the resonance of the cavity differ by χ_{qs}. The qubit acts as a switch that allow signals at $\omega = \omega_s - \chi_{qs}$ to pass into the cavity only when in the excited state. It is controlled by pulses at frequency ω_q which do not affect the cavity because of the detuning. If we put the qubit in the superposition $\frac{|g\rangle+|e\rangle}{\sqrt{2}}$ and send signal at $\omega = \omega_s - \chi_{qs}$ the result state of the system is $|\Psi\rangle = \frac{|g,0\rangle+|e,\alpha\rangle}{\sqrt{2}}$. Applying a second π-pulse to the qubit yields the superposition $|\Psi\rangle = \frac{1}{2}(|g,0\rangle - |e,0\rangle + |e,\alpha\rangle + |g,\alpha\rangle)$, which after the measurement of the qubit in either $|g\rangle$ or $|e\rangle$ turns to:

$$|i\rangle = \frac{1}{\sqrt{2[1 \pm \exp(-|\alpha|^2/2)]}}(|\alpha\rangle \pm |0\rangle) \approx (|\alpha\rangle \pm |0\rangle)/\sqrt{2} \tag{14}$$

Lastly, we connect the storage cavity to a resonant source to displace the state:

$$\left|\Psi_f\right\rangle = \hat{D}(-\alpha/2)|\Psi\rangle = (|\alpha/2\rangle \pm |-\alpha/2\rangle)/\sqrt{2} \tag{15}$$

which is the desired π-phase cat. Indeed, the three-dimensional circuit QED architecture was used to deterministically encode cat states[91] and observe photon loss error syndromes[92].

The general form of the two-component cat state $|\Psi\rangle = c_0|\alpha\rangle + c_1|\alpha\rangle$ is not an eigenstate of the parity operator. Therefore, a more robust state is needed for the application of quantum error correction. The so-called cat code[83,84] exploits higher dimension of the cavity's Hilbert space and uses superposition of cat states as the computational basis:

$$|C_\alpha^\pm\rangle = N_\alpha^\pm(|\alpha\rangle \pm |-\alpha\rangle) \tag{16}$$

$$\left|C_{i\alpha}^\pm\right\rangle = N_\alpha^\pm(|i\alpha\rangle \pm |-i\alpha\rangle)$$

Let us define the logical $|0\rangle = |C_\alpha^+\rangle$ and $|1\rangle = |C_{i\alpha}^+\rangle$ and arbitrarily set the initial state to be $\left|\Psi_\alpha^0\right\rangle = c_0|C_\alpha^+\rangle + c_1|C_{i\alpha}^+\rangle$. We can now explore what happens in the case of photon loss:

$$\left|\Psi_{\alpha}^{1}\right\rangle \equiv a\left|\Psi_{\alpha}^{0}\right\rangle = \mathcal{N}_{\alpha}^{-}[c_0(|\alpha\rangle - |-\alpha\rangle) + ic_1(|i\alpha\rangle - |-i\alpha\rangle)] = c_0|C_{\alpha}^{-}\rangle + ic_1|C_{i\alpha}^{-}\rangle \quad (17)$$

$$\left|\Psi_{\alpha}^{2}\right\rangle \equiv a\left|\Psi_{\alpha}^{1}\right\rangle = \mathcal{N}_{\alpha}^{+}[c_0(|\alpha\rangle + |-\alpha\rangle) - c_1(|i\alpha\rangle + |-i\alpha\rangle)] = c_0|C_{\alpha}^{+}\rangle - c_1|C_{i\alpha}^{+}\rangle$$

$$\left|\Psi_{\alpha}^{3}\right\rangle \equiv a\left|\Psi_{\alpha}^{2}\right\rangle = \mathcal{N}_{\alpha}^{-}[c_0(|\alpha\rangle - |-\alpha\rangle) - ic_1(|i\alpha\rangle - |-i\alpha\rangle)] = c_0|C_{\alpha}^{-}\rangle - ic_1|C_{i\alpha}^{-}\rangle$$

$$a\left|\Psi_{\alpha}^{3}\right\rangle = N_{\alpha}^{+}[c_0(|\alpha\rangle + |-\alpha\rangle) + c_1(|i\alpha\rangle + |-i\alpha\rangle)] = \left|\Psi_{\alpha}^{1}\right\rangle$$

We have a closed set of states $\{|\Psi_{\alpha}^{n}\rangle\}$ under the operation of a, even with arbitrary c_0, c_1. In addition, the expectation value of the parity operator obeys $\langle\Psi_{\alpha}^{n}|\hat{P}|\Psi_{\alpha}^{n}\rangle = (-1)^n$. Thus, the sign of the parity measurement will change every time a single photon is lost, i.e. an error syndrome occurs. Finally, in the absence of photon jumps the states Ψ_{α}^{n} evolve deterministically according to $|\Psi_{\alpha}^{n}(t)\rangle = \left|\Psi^{n}_{\alpha e^{-\kappa t/2}}\right\rangle$, with κ the decay rate of the cavity. Overall, if the system is initialized at $\left|\Psi_{\alpha}^{0}\right\rangle$ and m jumps occur during time interval τ the final state will $\left|\Psi^{m \bmod 4}_{\alpha e^{-\kappa\tau/2}}\right\rangle$ is known. The information can then be decoded to the ancilla qubit, corrected, and re-encoded to the cavity. This scheme was implemented successfully[93] with the same 3D architecture mentioned before to demonstrate for the first time gainful quantum error correction.

In this chapter we showed the different ways mechanical oscillators are exploited for quantum information processing. When coupled to artificial atoms they can serve as a quantum memory with long lifetime, although strong single-phonon coupling is still a challenge. To overcome this limitation, we seek to combine the nonlinear capabilities of artificial atoms with the enhanced coupling strengths demonstrated in magnetic flux-mediated systems. As shown in previous sections, magnetic coupling schemes can achieve single-photon coupling rates, representing order-of-magnitude improvements over capacitive approaches. The next chapter presents the central goal of this thesis: to develop and demonstrate magnetic coupling between a superconducting flux qubit and mechanical resonators. Moreover, harmonic oscillators can be used for the generation of cat-state qubits. However, with microwave cavities, scalability is a major issue while mechanical cat-state only demonstrated recently. The proposal suggests that by swapping the microwave cavity for a mechanical cavity, our architecture would be capable of generating a mechanical cat-state.

2. Methodology

2.1 Introduction

Traditional approaches to quantum control of mechanical resonators rely on coupling to electromagnetic harmonic oscillators through optomechanical and electromechanical interactions. While these methods have enabled groundbreaking demonstrations of ground-state cooling and basic quantum state preparation, the coupling strengths achieved through radiation pressure and capacitive mechanisms remain inherently limited. Single-photon coupling rates g_0 typically reach only 10^0– 10^2 Hz, falling short of the strong coupling regime ($g_0 > \kappa$) necessary for efficient quantum control.

Magnetic coupling schemes have emerged as a promising solution to this fundamental limitation, offering enhanced coupling strengths through flux-mediated interactions. By embedding mechanical resonators within SQUIDs, researchers have demonstrated single-photon coupling rates reaching $g_0/2\pi \approx$ kHz[61,62], representing an order-of-magnitude improvement over conventional approaches. Yet, the magnetic coupling does not allow for the creation on non-Gaussian quantum states.

To transcend this limitation, coupling schemes involving nonlinear artificial atoms, specifically superconducting qubits, have been developed and demonstrated. The intrinsic anharmonicity of superconducting qubits enables the preparation of non-classical states including mechanical cat states[85], squeezed states[74], and multi-phonon Fock states[81].

We propose a novel approach that combines the enhanced coupling strengths of magnetic flux-mediated systems with the nonlinear capabilities of superconducting artificial atoms. Specifically, we present a methodology for coupling mechanical resonators, implemented as diamond nano-beams or silicon suspended membranes, to a superconducting flux qubit.

At the heart of our scheme is the superconducting flux qubit. This qubit offers superior sensitivity to magnetic flux variations compared to conventional SQUID, making it ideal candidates for detecting mechanical motion through flux-mediated interactions.

By positioning the mechanical resonator on one of the arms of the superconducting flux qubit loop, similar to the one detailed in section 1.4.1, the mechanical motion can alter the magnetic flux threading the loop if a parallel magnetic field is applied.

The enhanced sensitivity also presents significant experimental challenges. The control of flux qubit parameters requires precise control of the magnetic flux threading its loop, while the inherent flux sensitivity can result in environmental noise overwhelming the mechanical signal of interest.

To mitigate these challenges, we propose implementing the flux qubit in a gradiometer configuration. This design allows us to apply a strong, parallel magnetic field to increase the coupling between the qubit and the mechanical resonator. Crucially, the gradiometer geometry ensures this uniform field does not directly affect the qubit; instead, the qubit is only influenced by the localized magnetic flux changes produced by the mechanical motion of the resonator**.**

Previously, gradiometric flux qubits were developed to address the fabrication challenges inherent in flux qubits—where the energy gap depends exponentially on junction dimensions—enabling the realization of tunable gaps[94–97]. The gradiometric design eliminated crosstalk between gap tuning and energy bias control, both implemented via dedicated flux lines. While these gradiometric flux qubits demonstrated gap tunability across a GHz range and decay times of $T_1 = 1.5 - 150$ μs, their coherence times remained limited to and $T_2 = 65 - 300$ ns[95,96].

The gradiometer configuration can successfully enhance the coupling, yet it introduces a new challenge: the suppression of global magnetic field from external coils that are typically used to flux-bias the qubit to operate at the optimal point. To overcome this limitation, we implement a local biasing strategy that enables precise flux control while preserving the uniform field rejection properties of the gradiometer design.

Our proposed methodology incorporates the flux qubit within a carefully designed coplanar waveguide resonator architecture. The resonator is terminated by a Bragg filter on one end, which provides a notch filter around the resonance frequency of the qubits. The opposite end is shorted to ground, creating a well-defined boundary condition for the electromagnetic modes.

This resonator configuration serves dual purposes: it facilitates the application of precise DC magnetic bias fields required for optimal flux qubit operation, while simultaneously acting as a Purcell filter that removes unwanted microwave frequencies close to the qubit which could

otherwise degrade the system performance. The grounded termination provides a stable reference and enables the establishment of the necessary DC bias conditions.

The following sections detail the theoretical framework, device design principles, fabrication methodology, and experimental protocols necessary to realize this quantum platform.

2.2 Diamond Nano-beams

This chapter outlines the methodology employed for the fabrication and analysis of diamond nano-mechanical resonators.

2.2.1 Diamond as a Material Platform

The selection of single-crystal diamonds for fabricating nano-mechanical systems is motivated by a unique combination of superior material properties, despite notable fabrication and cost challenges.

Single-crystal diamond exhibits Young's modulus values of approximately E_Y = 1010 GPa, substantially exceeding silicon or silicon nitride as shown in Table 2. This high elastic modulus leads to increased E_Y/ρ ratio, with ρ the density, that enables the realization of mechanical resonators with frequencies extending into the gigahertz range[98]. The mechanical quality factors of diamond nano-beams[98,99,28] can exceed 10^4, with peak value of $Q_m = 1.2 \times 10^7$ for a nano beam embedded in a phononic crystal[100].

Table 2 – Mechanical properties of diamond, silicon, and silicon nitride

Material	Young's modulus [GPa]	Density [g/cm^3]	E_Y/ρ [GPa·cm^3/g]
Diamond	1010[101]	3.52	286.93
Silicon Nitride	362[102]	3.26	111.04
Silicon	130 ⟨100⟩ orientation, 169 ⟨110⟩ orientation[103]	2.33	68.67

Diamond also serves as an optimal substrate material for superconducting quantum circuits due to several key properties[104]. The chemical inertness of diamond allows for surface treatments that reduce contamination at the substrate-metal interface. This directly improves the coherence of superconducting qubits by mitigating dielectric loss, which primarily originates at these material interfaces.[105] Additionally, diamond exhibits high thermal conductivity, facilitating efficient thermalization of superconducting circuits.

2.2.2 Free-Standing Triangular Beams

The mechanical behavior of free-standing diamond nano-beams is analyzed using Euler-Bernoulli beam theory, which provides a description of flexural vibrations in structures where the beam length significantly exceeds the cross-sectional dimensions.[106] This theoretical framework enables prediction of resonance frequencies, mode shapes, and quality factors for different geometries. We focus on triangular cross-section beams due to considerations that are detailed in the Nano-Beam Fabrication section.

For small deflections relative to beam dimensions, the bending moment $M(x,t)$ relates to the beam curvature through:

$$M(x,t) = E_Y I \frac{\partial^2 u}{\partial x^2}(x,t) \tag{18}$$

where E_Y represents Young's modulus and I denotes the moment of inertia. The equation of motion for free vibrations, derived from Newton's second law, takes the form:

$$-E_Y I \frac{\partial^4 u}{\partial x^4}(x,t) = \rho A \frac{\partial^2 u}{\partial t^2}(x,t) \tag{19}$$

where A and ρ represent the cross-sectional area and mass density, respectively. Variable separation $u(x,t) = U(x)T(t)$ yields solutions for the spatial and temporal components of the beam motion.

For doubly-clamped beams of length L, the boundary conditions require zero displacement and slope at both ends: $u(0) = u(L) = u'(0) = u'(L) = 0$. These constraints reflect the rigid attachment of the beam to the substrate at both clamping points. The general solution for the position-dependent component becomes:

$$u_n(x) = C_n[\sinh \beta_n x - \sin \beta_n x + a_n(\cosh \beta_n x - \cos \beta_n x)] \tag{20}$$

with $a_n = \frac{\sinh \beta_n L - \sin \beta_n L}{\cos \beta_n L - \cosh \beta_n L}$. The frequency parameters β_n satisfy the transcendental equation $\cos \beta_n L \cdot \cosh \beta_n L = 1$, yielding $\beta_1 = 4.730, \beta_2 = 7.853$, and $\beta_3 = 10.996$ for the first three modes. Figure 6 shows the mode shapes corresponding to these first three vibration modes of a fully-clamped triangular diamond beam.

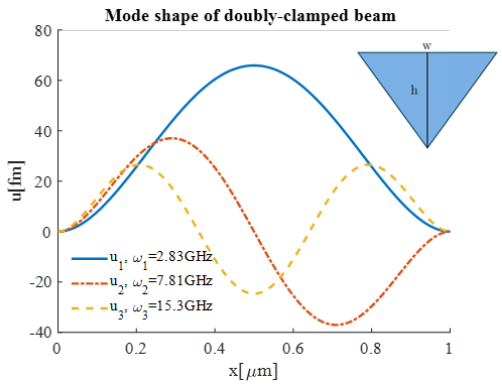

Figure 6 – Vibration modes of a fully-clamped triangular diamond beam | Analytic solution of the first three modes of a diamond beam with $w = h = 200\ nm$, $L = 1\ \mu m$, $E_Y = 1000\ GPa$ and $\rho = 3510\ \frac{kg}{m^3}$.

The temporal solution exhibits harmonic oscillation: $T_n(t) = \cos(\omega_n t)$, where the natural frequency of the nth mode is:

$$\omega_n = \frac{\beta_n^2}{L^2}\sqrt{\frac{E_Y I}{\rho A}} \tag{21}$$

For triangular cross-sections with width w and height h, the out-of-plane moment of inertia equals $I = \int_0^h y^2 dA = \frac{wh^3}{36}$.

Under high-vacuum and cryogenic conditions, the mechanical quality factor becomes limited by clamping losses arising from energy dissipation into the supporting substrate. The diamond substrate thickness significantly exceeds the shear wavelength $\lambda_s = \frac{c_s}{\omega_m} \approx 1\ \mu m$, where $c_s \approx 12\ \frac{km}{s}$ represents the transverse wave propagation speed in diamond. Under these conditions, the mechanical quality factor follows[107]:

$$Q_m = \frac{1}{\mathcal{A}}\frac{L}{w}\left(\frac{L}{h}\right)^4 \tag{22}$$

where $\mathcal{A} \approx 33.4$ represents a numerical coefficient weakly dependent on Poisson's ratio $\nu = 0.1$.

The design of optimal beam parameters involves competing requirements. High operational frequencies minimize thermal occupation, favoring short and wide beams, while high quality factors require long and narrow geometries. Resolution of this trade-off necessitates numerical analysis using finite element methods.

We employed COMSOL Multiphysics structural mechanics simulations of a model consisting of triangular beams with equal width and height, etched from cubic diamond substrates with dimensions comparable to the shear wavelength (Figure 7). Low-reflecting boundary conditions prevent spurious energy reflections, while the beam and surrounding regions are maintained under high vacuum ($P = 10^{-6}$ mbar). The simulations systematically vary beam length and width to analyze the out-of-plane vibrational modes.

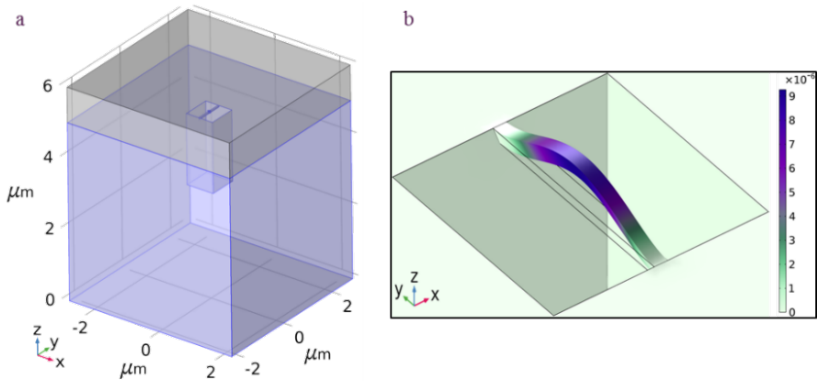

Figure 7 – COMSOL model | (a) Triangular diamond beam (purple) surrounded by high vacuum (grey). (b) Out-of-plane vibration mode shape. The color bar presents the displacement amplitude in arbitrary units determined by the simulation normalization.

Each simulation generates a spectral response normalized by the software. Extraction of zero-point fluctuations requires fitting the spectral response with Lorentzian functions and normalizing by the bending energy from the simulation to account for software normalization procedures. To do so we compare the simulated bending energy U_b to the resonator's ground energy $U_0 = \frac{\hbar\omega}{2}$. Both energies are proportional to the square of the displacement, hence the zero-point fluctuation is $u_{ZPF} = u\sqrt{U_0/U_b}$, with u the simulated displacement of the beam.

The analysis encompasses beams with widths $w \in [40\,\text{nm}, 60\,\text{nm}]$ and lengths $L \in [800\,\text{nm}, 1000\,\text{nm}]$. The corresponding resonance frequencies span 0.6 GHz to 1.2 GHz, in good agreement with the analytical solution given by Equation 21. The quality factors range from 20,000 to 300,000, not far from the prediction from clamping losses (see Equation 22). A representative result is shown in Figure 8a.

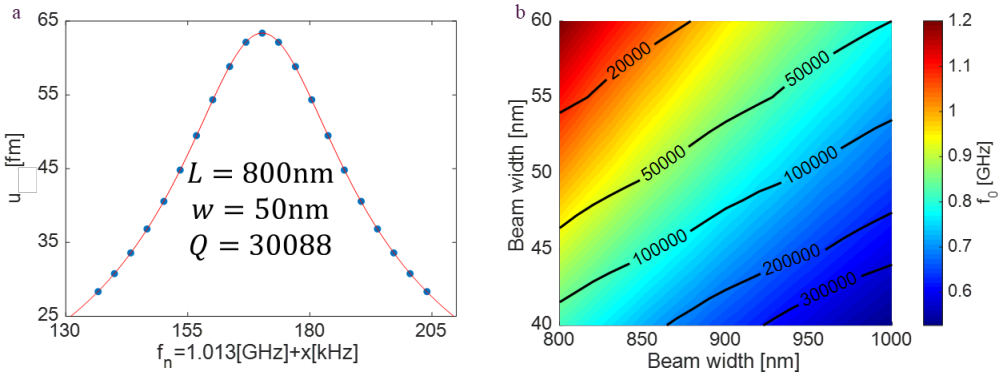

Figure 8 – COMSOL simulations results | (a) Simulated and re-normalized spectral response (blue dots) of an 800 nm long and 50 nm wide diamond beam with a Lorentzian fit (solid red line). The out-of-plane resonance frequency is $\omega_n/2\pi = 1.013\ GHz$ and the quality factor of the mode is $Q = 30{,}088$. (b) Color map of the resonance frequency of beams with different dimensions. The contour lines are the quality factor of the out-of-plane vibration mode

Figure 8b presents a color map of the simulated resonance frequency for beams with different dimensions, with contour lines indicating the quality factor of the out-of-plane vibration mode.

2.3 Silicon Membrane

This section examines silicon as a platform for suspended membranes. We analyze the material properties that make silicon suitable for micromechanical applications, and discuss the theoretical models used to predict their mechanical response.

2.3.1 Silicon as a Material Platform

As shown in Table 2, silicon demonstrates directionally dependent elastic properties, with Young's modulus values varying between 130 GPa in the ⟨100⟩ orientation and 169 GPa in the ⟨110⟩ direction[103]. This crystallographic anisotropy allows optimization of the mechanical performance through strategic device orientation.

Silicon on Insulator (SOI) is a semiconductor substrate technology that consists of a thin silicon device layer separated from the bulk silicon substrate by an insulating layer, typically silicon dioxide (SiO_2)[108]. One particularly relevant application of SOI technology is in the fabrication of silicon membranes. In this process, the buried oxide layer serves as a sacrificial layer that can be selectively etched away using hydrofluoric acid (HF) or other appropriate etchants, leaving behind a free-standing silicon membrane from the top device layer. The ability to use the insulating layer as a sacrificial layer provides an additional degree of structural control.

The resonance frequency of silicon mechanical resonators[109] is usually in the order of 1-100 MHz with quality factors above 10^4. Record quality factors above 10^6, at MHz frequencies, were achieved using square plate Lamé-mode resonator[42,110].

In this work, we focus on silicon membranes that can be coupled with a superconducting flux qubit. The coupling mechanism will be discussed later. Below, we overview the mechanical behavior of silicon membranes.

2.3.2 Mechanics of Circular Membranes

Membranes are two-dimensional structures characterized by thickness much smaller than their lateral dimensions. For circular membranes with radius R and mass density ρ, the dynamic behavior follows the Kirchhoff-Love plate equation[111]

$$\nabla^4 w + \frac{12(1-\nu^2)}{E_Y h^2}\rho\frac{\partial^2 w}{\partial^2 t} = 0 \tag{23}$$

where $w(r,\theta,t)$ represents the transverse displacement, E_Y is Young's modulus, ν is Poisson's ratio, and h is the membrane thickness. The operator ∇^2 denotes the Laplacian in polar coordinates.

The solution to equation 23 yields the mode shapes for a clamped circular membrane:

$$w_{m,n}(r,\theta,t) = C_{m,n}\left[J_m(\gamma_{m,n}r) - \frac{J_m(\gamma_{m,n}R)}{I_m(\gamma_{m,n}R)}I_m(\gamma_{m,n}r)\right][\cos(m\theta)+\sin(m\theta)]e^{i\omega t} \tag{24}$$

Here, J_m and I_m are the normal and modified Bessel functions, respectively. The first few values of the quantized parameter are: $\gamma_{0,1}R = 3.19622, \gamma_{1,1}R = 4.61090$, $\gamma_{2,1}R = 5.90568, \gamma_{0,2}R = 6.30644$. The vibrational modes are characterized by two integer indices (*m*, *n*) that define the spatial oscillation pattern. Angular index *m* determines the number of nodal diameters (radial lines where displacement equals zero) while the radial index *n* corresponds to the number of nodal circles, determined by the *n*-th root of the Bessel functions.

For a thin plate with thickness $h \ll R$, the mode eigenfrequencies are:

$$f_{m,n} = \frac{(\gamma_{m,n}R)^2}{2\pi R^2}\sqrt{\frac{E_Y}{12\rho(1-\nu^2)}}h \tag{25}$$

The effective mass of each vibrational mode is given by $m_{eff} = \rho t A_{eff}$, where the effective area is $A_{eff} = 2\pi \int_0^R w_{m,n}(r)dr$. For the fundamental mode (0,1), the ratio $\frac{A_{eff}}{\pi R^2} = 0.3289$.

The zero-point fluctuation amplitude, critical for the coupling mechanism that will be presented later, is $u_{ZPF} = \sqrt{\hbar/4\pi m_{eff} f_{m,n}}$.

The total quality factor of a vibrating membrane results from multiple loss mechanisms:

$$\frac{1}{Q_{tot}} = \frac{1}{Q_{fluidic}} + \frac{1}{Q_{intrinsic}} + \frac{1}{Q_{clamping}} + \cdots \tag{26}$$

The dominant contribution at low temperature and under high-vacuum is from clamping losses (i.e. energy dissipation through the membrane supports). For a thin circular membrane the clamping losses are given by[112]:

$$\frac{1}{Q_{clamping}} = [6(1-\nu)]^{-\frac{3}{2}} \left[(\gamma_{0,n} R)\frac{h}{h_s}\right]^4 c_{0n} \tag{27}$$

where h_s is the thickness of the support and $c_{0n} \approx 1$ is a numerical factor related to the radiation admittance of the substrate and the normal force along the disk edge. The expected quality factor for the fundamental mode of a silicon membrane with $\nu = 0.28$ and ratio $\frac{h}{h_s} = \frac{110\ \text{nm}}{3\ \mu\text{m}} \approx 0.073$ is $Q_{clamping} \approx 3000$.

To validate the theoretical predictions and calculate realistic parameters, we performed finite element analysis using COMSOL Multiphysics Solid Mechanics module. The simulation geometry consisted of a 10 μm thick Si substrate of lateral dimensions 10 μm x 10 μm with 3 μm thick oxide layer and a 220 nm Si device layer on top. Circular hole of radius $R = \{0.5, 1, 1.5, 2\}$ μm is etched through the oxide to define the suspended silicon membrane (see Silicon Membrane Fabrication section). The outer boundaries are set as low-reflecting to minimize wave reflections. Figure 9 shows the fundamental vibrational mode of the silicon-on-insulator membrane structure.

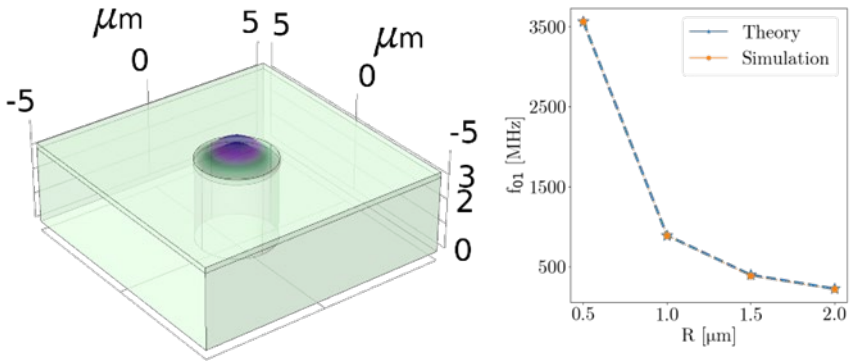

Figure 9 – COMSOL simulation of a circular Si membrane | The membrane is made of thin Si layer (220 nm) on top of a 3 μm layer of SiO_2 and a 10 μm Si substrate (not shown in the image). Eigenfrequency analysis result with good agreement to the theoretical prediction for the fundamental mode of membranes with $R = \{0.5, 1, 1.5, 2\}$ μm.

The simulated eigenfrequencies show good agreement with the analytical prediction of equation 25 with maximum deviation of 3%. In subsequent analysis of the coupling strength between mechanical resonators and superconducting flux qubits, we will use the values obtained for $R = 1$ μm: $f_{01} = 384$ MHz, and effective mass $m_{eff} = \frac{\rho}{\langle w \rangle} \iiint w dV = 3.62$ fg, which corresponds to zero-point fluctuation amplitude $u_{ZPF} = 2.5$ fm.

2.4 Gradiometer Superconducting Flux Qubit

Flux qubits are quantum two-level systems with macroscopic degrees of freedom, realized through superconducting loops interrupted by Josephson junctions[113,114]. The potential energy of the qubit exhibits two local minima that correspond to persistent currents circulating in opposite directions as illustrated in Figure 10a. When those states degenerate, the qubit states manifest as their symmetric and anti-symmetric superpositions. The persistent current, typically 100-500 nA in micron-sized loops, generate magnetic dipole moments on the order of 10^5 μ_B, which is five orders of magnitude larger than atomic magnetic moments[115].

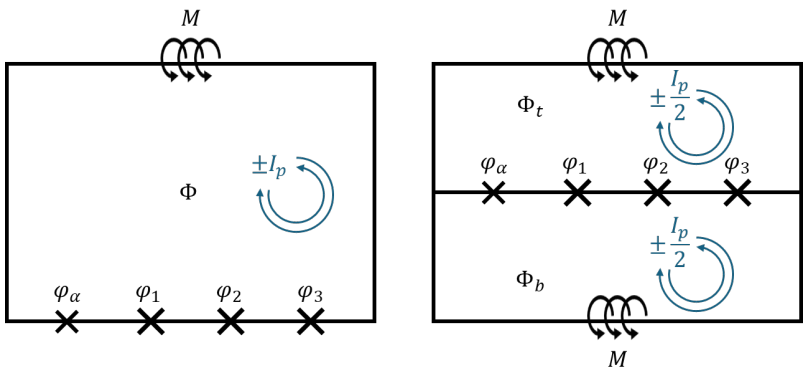

Figure 10 – Gradiometer flux qubit topology | Left panel: Standard flux qubit topology where four Josephson junctions intersect a superconducting loop. The persistent current I_p can flow in two opposite directions depending on the external magnetic flux Φ. The mutual inductance of the loop M is also depicted. Right panel: Gradiometer flux qubit with top (t) and bottom (b) loops. The persistent current is divided equally between the loops while the mutual inductance of each arm remains the same.

The large magnetic dipole moment fundamentally enhances the magnetic flux sensitivity of flux qubits compared to conventional superconducting quantum interference devices (SQUIDs). The qubit energy levels shift linearly with applied magnetic flux, on the order of 500 GHz/G, providing a direct transduction mechanism between magnetic field and measurable energy[116]. Under optimal conditions at millikelvin temperatures, flux qubits achieve flux sensitivities of 10^{-8} Φ_0/Hz, representing an improvement over DC SQUIDs[117].

To enhance sensitivity to local magnetic flux changes induced by mechanical nano-beams, through a mechanism that will be discussed later; while rejecting common-mode, we employ gradiometer architecture. The gradiometer flux qubit (GFQ) utilizes a figure-eight geometry with two loops of different areas, creating a differential magnetometer that responds to magnetic field gradients rather than uniform fields. This configuration, schematically drawn in Figure 10b, provides inherent rejection of spatially uniform magnetic field, including those from distant sources and electromagnetic interference, while maintaining high sensitivity to localized magnetic signatures such as those generated by the mechanical motion.

2.4.1 Model of Gradiometer Flux Qubit

The gradiometer flux qubit schematically drawn in Figure 10b, consists of a figure-eight superconducting loop configuration designed to provide differential magnetic field sensitivity. Unlike conventional single-loop flux qubits, the GFQ comprises two superconducting loops that share a common arm containing four Josephson junctions. Three junctions are identical with critical current I_c, while the fourth junction has a reduced critical current αI_c, where $\alpha < 1$ is the asymmetry parameter.

The gradiometer architecture exploits the principle of common-mode rejection. Uniform magnetic fields threading both loops generate equal and opposite flux contributions, resulting in zero net flux through the differential setup. Conversely, spatially varying magnetic fields create unequal flux threading each loop, producing a measurable differential signal. This

configuration is particularly sensitive to localized flux sources, such as those generated by the mechanical motion of a nano-beam.

Applying Faraday's law around each loop yields:

$$\varphi_\alpha + \varphi_1 + \varphi_2 + \varphi_3 = \quad 2\pi\frac{\Phi_t}{\Phi_0} \tag{28}$$

$$\varphi_\alpha + \varphi_1 + \varphi_2 + \varphi_3 = -2\pi\frac{\Phi_b}{\Phi_0}$$

where φ_i represents the superconducting phase difference across the i-th Josephson junction, Φ_t (Φ_b) is the magnetic flux through the top (bottom) loop, and $\Phi_0 = \frac{h}{2e} \approx 2.07 \times 10^{-15}$ Wb is the magnetic flux quantum. These constraints can be combined to eliminate the phase across the asymmetric junction:

$$\varphi_\alpha = \pi\frac{\Phi_d}{\Phi_0} - \varphi_1 - \varphi_2 - \varphi_3 \tag{29}$$

where the differential flux $\Phi_d = \Phi_t - \Phi_b$ becomes the fundamental control parameter for the qubit energy levels.

The potential energy of the gradiometer circuit arises from the Josephson coupling across each junction. For junctions with Josephson energies $E_J = \frac{\Phi_0 I_0}{2\pi}$, the total potential energy is:

$$U = -E_J\left[\sum_{i=1}^{3}\cos(\varphi_i) + \alpha\cos\left(\pi\frac{\Phi_d}{\Phi_0} - \varphi_1 - \varphi_2 - \varphi_3\right)\right] \tag{30}$$

At the optimal operating point $\frac{\Phi_d}{\Phi_0} = 1$, the potential energy exhibits two degenerate minima. At that point, the phases across the junctions satisfy $\varphi_{i=1,2,3} \equiv \varphi^*$ where $\sin(\varphi^*) = \alpha\sin(3\varphi^*)$.

The two degenerate solutions correspond to persistent current states with opposite circulation directions:

$$I_p = \pm I_0\sqrt{\frac{3}{4} - \frac{1}{4\alpha}} \tag{31}$$

The kinetic energy arises from the charging energy stored in the junction and geometric capacitances. The circuit, as shown in Figure 11, contains both junction capacitances C_J and parasitic capacitances C_{ij} between superconducting islands.

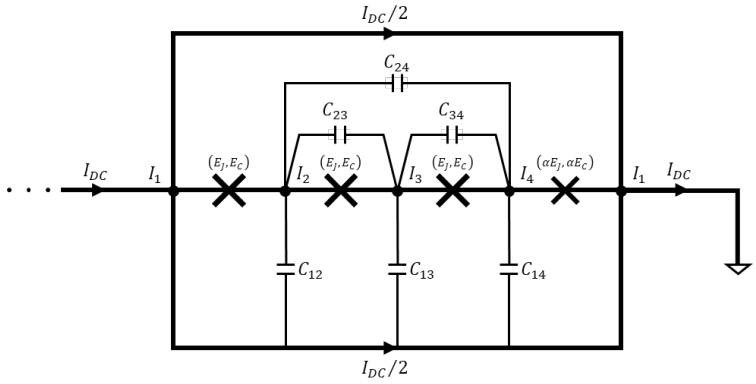

Figure 11 – Schematic circuit drawing of the gradiometer flux qubit | The Josephson junctions, depicted by × and characterized by the Josephson energy E_J and the capacitive energy E_C, create four superconducting islands I_i connected via the capacitors C_{ij}. Direct current bias I_{DC} is used to control the energy of the qubit.

The total kinetic energy of the circuit can be expressed as[118]:

$$K = \frac{1}{2}\sum_{i\neq j} C_{ij}\left(V_j - V_i\right)^2 + \frac{1}{2}C_J[(V_2 - V_1)^2 + (V_3 - V_2)^2 + (V_4 - V_3)^2 + \alpha(V_1 - V_4)^2] \tag{32}$$

where V_i represents the electrostatic potential of the i-th superconducting island. In matrix form, the kinetic energy becomes:

$$K = \frac{1}{2}\tilde{V}^T\tilde{C}_J\tilde{V} + \frac{1}{2}\tilde{V}^T\tilde{C}_G\tilde{V} \tag{33}$$

with $\tilde{V} = (V_1 \quad V_2 \quad V_3 \quad V_4)^T$. The junction capacitance matrix $\tilde{C}_J$ and geometric capacitance matrix $\tilde{C}_G$ are given by:

$$\tilde{C}_J = C_J\begin{pmatrix} 1+\alpha & -1 & 0 & -\alpha \\ -1 & 2 & -1 & 2 \\ 0 & -1 & 2 & -1 \\ -\alpha & 0 & -1 & 1+\alpha \end{pmatrix} \tag{34}$$

$$\tilde{C}_G = \begin{pmatrix} C_{12}+C_{13}+C_{14} & -C_{12} & -C_{13} & -C_{14} \\ -C_{12} & C_{12}+C_{23}+C_{24} & -C_{23} & -C_{24} \\ -C_{13} & -C_{23} & C_{13}+C_{23}+C_{34} & -C_{34} \\ -C_{14} & -C_{24} & -C_{34} & C_{14}+C_{24}+C_{34} \end{pmatrix}$$

The Hamiltonian of the gradiometer flux qubit can be derived with respect to different basis. We will work with the so-called charge basis that allows direct simulation of the capacitive

contribution. To do so we introduce a transformation from absolute voltages $\tilde{V}$ to junction voltages $\tilde{V}_j = P^{-1}\tilde{V}$. Here $\tilde{V}_j = (V_{12} \quad V_{23} \quad V_{34})^T$ where $V_{ij} = V_j - V_i$. In the case where the island I_1 is grounded ($V_1 \equiv 0$) the transformation matrix reduces to $P = \begin{pmatrix} 0\,0\,0 \\ 1\,0\,0 \\ 1\,1\,0 \\ 1\,1\,1 \end{pmatrix}$.

Let us define the conjugate charge variables using the Josephson relation $\frac{\Phi_0}{2\pi}\dot{\varphi}_j = V_{j,j+1}$:

$$n_j \equiv \frac{1}{\hbar}\frac{\partial \mathcal{L}}{\partial \dot{\varphi}_j} = \frac{\hbar}{(2e)^2} C_j \dot{\varphi}_j \tag{35}$$

Resulting with the complete Hamiltonian in the charge representation:

$$\mathcal{H} = \frac{(2e)^2}{2}\tilde{n}^T\left(P^T\tilde{C}P\right)^{-1}\tilde{n} + U \tag{36}$$

where $\tilde{n} = (n_1 \quad n_2 \quad n_3)^T$ represents the charge operators and $\tilde{C} = \tilde{C}_J + \tilde{C}_G$ is the total capacitance matrix. In the vicinity of the optimal operating point, the energy spectrum demonstrates a near-perfect qubit behavior. This is characterized by a clear separation between the two lowest energy states and the higher excited states (in some cases, the third energy level is located above the superconducting gap). This enables an effective two-level description with the pseudo-Hamiltonian:

$$\mathcal{H} = \frac{\hbar}{2}(\Delta\hat{\sigma}_z + \epsilon\hat{\sigma}_x) \tag{37}$$

The energy eigenvalues of the Hamiltonian are $E_\pm = \pm\frac{\hbar}{2}\sqrt{\Delta^2 + \epsilon^2}$ where Δ is the tunnelling energy between the two lowest energy states, and $\epsilon = \frac{I_p}{\hbar}(\Phi_d - \Phi_0)$ represents the energy bias controlled by the differential flux. By defining the flux parameter of the gradiometer qubit $\Phi = \frac{\Phi_d}{2}$, we obtain the expression for ϵ as of a standard flux qubit[118]:

$$\epsilon = \frac{2I_p}{\hbar}\left(\Phi - \frac{\Phi_0}{2}\right) \tag{38}$$

At the degeneracy point $\Phi = \frac{\Phi_0}{2}$, the flux dependent term ϵ vanish and the qubit is immune to first-order flux noise, providing optimal coherence properties.

The gradiometer responds to external magnetic fields through the differential flux Φ_d. For identical loops, global uniform magnetic field will result with $\Phi_d = 0$. Therefore, we introduce the current bias I_{DC} (see Figure 11) that will split evenly between the two loops creating

opposite magnetic flux through the top and bottom loops. Considering only the mutual inductance of the outer arms M, the flux threading each loop is:

$$\Phi_t = M\frac{I_{DC}}{2} = -\Phi_b \quad (39)$$
$$\downarrow$$
$$\Phi = M\frac{I_{DC}}{2}$$

Note that at the optimal operating point where $\Phi = \frac{\Phi_0}{2}$, the mutual inductance can be experimentally determined:

$$M = \frac{\Phi_0}{I_{DC}^{optimal}} \quad (40)$$

In the case of loops with different areas, an external magnetic field can be used to bias the qubit. The flux difference between the loops of the gradiometer is given by:

$$\Phi_d = MI_{DC} + \delta A B_{ext}\cos(\theta) \quad (41)$$

with δA the difference between the area of the top and bottom loops. B_{ext} and θ are the magnitude and angle of an external magnetic field, respectively.

2.5 Coplanar Waveguide Resonator With Bragg Filter Termination

A Bragg reflector consists of a periodic structure of alternating high and low impedance sections that creates a notch filter around specific frequencies. The Bragg reflector can be designed to provide high reflectivity at a desired frequency range while maintaining DC conductivity. The structure consists of alternating sections of narrow and wide coplanar waveguide geometries, creating impedance variations that produce the required reflection properties.

The key advantage of the Bragg reflector is that it provides the necessary boundary conditions for resonator operation while allowing DC current flow. The periodic structure acts as a high- or low impedance termination at the resonator frequency (depending on the choice of the impedance adjacent to the resonator), effectively confining the electromagnetic field within the resonator volume. Simultaneously, the continuous superconducting path allows unimpeded DC current flow for qubit biasing.

In this section we will follow the scattering-matrix formalism proposed in reference 118 and apply it to a coplanar waveguide (CPW) transmission line terminated on one end by a Bragg filter and on the other end shorted to the ground.

2.5.1 Transmission Line Model

To analyze the electromagnetic properties of coplanar waveguide resonators in our circuit QED architecture, we employ a distributed transmission line model. This approach is essential for understanding wave propagation and reflection phenomena at microwave frequencies, where the wavelength becomes comparable to the physical dimensions of the circuit elements.

The coplanar waveguide transmission line is modeled as a cascade of infinitesimal LC elements, as illustrated in Figure 12. Each unit cell of length u is characterized by inductance L_u and capacitance C_u. This discrete representation captures the fundamental electromagnetic properties while enabling mathematical analysis of wave propagation.

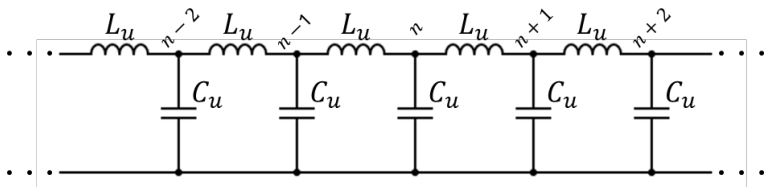

Figure 12 – Distributed-element model of transmission line | Each unit cells u of the transmission line in characterized by its inductance L_u and capacitance to the ground C_u.

In the continuum limit, where $u \to 0$, the inductance and capacitance are normalized to unit length, yielding the distributed parameters $\mathcal{L}$ and $\mathcal{C}$ representing inductance and capacitance per unit length, respectively. This continuum approximation is valid when the unit cell length is much smaller than the wavelength of interest.

The voltage $V(x,t)$ and current $I(x,t)$ along the transmission line are governed by Kirchhoff's laws applied to each infinitesimal element:

$$\frac{\partial V}{\partial x} = -\mathcal{L}\frac{\partial I}{\partial t} \tag{42}$$

$$\frac{\partial I}{\partial x} = -\mathcal{C}\frac{\partial V}{\partial t}$$

These coupled equations describe the fundamental relationship between voltage and current in distributed systems, where spatial and temporal derivatives are coupled through the line parameters.

To decouple these equations and analyze wave propagation, we introduce forward and backward propagation amplitudes. These quantities represent the decomposition of voltage and current into waves traveling in opposite directions along the transmission line:

$$A^{\rightarrow} = \frac{V}{\sqrt{Z_0}} + I\sqrt{Z_0} \tag{43}$$

$$A^{\leftarrow} = \frac{V}{\sqrt{Z_0}} - I\sqrt{Z_0}$$

where $Z_0 = \sqrt{\mathcal{L}/\mathcal{C}}$ is the characteristic impedance of the transmission line. This transformation separates the electromagnetic field into components propagating in the +x and -x directions. Substituting the propagation amplitudes into Kirchhoff's equations yields decoupled wave equations:

$$\frac{\partial A^{\rightarrow}}{\partial t} + c\frac{\partial A^{\rightarrow}}{\partial x} = 0 \tag{44}$$

$$\frac{\partial A^{\leftarrow}}{\partial t} - c\frac{\partial A^{\leftarrow}}{\partial x} = 0$$

where $c = 1/\sqrt{\mathcal{L}\mathcal{C}}$ is the electromagnetic wave velocity in the transmission line. These equations demonstrate that $A^{\rightarrow}$ represents a wave traveling in the +x direction with velocity c, while $A^{\leftarrow}$ represents a wave traveling in the -x direction with the same velocity. For harmonic excitation at frequency ω, the forward propagating wave solution takes the form:

$$A^{\rightarrow}(x,t) = \mathcal{A}(x)^{\rightarrow}e^{-i\omega t} + c.c. \tag{45}$$

The spatial dependence $\mathcal{A}(x)$ satisfies the reduced wave equation, yielding:

$$\mathcal{A}(\mathrm{x}) = \mathcal{A}^0 e^{ikx} \tag{46}$$

where $k = \omega/c$ is the propagation constant (wave number).

The phase accumulated by electromagnetic wave propagation from position x_1 to position x_2 along the transmission line is:

$$\phi = \omega\frac{x_2 - x_1}{c} = k(x_2 - x_1) \tag{47}$$

This phase relationship is fundamental for understanding interference phenomena in Bragg filters, where constructive and destructive interference between waves reflected from periodic impedance discontinuities creates the desired filtering characteristics. For a quarter-wavelength section (the basic building block of Bragg filters), the phase accumulation is $\phi = \frac{\pi}{2}$, corresponding to a 90° phase shift. Multiple quarter-wave sections with alternating impedances create the periodic structure necessary for Bragg reflection.

2.5.2 Scatter-Matrix Analysis

The behavior of electromagnetic waves at discontinuities in transmission line circuits can be systematically analyzed using scattering matrix methods. This approach is essential for understanding the reflection and transmission properties of impedance mismatches, lumped elements, and periodic structures that form the basis of Bragg filters.

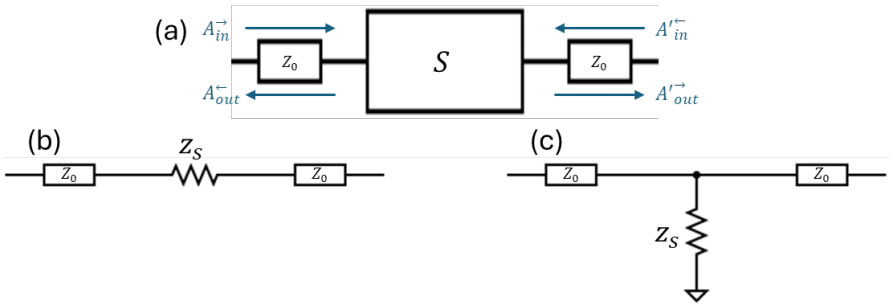

Figure 13 – Scattering elements | (a) general scattering element embedded in a transmission line. Scattering element of impedance Z_S connected in series (b) or in parallel (short to ground, c) to the transmission line.

Single Elements

The relationship between incoming and outgoing electromagnetic waves at a scattering element, depicted in Figure 13, is described by the scattering matrix formalism:

$$\begin{pmatrix} A^{\leftarrow}_{out} \\ A'^{\rightarrow}_{out} \end{pmatrix} = \overbrace{\begin{pmatrix} r_{\leftarrow} & t'_{\leftarrow} \\ t_{\rightarrow} & r'_{\rightarrow} \end{pmatrix}}^{S} \begin{pmatrix} A^{\rightarrow}_{in} \\ A'^{\leftarrow}_{in} \end{pmatrix} \tag{48}$$

where $r_{\leftarrow}$ ($r'_{\rightarrow}$) and $t_{\rightarrow}$ ($t'_{\leftarrow}$) represent the reflection and transmission coefficients respectively. For symmetric scatterers, these coefficients satisfy $r_{\leftarrow} = r'_{\rightarrow} \equiv r$ and $t_{\rightarrow} = t'_{\leftarrow} \equiv t$, simplifying the analysis. Throughout this analysis, we assume single-sided excitation ($A'^{\leftarrow}_{in} = 0$).

The simplest element is a uniform transmission line segment of length l which introduces no reflection but accumulates phase according to the propagation constant. The scattering parameters are:

$$r = 0 \qquad (49)$$

$$t = e^{ikl}$$

where the phase factor e^{ikl} represents the time delay for wave propagation across the segment.

For an impedance Z_S connected in parallel to the transmission lines, as exemplified in Figure 13c the Kirchhoff's equations become:

Voltage constraint: $$V_s = V = V^{'} \qquad (50)$$

Current continuity: $$\frac{V_s}{Z_s} = I_s = I - I^{'}$$

This configuration yields the scattering coefficients:

$$r = -\frac{1}{2z+1} \qquad (51)$$

$$t = \frac{2z}{2z+1}$$

where $z = Z_S/Z_0$ is the normalized impedance.

For an abrupt transition between transmission lines with impedances Z_1 and Z_2, continuity of voltage and current at the interface requires:

Voltage constraint: $$V = V^{'} \rightarrow \sqrt{Z_1}(A_{in}^{\rightarrow} + A_{out}^{\leftarrow}) = \sqrt{Z_2}\left(A^{'\leftarrow}_{in} + A^{'\rightarrow}_{out}\right) \qquad (52)$$

Current continuity: $$I = I^{'} \rightarrow \frac{1}{\sqrt{Z_1}}(A_{in}^{\rightarrow} - A_{out}^{\leftarrow}) = \frac{1}{\sqrt{Z_2}}\left(A^{'\rightarrow}_{out} - A^{'\leftarrow}_{in}\right)$$

The resulting scattering coefficients are:

$$r = \frac{Z_2 - Z_1}{Z_1 + Z_2} \quad ; \quad t = \frac{2\sqrt{Z_1 Z_2}}{Z_1 + Z_2} \tag{53}$$

$$r' = \frac{Z_1 - Z_2}{Z_1 + Z_2} \quad ; \quad t' = \frac{2\sqrt{Z_1 Z_2}}{Z_1 + Z_2}$$

These expressions form the foundation for analyzing impedance mismatches in Bragg filters.

Transmission Line Resonator Terminated by Asymmetrical Terminations

The most general case involves a transmission line of length L terminated by different scatterers S and S′ at each end as depicted in Figure 14. This configuration provides the framework for analyzing complex resonator systems where the terminations have distinct reflection and transmission properties, such as a Bragg filter on one end and a short circuit on the other.

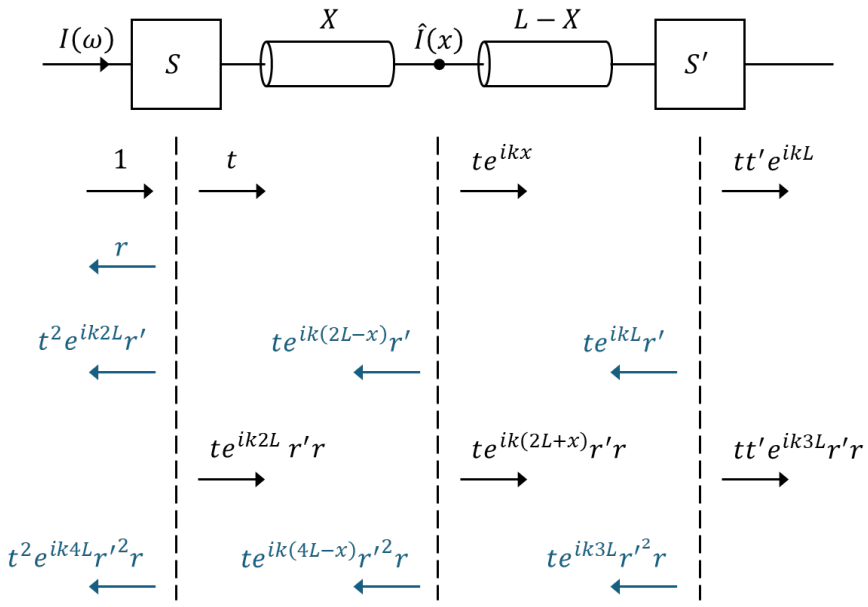

Figure 14 – Asymmetrical transmission line | Transmission line of length L, terminated by different scatterers S and S′. The current at each point of the transmission line $\hat{I}(x)$ results from an infinite number of reflections.

For an electromagnetic wave incident from the side of scatterer S, multiple reflections occur between the two terminations, creating an infinite series of forward and backward propagating waves. The total reflection (r^*) and transmission (t^*) coefficients for this asymmetrically terminated system are:

$$r^*(\omega) = r(\omega) + t(\omega)^2 e^{ik2L} r'(\omega) \sum_{n=0}^{\infty} \left(e^{ik2L} r'(\omega) r(\omega) \right)^n = r(\omega) + \frac{t(\omega)^2 r'(\omega) e^{ik2L}}{1 - r'(\omega) r(\omega) e^{ik2L}} \quad (54)$$

$$t^*(\omega) = t(\omega) t'(\omega) e^{ikL} \sum_{n=0}^{\infty} \left[r'(\omega) r(\omega) e^{ik2L} \right]^n = \frac{t(\omega) t'(\omega) e^{ikL}}{1 - r'(\omega) r(\omega) e^{ik2L}}$$

Where $r(\omega)$, $t(\omega)$ and $r'(\omega)$, $t'(\omega)$ are the scattering coefficients of the individual terminations S and S′ respectively. The complex wave number $k = \frac{1}{c}(\omega + i\kappa)$ includes both the propagation constant and any losses κ in the transmission line.

The current at any position x along the transmission line can be expressed in terms of the incident propagation amplitude $A_{in}^{\rightarrow}$:

$$I(x, \omega) = \frac{1}{\sqrt{Z_0}} f_{\rightarrow}(x, \omega) A_{in}^{\rightarrow} \quad (55)$$

where $f_{\rightarrow}(x, \omega)$ represents the difference between forward and backward propagating current waves. The spatial distribution function account for all multiple reflections between the terminations:

$$f_{\rightarrow}(x, \omega) = t \frac{e^{ikx} - r' e^{ik(2L - x)}}{1 - r' r e^{ik2L}} \quad (56)$$

These expression reveal the standing wave pattern that develops within the asymmetrically terminated transmission line, with the specific distribution depending on the frequency-dependent reflection properties of both terminations.

The asymmetrically terminated transmission line supports resonant modes when specific phase and amplitude conditions are satisfied. For constructive interference and efficient energy storage, the round-trip phase accumulated by electromagnetic waves must satisfy:

$$\arg[r'(\omega) r(\omega)] + 2kL = 2\pi n \quad (57)$$

where n is an integer and $k = \omega/c$ is the real part of the wave number. This phase condition ensures that waves returning after a complete round trip between the terminations interfere constructively with the original wave. For high-quality resonances, an additional amplitude condition must be approximately satisfied:

$$\left| r'(\omega) r(\omega) \right| \approx 1 \quad (58)$$

This condition requires that the product of reflection magnitudes from both terminations approaches unity, minimizing energy loss during each round trip and enabling sustained oscillation within the cavity.

The combination of these conditions determines the resonance frequencies and quality factors of the system. When both terminations have high reflectivity ($|r'(\omega)|, |r(\omega)| \approx 1$), the amplitude condition is readily satisfied, and the resonance frequency is primarily determined by the phase matching requirement. The quality factor depends on how closely the amplitude condition is met, with deviations from unity leading to energy decay and finite Q values.

Chain of Elements

The analysis of multiple scattering elements requires accounting for multiple reflections between adjacent discontinuities. Consider two scatterers separated by a transmission line segment of length L similar to Figure 15.

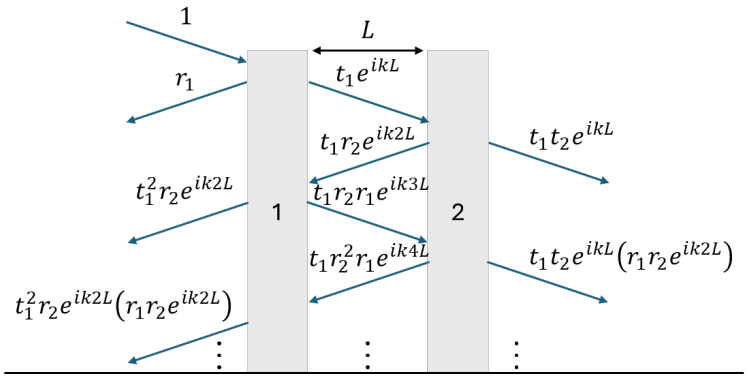

Figure 15 – A chain of two scatterers

When an electromagnetic wave encounters the first scatterer, part is reflected while part is transmitted. The transmitted wave propagates distance L, accumulating phase e^{ikL}, before encountering the second scatterer. Multiple reflections occur between the scatterers, creating an infinite series that must be summed up. The total reflection and transmission coefficients for the cascaded system are:

$$r = r_1 + \frac{t_1^2 r_2 e^{ik2L}}{1 - r_1 r_2 e^{ik2L}} \quad ; \quad r' = r_2 + \frac{t_2^2 r_1 e^{ik2L}}{1 - r_2 r_1 e^{ik2L}} \tag{59}$$

$$t = \frac{t_1 t_2 e^{ikL}}{1 - r_1 r_2 e^{ik2L}} \quad ; \quad t' = \frac{t_1 t_2 e^{ikL}}{1 - r_1 r_2 e^{ik2L}}$$

where r_1, t_1 and r_2, t_2 are the individual scattering coefficients of the first and second elements respectively.

Bragg Filters

These scattering matrix results provide the building blocks for analyzing Bragg filters as cascaded networks of impedance mismatches and transmission line segments. Microwave Bragg filters are constructed from periodic structures of transmission lines with alternating characteristic impedances Z_1 and Z_2, where each segment has length $L_b = \frac{\lambda_B}{4}$, with λ_B the center wavelength to be filtered.

The fundamental design parameters of a Bragg filter include the impedance values Z_1 and Z_2 which determine the reflection per interface, the number of doublets m which sets the total reflection magnitude and bandwidth, the segment length L_b that ensures constructive interference at the design frequency, and the resulting internal interfaces $n = 2m - 1$ that create the periodic structure through impedance mismatches.

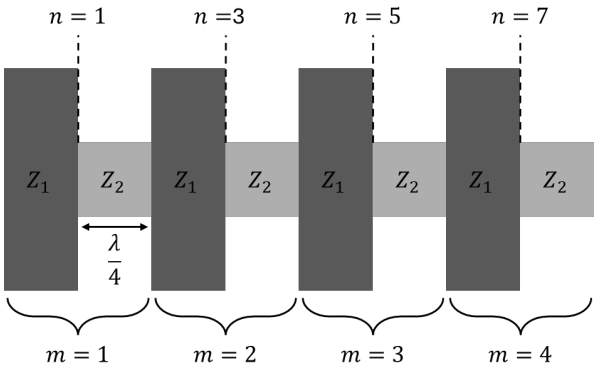

Figure 16 – Bragg filter | $m = 4$ doublets and $n = 7$ internal interfaces between low impedance (Z_1) and high impedance (Z_2) segments.

For a Bragg filter with $m = 4$ doublets, there are $n = 7$ internal impedance mismatches as shown in Figure 16. The periodic structure alternates between low and high impedance sections, creating a photonic bandgap around the design frequency that provides the desired filtering characteristics while maintaining DC conductivity throughout the structure.

Using the cascaded scattering formulas derived earlier, the total reflection and transmission of the Bragg filter can be calculated systematically. The elements are chained in sequence through phase accumulation during propagation in Z_1 quarter-wave segments, impedance mismatches at Z_1/Z_2 interfaces, phase accumulation during propagation in Z_2 quarter-wave

segments, impedance mismatches at Z_2/Z_1 interfaces, with this pattern repeated for m doublets. Each impedance mismatch contributes reflection according to $r_{interface} = \frac{Z_2 - Z_1}{Z_1 + Z_2}$, while each quarter-wave segment contributes phase delay $t_{segment} = e^{i\frac{\pi}{2}}$. The recursive application of the cascading formulas builds up the total response through constructive and destructive interference between multiple internal reflections. For example, Figure 17 shows the reflection and transmission coefficients of the Bragg filter for a center frequency ω_c, $Z_1 = 35\ \Omega$, $Z_2 = 80\ \Omega$, and $m = 4$. The effective impedance on the filter is $Z_{eff} = \left(\frac{Z_2}{Z_1}\right)^{2m} Z_0 \approx 37$ kΩ, with $Z_0 = 50\ \Omega$ the input line impedance[119].

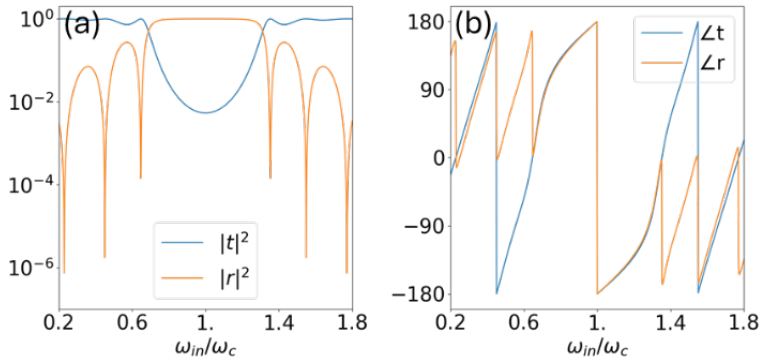

Figure 17 – Bragg filter response | Transmission and reflection power (a) and phase response (b) of a Bragg filter with $m = 4$, $Z_1 = 35\ \Omega$ and $Z_2 = 80\ \Omega$. The x-axis represents the incoming frequency ω_{in} normalized by the center filtered frequency ω_c.

The calculated reflection and transmission coefficients exhibit the characteristic Bragg filter response. The reflection shows high values ($|r|^2 \approx 0.99$) in the stopband around $\frac{\omega_{in}}{\omega_c} = 1$ with sharp transitions at band edges, multiple reflection nulls at frequencies where destructive interference occurs, and bandwidth determined by the impedance contrast ratio $Z_2/Z_1 \approx 2.3$. This frequency selectivity enables electromagnetic isolation at the resonator frequency while preserving DC conductivity.

The phase response of the Bragg filter shows characteristic behavior crucial for resonator applications. The reflection phase exhibits rapid phase variation through the stopband with phase jumps of ±180° at reflection nulls and smooth phase transition in passbands. The transmission phase demonstrates linear phase accumulation outside the stopband, enhanced group delay within the Bragg frequency range, and phase penetration depth effects that contribute to quality factor enhancement.

The phase penetration depth effects arise from the finite spatial extent over which electromagnetic waves penetrate the Bragg structure before being reflected. Unlike an ideal mirror that reflects instantaneously at the interface, the Bragg filter allows waves to propagate several periods into the periodic structure as evanescent modes before complete reflection occurs. This penetration creates an effective additional optical path length that manifests in the transmission phase as an enhanced phase accumulation compared to simple impedance mismatches. In the transmission phase response, these effects appear as a frequency-dependent phase delay that exceeds the geometrical phase accumulation expected from the physical length of the filter. Near the Bragg frequency, the group velocity of electromagnetic waves decreases significantly as they interact with the periodic structure, leading to increased phase accumulation per unit frequency change. This enhanced phase response corresponds to increased photon storage time within the resonator system. The frequency-dependent phase response creates modified boundary conditions that are more favorable for energy storage, as photons experience extended interaction times with the resonator boundaries during the penetration and reflection process. The magnitude of this enhancement depends on the impedance contrast ratio, number of periods, and the specific frequency of operation, with stronger impedance contrasts and more periods generally yielding greater enhancement factors.

Bragg-Terminated Resonator with Short Circuit

A specific implementation of practical importance for the gradiometer flux qubit system consists of a transmission line of length $L = \frac{3}{4}\lambda$ terminated by a Bragg filter on one end and a short circuit to ground on the other end as presented in Figure 18. This configuration combines the electromagnetic isolation properties of the Bragg filter with the perfect reflection characteristics of the short circuit, creating an efficient resonator structure while maintaining DC conductivity.

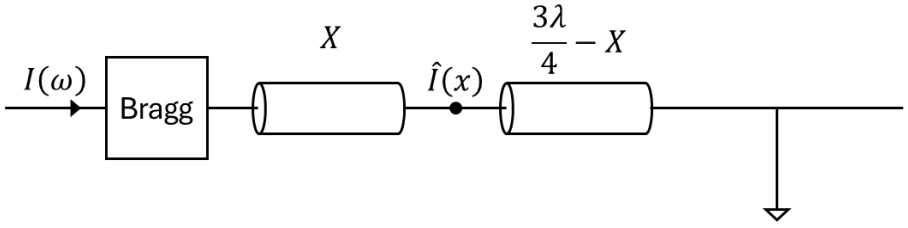

Figure 18 – Transmission line of length $\frac{3}{4}\lambda$ terminated by a Bragg filter and a short circuit.

For the short circuit termination, the scattering coefficients are obtained by setting the normalized impedance $z = 0$ in Equation 51, yielding $r_{short} = -1$ and $t_{short} = 0$. The short circuit provides perfect reflection with a π phase shift while completely blocking transmission. Applying the asymmetrical termination formulas of Equation 54 with these boundary conditions, the total reflection and transmission coefficients become:

$$r^*(\omega) = r_{Bragg}(\omega) - \frac{t_{Bragg}(\omega)^2 e^{i3\pi\frac{\omega}{\omega_r} - 2L\frac{\kappa}{c}}}{1 + r_{Bragg}(\omega) e^{i3\pi\frac{\omega}{\omega_r} - 2L\frac{\kappa}{c}}} \tag{60}$$

$$t^*(\omega) = 0$$

The zero transmission-coefficient confirms that no electromagnetic energy passes through the short-circuited end, making this an ideal resonator configuration. The reflection coefficient exhibits frequency-dependent behavior determined by the interplay between the Bragg filter characteristics and the $\frac{3}{4}\lambda$ electrical length.

The current distribution (Equation 56) along the transmission line is given by:

$$f_{\rightarrow}(x, \omega) = t_{Bragg}(\omega) \frac{e^{ikx} + e^{ik(2L-x)}}{1 + r_{Bragg}(\omega) e^{ik2L}} \tag{61}$$

this expression reveals the standing wave pattern within the resonator, with current nodes occurring at the short circuit termination and at specific positions determined by the frequency and Bragg filter properties. The current distribution results with optimized galvanic coupling to the qubit at appropriate locations, where the current is maximal along the transmission line.

The resonance condition for this system requires that the total phase accumulated during a round-trip equals 4π. This condition corresponds to $n = 2$ in Equation 38, and is a result of the length of the transmission line defined as $L = \frac{3}{4}\lambda$. The total phase consists of contributions from the Bragg filter reflection $\varphi_{Bragg} = \varphi^*(\omega)$, the transmission line propagation $\varphi_{TL} = \omega\frac{2L}{c}$, and the short circuit reflection $\varphi_{short} = \pi$. The resulting resonance frequency is:

$$\omega_r = \frac{c}{2L}[3\pi - \varphi^*(\omega_r)] \tag{62}$$

This expression shows that the resonance frequency is determined not only by the geometric length but also by the frequency-dependent phase response of the Bragg filter, providing additional tunability compared to conventional capacitively terminated resonators.

The energy decay rate of the resonator κ_C is determined by the ratio between the round-trip time $\tau = \partial_\omega \varphi_{acc}$ and the energy loss per round trip. Unlike capacitor-terminated resonators where the accumulated phase is linear in frequency, the Bragg termination introduces frequency-dependent phase behavior. Near the resonance frequency, this phase response becomes effectively linear, allowing the round-trip time to be expressed as:

$$\tau = \gamma \frac{3\pi}{\omega_r} \tag{63}$$

The enhancement factor $\gamma > 1$ accounts for the finite penetration depth of electromagnetic waves into the Bragg structure before reflection occurs. This penetration creates additional phase delay compared to ideal reflection, effectively increasing the photon storage time and improving the quality factor.

As energy loss occurs only at the Bragg filter (the short circuit provides perfect reflection), the decay rate and quality-factor are:

$$\kappa_C = \frac{\left|t_{Bragg}\right|^2}{\tau} \tag{64}$$

$$Q_C \equiv \frac{\omega_r}{\kappa_C} = \frac{3\pi\gamma}{\left|t_{Bragg}\right|^2}$$

This configuration achieves quality-factor enhancement through both the high reflectivity of the Bragg filter and the phase penetration effects that increase the effective photon storage time by the factor γ. The resulting performance represents a significant improvement over simple impedance-mismatched terminations while maintaining the DC conductivity essential for gradiometer flux qubit operation.

2.6 Coupling Flux Qubit To Bragg Resonator

2.6.1 Circuit QED Hamiltonian and Coupling Derivation

The system Hamiltonian for the coupled qubit-resonator system is given by:

$$\mathcal{H}/\hbar = \omega_r \hat{a}^\dagger \hat{a} + \frac{\Delta}{2}\hat{\sigma}_z + \frac{\epsilon}{2}\hat{\sigma}_x + g\hat{\sigma}_x(\hat{a}^\dagger + \hat{a}) \tag{65}$$

where ω_r is the resonator frequency, $\hat{a}^\dagger$ and $\hat{a}$ are the photon creation and annihilation operators. Here we consider only a specific mode of the resonator, and the mode index is omitted. Δ is the qubit minimal frequency (gap), and g is the coupling strength. The Pauli matrices $\hat{\sigma}_x$ and $\hat{\sigma}_z$ represent the qubit operators in the computational basis.

At the optimal operating point of the flux qubit where $\epsilon = 0$, the coupling term g arises from flux fluctuations in the qubit loop. Following Equation 38, the energy bias fluctuation is:

$$\delta\epsilon = \frac{2I_p}{\hbar}\delta\Phi = \frac{I_p}{\hbar}M\delta I(\hat{a}^\dagger + \hat{a}) \tag{66}$$

where I_p is the persistent current, M is the mutual inductance between the resonator and qubit loop, and δI represents the current fluctuation amplitude in the resonator. The resulting coupling is:

$$\frac{\delta\mathcal{H}}{\hbar} = \frac{\delta\epsilon}{2}\hat{\sigma}_x = M\frac{I_p}{2\hbar}\delta I\hat{\sigma}_x(\vec{a}^\dagger + \vec{a}) \equiv g\sigma_x(\hat{a}^\dagger + \hat{a}) \tag{67}$$

This yields the inductive coupling strength:

$$g = M\frac{I_p}{2\hbar}\delta I \tag{68}$$

To estimate the coupling strength the current fluctuation δI is calculated[118] using $\delta I(x) = \sqrt{\int \frac{\hbar\omega}{4\pi Z_0}|f_{\rightarrow}(x,\omega)|^2}$ and the mutual inductance is given by Equation 40.

2.7 Flux Qubit Relaxation and Dephasing

The coherence properties of gradiometer flux qubits are fundamentally limited by their interaction with environmental degrees of freedom. Understanding these decoherence mechanisms is essential for characterizing and optimizing their performance.

2.7.1 Purcell Decay

Relaxation refers to the process by which a qubit in the excited state spontaneously decays to its ground state by releasing energy to the environment. This energy exchange results from coupling between the qubit and environmental degrees of freedom, such as electromagnetic

fields, phonons, or other microscopic excitations. For a qubit initially in the excited state, the probability of remaining in that state decays exponentially:

$$P(t) = e^{-t/T_1} \tag{69}$$

where $P(t)$ is the probability that the qubit remains in the excited state at time t, and T_1 is the relaxation time. In circuit QED systems, Purcell decay arises from the coupling between the qubit and electromagnetic modes of the resonator. The interaction Hamiltonian is:

$$\mathcal{H}_{int}/\hbar = M\frac{I_p}{2\hbar}\delta I(\hat{\sigma}_+ A + \hat{\sigma}_- A^\dagger) \tag{70}$$

where M is the mutual inductance, I_p is the persistent current, and δI represents current fluctuations in the resonator. According to Fermi's Golden Rule[120], the Purcell decay rate is:

$$\Gamma_P = 2\pi\left(\frac{MI_p}{\hbar}\right)^2\left[S_I(\omega_{ge}) + S_I(-\omega_{ge})\right] \tag{71}$$

where $S_I \equiv \frac{1}{2\pi}\int_t \langle I(t)I(0)\rangle e^{i\omega t}$ is the current power spectrum. For the transmission line resonator, the current power spectrum is:

$$S_I = \frac{|f_{\rightarrow}(x,\omega)|^2}{Z_0} S_{A_{in}^{\rightarrow}} \tag{72}$$

where $f_{\rightarrow}(x,\omega)$ is the current distribution function and $S_{A_{in}^{\rightarrow}}$ is the photon influx power spectrum. By writing the explicit form $A_{in}^{\rightarrow} = \sum_n \sqrt{\frac{c}{2L}\hbar\omega_n}\hat{a}_n e_n^{-i\omega t} + H.c$ and moving to the continuum limit $\sum_n \frac{c}{2L}\hbar\omega_n \rightarrow \int_{d\omega}\frac{\hbar\omega}{4\pi}$, the photon influx power spectrum can be calculated from:

$$S_{A_{in}^{\rightarrow}} = \frac{\hbar\omega}{4\pi}\begin{cases}\langle \hat{a}_n \hat{a}_n^\dagger\rangle & \omega > 0 \\ \langle \hat{a}_n^\dagger \hat{a}_n\rangle & \omega < 0\end{cases} \tag{73}$$

For a finite temperature environment T, the total Purcell rate becomes:

$$\Gamma_P = \frac{\hbar\omega}{2Z_0}\left(\frac{MI_p}{\hbar}\right)^2 |f_{\rightarrow}(x,\omega)|^2 \coth\left(\frac{\hbar\omega}{2k_B T}\right) \tag{74}$$

This expression shows that the Purcell decay rate depends on the coupling strength, the current distribution in the resonator, and the thermal occupation of electromagnetic modes.

2.7.2 Qubit Dephasing Mechanisms

Dephasing, characterized by the time constant T_2, represents the loss of phase coherence between components of a quantum superposition without energy exchange with the environment. This process occurs when fluctuations in the qubit frequency due to environmental noise lead to the accumulation of random relative phases between basis states.

The overall dephasing rate $\Gamma_2 \equiv 1/T_2$ combines the effects of both pure dephasing Γ_ϕ and relaxation Γ_1:

$$\Gamma_2 = \frac{1}{2}\Gamma_1 + \Gamma_\phi \tag{75}$$

The dephasing decay is not strictly exponential and depends on the power spectrum of the noise source.

Free Induction Decay (Ramsey)

Consider a qubit undergoing free evolution for a time t. The total accumulated phase is $\varphi(t) = \omega_{ge}t + \delta(t)$, where ω_{ge} is the nominal qubit transition frequency. The second term, $\delta(t)$, is a stochastic phase error caused by fluctuations $\delta\lambda(t)$ in the Hamiltonian, which induce a frequency noise $\delta\omega(t)$. The phase error is the integral of this frequency noise: $\delta(t) = \int_0^t \delta\omega(t')dt'$.

If we assume the underlying frequency fluctuations $\delta\omega(t)$ constitute a Gaussian process then the accumulated phase $\delta(t)$ is a Gaussian random variable. The statistical uncertainty in this phase causes dephasing across an ensemble of measurements. This loss of coherence manifests as the free induction decay (FID), also known as Ramsey decay:

$$f_R(t) = \left\langle e^{i\delta(t)} \right\rangle = e^{-\frac{1}{2}\langle\varphi^2(t)\rangle} = \exp\left[-\frac{t^2}{2}\left(\frac{\partial\omega_{ge}}{\partial\lambda}\right)^2 \int_{-\infty}^{\infty} d\omega S_\lambda(\omega)\,\mathrm{sinc}^2\left(\frac{\omega t}{2}\right)\right] \tag{76}$$

where $S_\lambda(\omega)$ is the power spectrum of the noise source $\lambda(t)$. In the case of white noise where the power spectrum equals some constant $S_\lambda(\omega) = c$, the decay is exponential $f_R(t) = \exp\left[-t\left(\frac{\partial\omega_{ge}}{\partial\lambda}\right)^2 \pi c\right]$.

Hahn Echo Decay

A Hahn-Echo sequence is a powerful method for mitigating the effects of low frequency noise. The sequence begins with the qubit evolving freely for a time $\tau/2$. During this interval, it

accumulates a phase error δ_1. A π-pulse is then applied, which inverts the qubit state. This pulse has the crucial effect of reversing the sign of the phase accumulated during the subsequent free evolution period. The qubit then evolves for a second identical interval of $\tau/2$, accumulating a second phase error δ_2. Due to the pulse, the total deterministic phase cancels out, and the net stochastic phase, $\varphi_{total} = \delta_1 - \delta_2$, is the difference between the noise accumulated in the two intervals. Assuming the underlying frequency fluctuations $\delta\omega(t)$ constitute a Gaussian process, the net phase error φ_{total} is also a Gaussian random variable with zero mean. The decay of the echo signal, $f_E(t)$, is determined by the ensemble average of the final phase factor:

$$f_E(t) = \left\langle e^{i\varphi_{total}} \right\rangle = e^{-\frac{1}{2}\langle\varphi_{total}^2\rangle} \tag{77}$$

The variance $\left\langle\varphi_{total}^2\right\rangle$ can be calculated by filtering the noise power spectral density $S_\lambda(\omega)$ through a function determined by the echo sequence. This gives the final expression for the decay:

$$f_E(t) = \exp\left[-\frac{t^2}{2}\left(\frac{\partial\omega_{ge}}{\partial\lambda}\right)^2 \int_{-\infty}^{\infty} d\omega S_\lambda(\omega) \sin^2\left(\frac{\omega t}{4}\right) \mathrm{sinc}^2\left(\frac{\omega t}{4}\right)\right] \tag{78}$$

This result shows how the Hahn-Echo sequence effectively cancels the influence of low-frequency noise where $\omega \to 0$. If the noise is white, we get again an exponential decay function $f_E(t) = \exp\left[-\mathrm{t}\left(\frac{\partial\omega_{ge}}{\partial\lambda}\right)^2 \pi c\right]$.

Magnetic Flux Noise Dephasing

Superconducting flux qubits are sensitive to low-frequency magnetic flux noise. This noise is often characterized as "pink noise" or 1/f noise, meaning its power spectral density, $S_\lambda(\omega) = A_\lambda^2/\omega$, is inversely proportional to frequency.

This noise couples to a qubit's transition frequency, ω_{ge}, causing it to fluctuate and leading to dephasing. The impact of this noise depends critically on the experimental sequence used to measure coherence. In a Ramsey experiment, a qubit's free evolution exposes it to the entire noise spectrum. Due to its divergence at zero frequency, the effect of 1/f noise must be integrated. The low-frequency cutoff is set by measurement time *t*, while the high-frequency

cutoff, ω_{IR}, is arbitrary. The integrated effect of this noise is represented by the formula $\sqrt{\ln\left(\frac{1}{\omega_{IR}t}\right)}$ which leads to a Gaussian decay:

$$f_R(t) = \exp\left[-t^2\left(\frac{\partial\omega_{ge}}{\partial\lambda}\right)^2 A_\lambda^2 \ln\left(\frac{1}{\omega_{IR}t}\right)\right] \tag{79}$$

For typical cutoff frequency $\omega_{IR} = 1$ MHz and measurement time t = 1 second per point, $\sqrt{\ln\left(\frac{1}{\omega_{IR}t}\right)}$ equals approximately 3.7.

A Hahn-Echo sequence applies a π-pulse that refocuses the qubit's phase. This pulse sequence acts as a high-pass filter, effectively canceling the slow phase drifts caused by low-frequency noise. For 1/f noise, this completely removes the dependence on the arbitrary cutoff ω_{IR}, resulting in a cleaner decay form:

$$f_E(t) = \exp\left[-t^2\left(\frac{\partial\omega_{ge}}{\partial\lambda}\right)^2 A_\lambda^2 \ln(2)\right] \tag{80}$$

For the case of flux qubit, described by the Hamiltonian in Equation 37, the frequency $\omega_{ge} = \sqrt{\Delta^2 + \epsilon^2}$ depends on the energy bias ϵ, which is controlled by the external magnetic flux. It is through ϵ that the 1/f flux noise affects the qubit.

The qubit's first-order sensitivity to this noise is given by the derivative $\partial_\epsilon\omega_{ge} = \epsilon/\omega_{ge}$ ($\partial_\Phi\omega_{ge} = \left(\frac{2I_p}{\hbar}\right)^2 \frac{\Phi-\Phi_0/2}{\omega}$). The corresponding decay rates, defined by $f(t) = e^{-(t\Gamma)^2}$, are:

$$\Gamma_{2,R}^{\epsilon} = \frac{\epsilon}{\omega_{ge}} A_{\varphi,R}^{\epsilon} \sqrt{\ln\left(\frac{1}{\omega_{IR}t}\right)} \quad ; \quad \Gamma_{2,R}^{\Phi} = \left(\frac{2I_p}{\hbar}\right)^2 \frac{\Phi - \Phi_0/2}{\omega_{ge}} A_{\varphi,R}^{\Phi} \sqrt{\ln\left(\frac{1}{\omega_{IR}t}\right)} \tag{81}$$

$$\Gamma_{2,E}^{\epsilon} = \frac{\epsilon}{\omega_{ge}} A_{\varphi,E}^{\epsilon} \sqrt{\ln(2)} \quad ; \quad \Gamma_{2,E}^{\Phi} = \left(\frac{2I_p}{\hbar}\right)^2 \frac{\Phi - \Phi_0/2}{\omega_{ge}} A_{\varphi,E}^{\Phi} \sqrt{\ln(2)}$$

with A^{ϵ} (A^{Φ}) the power spectrum amplitude of the noise affecting ϵ (Φ). By tuning of the external flux so that $\epsilon = 0$, the sensitivity vanishes. This special operating point is known as the flux sweet spot. At this point, the qubit becomes, to first order, immune to flux noise, and the dephasing rates become zero.

However, coherence is still limited. Even at the sweet spot, the qubit's energy has a non-zero curvature, given by the second derivative $\frac{\partial^2 \omega_{ge}}{\partial \epsilon^2} = \Delta^2/\omega_{ge}(\epsilon)^3$. This means the qubit frequency still has a residual sensitivity to noise, also when ϵ vanish. In a previous work[118] an empirical law for the second order flux noise was established, which, with respect to ϵ and Φ, are given by:

$$\Gamma_{2,E}^{\epsilon,(2)} = \frac{14.4}{2\pi}\frac{\Delta^2}{\omega_{ge}(\epsilon)^3}\left(A_{\varphi,E}^{\epsilon}\right)^2 \quad ; \quad \Gamma_{2,E}^{\Phi,(2)} = \frac{14.4}{2\pi}\frac{\Delta^2}{\omega_{ge}(\Phi)^3}\left(\frac{2I_p}{\hbar}\right)^2\left(A_{\varphi,E}^{\Phi}\right)^2 \tag{82}$$

Photon Noise

A common source of dephasing in circuit QED systems arises from the qubit's interaction with photons in its coupled readout resonator. Even at millikelvin base temperatures, thermal photons from warmer stages can contribute to this dephasing, disrupting the qubit's quantum state. The thermal photon occupation follows Bose-Einstein statistics:

$$\bar{n}_{th} = \frac{1}{e^{\frac{\hbar\omega}{k_B T}} - 1} \tag{83}$$

For a multi-stage dilution refrigerator, the total thermal population is:

$$\bar{n}_{th}^{tot}(\omega) = \sum_T \alpha_T \bar{n}_{th}(T,\omega) \tag{84}$$

where α_T represents the attenuation factor from stage at temperature T. Thermal photons arrive from both the input port used for control signals and the output measurement port, where the amplifier chain operates at an effective temperature of approximately 10 K despite cryogenic pre-amplification. Typical values range from $\bar{n}_{th}^{tot} \approx 10^{-3}$ for well-filtered systems to $\bar{n}_{th}^{tot} \approx 10^{-2}$ for poorly isolated configurations.

The dispersive interaction between the qubit and the photon in its coupled readout resonator is described by the interaction Hamiltonian $\mathcal{H}_{int} = \hbar\chi\hat{\sigma}_z\left(\bar{n} + \frac{1}{2}\right)$. Here, $\bar{n} = \langle \hat{a}^\dagger \hat{a} \rangle$ is the average number of photons in the resonator and $\chi = g^2/\Delta$ is the dispersive coupling strength. This Hamiltonian means that the qubit's transition frequency, ω_{ge}, is shifted by $\frac{\chi}{2}$ for every single photon present in the resonator. Consequently, any random fluctuations in the number of photons, $\delta\bar{n}(t) = \hat{a}^\dagger\hat{a} - \langle \hat{a}^\dagger\hat{a} \rangle$, will act as a direct source of frequency noise for the qubit:

$$\delta\omega_{ge}(t) = 2\chi\bar{n}(t) \tag{85}$$

The factor of 2 arises because the dispersive shift affects both qubit states with opposite signs, doubling the frequency difference between them.

The number of photons in the resonator fluctuates because the resonator is coupled to an environment, causing photons to randomly leak out at a rate κ. For a resonator with an average photon number $\bar{n}$, this process creates noise with a Lorentzian power spectrum[120]: $S_{\bar{n}}(\omega) = \frac{\kappa}{\pi}\frac{\bar{n}(\bar{n}+1)}{\kappa^2+\omega^2}$. This allows us to simplify the spectrum by taking its value at frequencies much smaller than the resonator linewidth, where it is nearly constant: $S_{\bar{n}}(\omega \ll \kappa) = \frac{\bar{n}(\bar{n}+1)}{\pi\kappa}$.

This flat spectral response in the relevant frequency range simplifies the analysis of dephasing effects. For Hahn-Echo sequences, the dephasing can be calculated using the filter function approach. The decay function becomes:

$$f_E(t) = \exp\left[-\frac{t^2}{2}\left(\frac{\partial\omega_{ge}}{\partial\bar{n}}\right)^2 \int_{-\infty}^{\infty} d\omega S_{\bar{n}}(\omega \ll \kappa)\sin^2\left(\frac{\omega t}{4}\right)\mathrm{sinc}^2\left(\frac{\omega t}{4}\right)\right] \tag{86}$$

Because $\partial_{\bar{n}}\omega_{ge} = 2\chi$ and the photon noise spectrum is approximately flat over the relevant frequency range; this integral evaluates to:

$$f_E(t) = \exp\left[-t\frac{4\chi^2}{\kappa}\bar{n}(\bar{n}+1)\right] \tag{87}$$

The resulting photon noise dephasing rate is:

$$\Gamma_\varphi^{\bar{n}} = \frac{4\chi^2}{\kappa}\bar{n}(\bar{n}+1) \tag{88}$$

The photon shot noise dephasing rate exhibits several important characteristics. The dependence on $\bar{n}(\bar{n}+1)$ reflects the quantum nature of photon statistics, where both the classical term $\bar{n}^2$ and the quantum correction $\bar{n}$ contribute to fluctuations. For large photon numbers, the dephasing scales approximately as $\Gamma_\varphi^{\bar{n}} \propto \bar{n}^2$.

The inverse dependence on κ indicates that broader resonator linewidths help suppress photon shot noise by reducing the correlation time of photon number fluctuations. However, this must be balanced against other considerations such as readout fidelity and Purcell decay rates.

The quadratic dependence on the dispersive shift $\chi = g^2/\Delta$ shows that stronger coupling (larger g) or smaller detuning (smaller Δ) both increase susceptibility to photon noise. This

creates a fundamental trade-off between the coupling strength needed for fast quantum operations and the coherence degradation from photon fluctuations.

Charge Noise

Charge fluctuations couple to flux qubits through the charging energy of Josephson junctions. While flux qubits are inherently less sensitive to charge noise than charge qubits, residual coupling can contribute to dephasing, particularly when operating away from charge-insensitive points.

The charge noise spectrum typically exhibits 1/f characteristics: $S_Q = \frac{A_Q}{|\omega|}$ with amplitude $\sqrt{A_Q} \approx 10^{-3}\ \frac{e}{\sqrt{Hz}}$ for typical devices. The charge dephasing rate for a flux qubit is:

$$\Gamma_\varphi^C = \sum_{i=1,2,3} \sqrt{A_Q} \left(\frac{\partial \omega_{01}}{\partial n_i}\right) \sqrt{\ln(2)} \tag{89}$$

where n_i represents the charge on the i-th superconducting island. The decay rate can be estimated numerically by simulating the Hamiltonian of the qubit with different charge states on each superconducting island.

2.8 Randomized Benchmarking

Quantum process tomography (QPT) requires computational resources that scale exponentially with system size, making it impractical for larger quantum devices. Moreover, estimating the fidelity of a gate requires to compensate for readout and preparation errors.

Randomized Benchmarking (RB) addresses this challenge by providing a scalable, statistically robust method for characterizing average gate error rates without requiring precise knowledge of state preparation and measurement (SPAM) errors[121,122]. Unlike traditional QPT, which suffers from exponential scaling and sensitivity to SPAM errors, RB offers a practical framework for evaluating gate performance that is directly relevant to quantum computing applications.

2.8.1 The Clifford Group

RB circumvents these limitations by estimating average gate error rates through stochastic sampling of random gate sequences. The protocol employs gates from the Clifford group, C_n,

defined as the finite subgroup of unitary operators that preserve the Pauli group under conjugation:

$$C_n = \{U \in \mathcal{U}(2^n) : UP_iU = P_j\} \quad (90)$$

where P_i and P_j represent Pauli operators[123].

The n-qubit Clifford group possesses several properties that make it suitable for benchmarking applications. First, it is generated by a small set of elementary gates, for example: the Hadamard gate, phase gate, and controlled-NOT gate[123]. Second, the group structure enables efficient classical simulation according to the Gottesman-Knill theorem, facilitating the computation of expected outcomes[124]. Most importantly for RB, random sampling over Clifford operations effectively converts arbitrary noise channels into depolarizing channels through the twirling property[122]. This transformation reduces complex, multi-parameter noise models into a single-parameter depolarizing channel, enabling direct extraction of average gate error rates from simple exponential decay fits.

2.8.2 Sequence Construction and Measurement Protocol

An RB sequence contains *m*+1 quantum operations:

1. **Random gates**: *m* gates $(C_1, C_2, \dots, C_m)$ selected uniformly at random from the Clifford group.
2. **Correction gate**: C_{m+1} chosen to ensure the complete sequence implements the identity operation in the absence of errors.

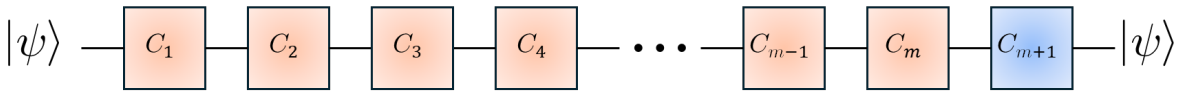

Figure 19 – Randomized benchmarking sequence | The first m operations C_i (orange) that are acting on the quantum state $|\psi\rangle$ are chosen randomly from the Clifford set, while the last operation C_{m+1} (blue) is selected to ensure the entire sequence is equal to the identity operator.

The correction gate is uniquely determined by the group property of Clifford operations:

$$C_{m+1} = (C_m \circ C_{m-1} \circ \dots \circ C_1)^\dagger = C_1^\dagger \circ C_2^\dagger \circ \dots \circ C_m^\dagger$$

In the ideal, error-free case, every RB sequence implements the identity: $C_{m+1} \circ C_m \circ \dots \circ C_1 = \mathbb{I}$. Any deviation from identity behavior directly reflects the presence of errors.

The measurement protocol exploits the fact that ideal RB sequences leave the input state unchanged. We prepare an initial state ρ (typically $|0\rangle\langle 0|$) and measure how likely we are to recover this state after applying the RB sequence. For a specific sequence labeled by index set $\mathrm{i}_m = \{i_1, i_2, \ldots i_m\}$, the survival probability is[125]:

$$p_{\mathrm{i}_m}(\psi) = \mathrm{Tr}\left[E_\psi S_{\mathrm{i}_m}(\rho)\right] \tag{91}$$

where S_{i_m} represent the noisy RB sequence and E_ψ is the positive operator-valued measure element for detecting the initial state ψ.

In realistic implementations, each gate suffers from imperfections. We model each noisy gate as the composition of an ideal Clifford operation C_{i_j} followed by an error channel $\Lambda_{i_j,j}$. The complete noisy RB sequence becomes:

$$S_{\mathrm{i}_m} = \Lambda_{i_{m+1},m+1} \circ C_{i_{m+1}} \circ \Lambda_{i_m,m} \circ C_{i_m} \circ \ldots \circ \Lambda_{i_1,1} \circ C_{i_1} \tag{92}$$

The error $\Lambda_{i_j,j}$ can depend on which specific gate i_j is applied and on the position j in the sequence. Moreover, typically the noise is considered Markovian, that is each error is independent of previous operations.

Because each random sequence gives a different survival probability, we must average over many sequences to extract meaningful information. For sequences of fixed length *m*, we define:

$$\bar{p_m}(\psi) = \frac{1}{|\mathrm{i}_m|}\sum_{\mathrm{i}_m} p_{\mathrm{i}_m}(\psi) = \frac{1}{|\mathrm{i}_m|}\sum_{\mathrm{i}_m} \mathrm{Tr}\left[E_\psi S_{\mathrm{i}_m}(\rho)\right] \tag{93}$$

To make analytical progress, we assume that gate errors are approximately independent of both the specific gate and its position in the sequence $\Lambda_{i_j,j} = \Lambda$. This approximation is valid when all gates suffer from similar dominant noise sources, gate-to-gate variations are small compared to the average error, and systematic drifts over sequence duration are negligible. Under this approximation, we can evaluate the average sequence operator analytically.

The average sequence operator $\bar{S_m} = \frac{1}{|\mathrm{i}_m|}\sum_{\mathrm{i}_m} S_{\mathrm{i}_m}$ can be written explicitly as:

$$\bar{S}_m = \Lambda \circ \left[\frac{1}{|C_n|}\sum_{C \in C_n} C^\dagger \circ \Lambda \circ C\right]^{\circ m} \tag{94}$$

The expression in brackets is the twirling of channel Λ over the Clifford group $\Lambda_T = \frac{1}{|C_n|}\sum_{C\in C_n} C^\dagger \circ \Lambda \circ C$. For any quantum channel Λ, averaging over random Clifford gates makes it look like a depolarizing channel that changes quantum states toward the maximally mixed state. Hence, the twirling of a single channel is given by $\Lambda_T(\rho) = p\rho + \frac{1-p}{d}$, where $d = 2^n$ and p represents the depolarizing parameter. Composition of m consecutive twirls results with $\Lambda_T^{\circ m} = p^m\rho + \frac{1-p^m}{d}$ and the average sequence fidelity becomes:

$$F(m,\psi) = \mathrm{Tr}\left(E_\psi \bar{S}_m(\rho)\right) = A_0 p^m + B_0 \tag{95}$$

where $A_0 = \mathrm{Tr}\left[E_\psi \Lambda\left(\rho - \frac{1}{d}\right)\right]$ and $B_0 = \mathrm{Tr}\left[E_\psi \Lambda\left(\frac{1}{d}\right)\right]$ account for the SPAM errors.

The average error rate over the entire Clifford set, defined as the average error per twirl, is related to the depolarizing parameter p through:

$$r = 1 - \underbrace{\left(p + \frac{1-p}{d}\right)}_{F(1,\psi)} = \frac{(d-1)(1-p)}{d} \tag{96}$$

As Clifford gates are composed of multiple primitive gates, we must account for the average gate count. Using our generating set $\left\{I, X_{\pm\frac{\pi}{2}}, X_{\pm\pi}, Y_{\pm\frac{\pi}{2}}, Y_{\pm\pi}\right\}$ with average length 1.875 primitive gates, the error rate per gate is $r_g = r/1.875$.

The complete set of Clifford operators used in our implementation is provided in Appendix 7.1.

2.8.3 Interleaved Randomized Benchmarking

Standard RB provides error rates averaged over the entire Clifford group, but quantum computing applications require characterization of specific gate implementations. Interleaved RB (IRB) addresses this need by enabling targeted assessment of individual gates within the Clifford group through a comparative measurement protocol[126].

The IRB protocol consists of two distinct measurement phases. First, standard RB is performed on random sequences of Clifford gates to establish a reference baseline, yielding the composite depolarizing parameter p_{ref} for the entire gate set. Second, sequences are constructed by systematically interleaving a specific target gate C of interest between uniformly random Clifford elements.

For a sequence of length m, the interleaved protocol applies the pattern: $C_1C - C_2C - \ldots - C_mC - C_{m+1}$, where each C_i represents a uniformly random Clifford operation, C is the target gate, and C_{m+1} is the correction gate ensuring the complete sequence implements the identity operation. This construction results in m applications of the target gate interspersed with m random Clifford gates as illustrated in Figure 20.

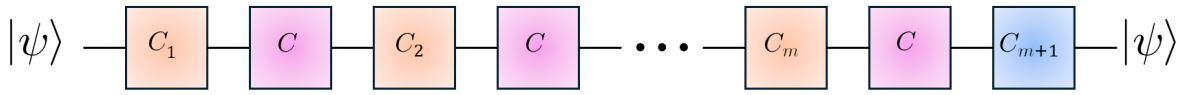

Figure 20 – Interleaved randomized benchmarking sequence | The gate of interest C (pink) is interleaved between m random Clifford operations C_i (orange). The final operation C_{m+1} (blue) is chosen such the entire sequence do not change the quantum state $|\psi\rangle$.

The key insight underlying IRB is that the interleaved sequences probe the combined error of random Clifford operations and the specific target gate. If we denote the error channel associated with the target gate as ϵ_C and the average error channel for random Clifford operation as ϵ_{avg}, then the interleaved sequence experiences the composite error process. The interleaved sequence fidelity follows the same decay as the standard sequence. Thus, using Equation 95 the composite depolarizing parameter for sequences containing the target gate p_C can be extracted.

The derivation of the specific gate error rate relies on the relationship between the composite and reference depolarizing parameters. The depolarizing parameter for a sequence containing both random Clifford operations and the target gate can be expressed as $p_C = pp_{gate}$, where p_{gate} is the depolarizing parameter associated specifically with the target gate C. This multiplicative relationship arises because each gate in the sequence contributes independently to the overall depolarization under the twirling approximation. The average gate error rate for random Clifford operation is $r_{ref} = \frac{(d-1)(1-p)}{d}$. Similarly, the composite error rate for interleaved sequences is $r_C = \frac{(d-1)(1-p_C)}{d}$. The specific gate error rate can then be isolated by recognizing that $p_C = pp_{gate}$, which gives $p_{gate} = p_C/p$. Substituting this into the error rate formula (Equation 96) yields:

$$r_{gate} = \frac{d-1}{d}\left(1 - \frac{p_C}{p}\right) \tag{97}$$

This expression directly relates the specific gate error to the experimentally measured depolarizing parameters from both standard and interleaved RB measurements. The bound for Equation 97 are given by $r_{gate} \pm E$, with[126]:

$$E = \min \begin{cases} \frac{d-1}{d}\left[\left|p - \frac{p_C}{p}\right| + 1 - p\right] \\ \frac{2}{p}\left[\frac{d^2-1}{d^2} + 2\sqrt{1-p}\sqrt{d^2-1}\right] \end{cases} \quad (98)$$

2.9 Coupling Flux Qubit To Mechanical Resonator

The coupling of the flux qubit to the mechanical resonator is based on the same interaction Hamiltonian described in the section Coupling to Artificial Atoms which takes the form:

$$\hbar\omega_m \hat{b}^\dagger \hat{b} + \hbar\frac{\Delta}{2}\hat{\sigma}_z + \hbar g_m \hat{\sigma}_x\left(\hat{b} + \hat{b}^\dagger\right) \quad (99)$$

with ω_m the mechanical frequency, $\hat{b}^\dagger$, $\hat{b}$ the creation and annihilation operators. Δ is the energy splitting of the flux qubit, $\hat{\sigma}_i$ are the Pauli operators. g_m is the coupling strength. The flux dependency of the qubit's energy is through $\epsilon = \frac{2I_p}{\hbar}\left(\Phi - \frac{\Phi_0}{2}\right)$, where I_p is the persistent current and Φ the magnetic flux threading the loop of the qubit. Thus, the coupling can be expressed in equivalence to the magnetic coupling derived in the Quantum Optomechanics and Electromechanics section as $g_m = \frac{\partial\epsilon}{\partial\Phi}\Phi_{\text{ZPF}}$. Φ_{ZPF} is the magnetic flux fluctuation induced in the flux qubit due to the mechanical motion of the resonator.

For a parallel magnetic field $B_\parallel$ acting on a flux qubit with a vibrating beam of length L as an arm $\Phi_{ZPF} = \gamma B_\parallel L x_{ZPF}$, where $\gamma \sim 0.5$ is a scaling factor that depends on the mechanical mode shape. Hence, the coupling is $g_m = \frac{2I_p}{h}\gamma B_\parallel L x_{ZPF} \approx 217$ kHz for typical parameters of $I_p =$ 300 nA, $B_\parallel = 100$ G, $L =$ 800 nm and $x_{ZPF} =$ 60 fm.

To couple the motion of a vibrating membrane to the flux qubit, one arm of the qubit's loop can be positioned along the center line of the membrane. In that case, the coupling has the same form $g_m/B_\parallel = \frac{2I_p}{h}\gamma(2R)x_{ZPF}$ as in the case of vibrating beam. For a silicon membrane of $R = 1$ μm and $x_{ZPF} = 2.5$ fm, the coupling to the fundamental vibration mode is $g_m \approx$ 36 kHz, with $B_\parallel = 100$ G and $\gamma_{0,1} = 0.5269$.

Type	Material	Size	Frequency	Q	x_{ZPF}	g
Beam	Diamond	$L = 800$ nm	$f = 1.013$ GHz	$Q = 30{,}088$	60 fm	21.7 MHz/T
Membrane	Silicon	$R = 1000$ nm	$f_{01} = 384$ MHz	$Q_c \approx 3000$	2.5 fm	3.58 MHz/T

3. Sample Design And Fabrication

3.1 Mechanical Resonators Fabrication

The successful realization of the proposed architecture in this thesis relies on the development of high-quality mechanical resonators. This section outlines the fabrication techniques established to produce two such devices: diamond nano-beams and silicon membranes. We will detail the multi-step processes engineered for each material system.

3.1.1 Nano-Beam Fabrication

To overcome the limitations of fabricating devices from single-crystal diamond, we collaborated with the Finkler Lab at the Weizmann Institute of Science (WIS) to employ an angled-etching technique that uses anisotropic, oxygen-based plasma[127]. This method utilizes a custom-designed Faraday cage to direct plasma ions toward the substrate at specific angles. This allows for the fabrication of suspended structures with triangular cross-sections directly from a bulk diamond substrate, as shown in Figure 21.

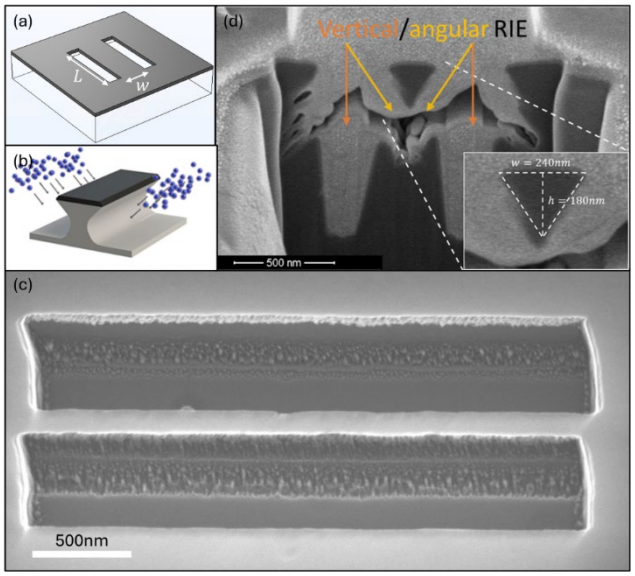

Figure 21 – Nano-beam fabrication using the angled-etching technique | (a) Schematic of the 20 nm thick Ti hard mask used to define the etch area. (b) Illustration of the angular RIE process that undercuts the mask to form the suspended beam. (c) Tilted-view (20°) scanning electron micrograph (SEM) of a fabricated nano-beam with length $L = 2.9$ μm and width $w = 125$ nm. (d) Cross-sectional SEM showing triangular geometry; dark regions represent diamond; bright regions show conductive

Ti coating for imaging. Inset shows geometric approximation of triangular cross-section. Panel (b) is adapted from reference 127.

The fabrication sequence begins at WIS with rigorous surface preparation of the diamond substrate, which includes ultrasonic cleaning in acetone followed by a heated tri-acid solution (NHO_3:H_2SO_4:$HClO_4$) to ensure optimal surface conditions. Next, alignment marks are patterned using photolithography, followed by the deposition of a 30 nm titanium (Ti) layer and liftoff in acetone. Next, the sample is delivered to our laboratory.

The nano-beam geometry is then defined using electron-beam lithography in a PMMA resist. The final beam's length (L) and width (w) are set by the dimensions of, and distance between, pairs of rectangles patterned in the resist. Following development of the resist, a 20 nm Ti layer is deposited at WIS to act as a durable hard mask for the subsequent etching steps.

The diamond is etched in a two-stage process. First, a vertical reactive-ion etch (RIE) using oxygen (O_2) and chlorine (Cl_2) plasma transfers the hard mask pattern into the diamond substrate. Second, a tent-assisted angular etch with O_2:Cl_2 plasma undercuts the structures, releasing the free-standing nano-beams, as illustrated in Figure 21b. Finally, the Ti mask is stripped, and the diamond is cleaned in a piranha solution to complete the process.

The key parameters for each step of the fabrication process are summarized in Table 3.

Table 3 – Fabrication steps of diamond nano-beams.

Process	Description
Surface Preparation	WIS
Solvents cleaning	Acetone ultrasonic bath
Acid cleaning	NHO_3:H_2SO_4:$HClO_4$ (1:1:1) at 180° C
Alignment Mark Formation	WIS
Spin coating	S1805: 4000 rpm, 40 s; bake 110° C, 1 min
UV lithography	70 mJ cm^{-2} (MicroWriter ML®3)
Development	MF319 developer, 40 s
Metal deposition	Ti layer, 30 nm (Odem Selene)
Liftoff	Acetone
Nano-beam Pattern Definition	BIU
Spin coating	PMMA 950A3: 4000 rpm, 60 s; bake 180° C, 5 min
E-beam lithography	50KeV, 30 pA; dose 500 μC cm^{-2} (Crestec-CABL)
Development	MIBK:IPA (1:3), 45 s
	WIS
Metal deposition	Ti hard mask, 20 nm (Odem Selene)
Liftoff	Acetone

Diamond Etching	WIS
Vertical etching	O_2:Cl_2 (50:2 sccm), 10 mbar, 700 W ICP
Angular etching	O_2:Cl_2 (50:2 sccm), 10 mbar, 1000 W ICP
Final cleaning	WIS
Acid cleaning	Piranha solution (H_2SO_4:H_2O_2, 3:1)

This fabrication process yields free-standing diamond nano-beams. Figure 21c shows a scanning electron micrograph (SEM) of an exemplary beam with a length $L = 2.9$ µm and width $w = 125$ nm. An SEM micrograph of a beam's triangular cross-section is shown in Figure 21d.

3.1.2 Silicon Membrane Fabrication

For the fabrication of silicon (Si) membranes, we developed a technique that uses a silicon oxide (SiO_2) sacrificial layer on a silicon-on-insulator (SOI) wafer. The core concept is to create a nano-scale hole in the top Si device layer and then use an isotropic wet etch to remove the buried oxide layer. This process defines a fully clamped circular membrane whose radius is determined by the etching time.

The fabrication process, illustrated schematically in Figure 22, begins with a piranha cleaning of a SOI wafer, which consists of a 220 nm Si device layer, a 3 µm buried oxide layer, and a 130 µm Si base layer.

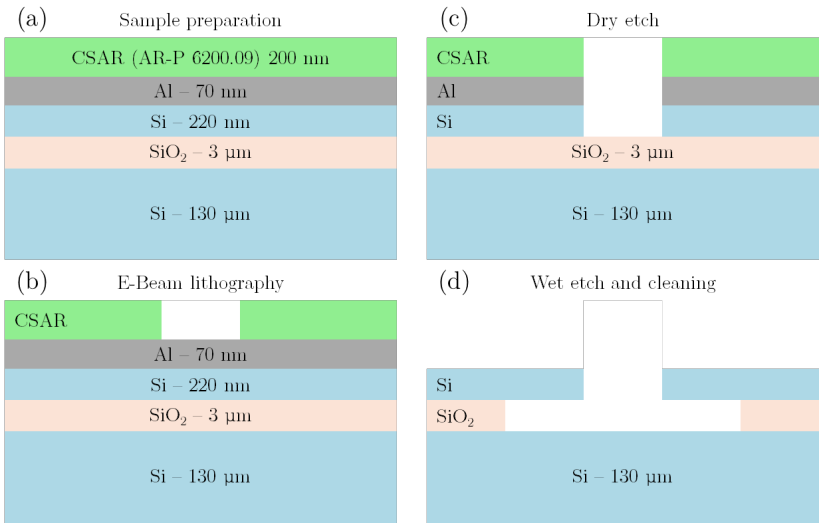

Figure 22 – Schematic of the Si membrane fabrication process.

A 70 nm Al layer is evaporated onto the top device layer to serve as a conductive layer for the e-beam lithography and a hard mask for the Si etching. The etching holes are patterned using

electron-beam lithography in a CSAR resist. The pattern is then transferred into the top Al layer via reactive-ion etching (RIE) with BCl_3. After the pattern transfer, the CSAR resist is removed by O_2 plasma ashing. With the Al acting as a hard mask, the pattern is etched through the Si device layer using RIE with SF_6. In the final step, the wafer is submerged in hydrofluoric (HF 48%) acid, which selectively removes the buried SiO_2 layer through the etched hole, leaving a suspended, circular Si membrane as shown in Figure 23.

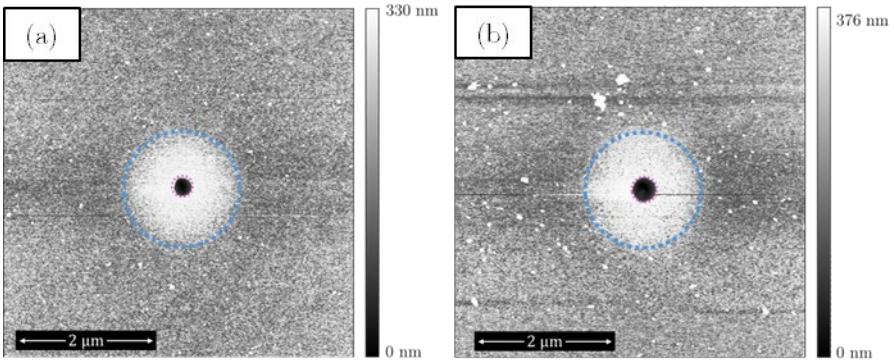

Figure 23 – Atomic force microscope (AFM) scans of fabricated Si membranes | The images show topography of two different circular membranes, with the blue dashed lines indicating the membrane edges at a radius of 1.65 µm. The central holes used for etching are marked with pink dashed lines. (a) A membrane fabricated with a 290 nm diameter etch hole. (b) A membrane fabricated with a 360 nm diameter etch hole. A height difference of 1 nm is visible in the regions where the buried oxide was etched.

The key parameters for each fabrication step are summarized in Table 5.

Table 4 – Etching Rates.

Material	Etch Process	Etch Rate [nm/s]
Si	RIE, SF_6	1.5-2.5
Al	RIE, BCl_3	1.15-1.3
SiO_2	HF 48%	1.3-1.5

Table 5 – fabrication steps of Si membranes.

Process	Description
Surface Preparation	
Solvents cleaning	Acetone ultrasonic bath
Acid cleaning	NHO_3:H_2SO_4:$HClO_4$ (1:1:1) at 180° C
Metal deposition	
Backside Sputtering	Al, 350 nm (Intelvac Nano Quest)
Topside e-beam evaporation	Al, 70 nm (Plassys MEB 550S)
Holes Pattern Definition	

Spin coating	CSAR (AR-P 6200.09): 4500 rpm, 60 s; bake 100° C, 5 min
E-beam lithography	50KeV, 30 pA; dose 500 μC cm^{-2} (Crestec-CABL)
Development	MIBK:IPA (1:3), 45 s
Al etching	RIE: BCl_3 (Versaline SLR 770)
Resist removal	O_2 plasma ashing, 10 min
Si etching	RIE: SF_6 (20 sccm), 20W (Versaline SLR 770)
SiO_2 etching	HF 48%
Final cleaning	
Acid cleaning	Piranha solution (H_2SO_4:H_2O_2, 3:1)

3.2 Superconducting Resonators Fabrication

The hybrid quantum systems explored in this thesis require the integration of mechanical elements with high-coherence superconducting circuits. This section outlines the fabrication techniques developed to produce two such circuits: $\lambda/2$ coplanar resonators on diamond, and Bragg resonators on silicon.

3.2.1 $\lambda/2$ Coplanar Resonators on Diamond

This section describes the design and fabrication of standard capacitively-terminated $\lambda/2$ coplanar waveguide resonators on diamond substrates. An example of such a resonator is shown in Figure 24. We pursued two primary objectives with these resonators: determining the relative permittivity and measuring the loss tangent of the diamond substrates.

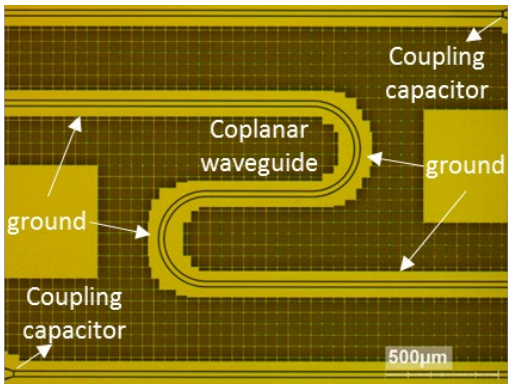

Figure 24 – $\lambda/2$ coplanar waveguide resonator | Optical micrograph of a resonator fabricated from 150 nm niobium film on diamond substrate. The serpentine geometry achieves the target length for $\omega_0 = 7.5$ GHz resonance, with interdigitated coupling capacitors ($C_c = 0.9$ fF, $Q_c = 1.75 \times 10^5$) providing controlled coupling to the 50 Ω feedline.

The resonator is designed as a coplanar waveguide (CPW) consisting of a central conductor of length $l = 10.875$ mm and width $w = 21$ μm placed between two ground planes separated by distance $h = 4$ μm from the central conductor. The resonance frequency of the resonator

is given by $f_r = \frac{1}{2l} v_{ph}$, where $v_{ph} = \frac{c}{\sqrt{\epsilon_{\text{eff}}}}$ is the phase velocity with c the speed of light in vacuum and $\epsilon_{eff} = \frac{1+\epsilon_r}{2}$ is the effective dielectric constant. The dielectric constant of the diamond substrate is $\epsilon_r = 5.7$.

For electromagnetic waves, the phase velocity $v_{ph} = 1/\sqrt{\mathcal{LC}}$ also relates to the capacitance $\mathcal{C}$ and inductance $\mathcal{L}$ per unit length[128]. The impedance of the CPW is given by $Z_0 = \sqrt{\mathcal{L}/\mathcal{C}}$.

The capacitance is given by $\mathcal{C} = 4\epsilon_0\epsilon_{eff}\frac{K(k_0)}{K(k_0')}$. For superconducting films, the total inductance $\mathcal{L} = \mathcal{L}_g + \mathcal{L}_k$ has contributions from both geometric $\mathcal{L}_g$ and kinetic $\mathcal{L}_k$ inductances. The value of the geometric inductance is given by $\mathcal{L}_g = \frac{\mu_0}{4}\frac{K(k_0')}{K(k_0)}$, where K is the complete elliptic integral of the first kind, $k_0 = \frac{w}{w+2h}$, and $k_0' = \sqrt{1-k_0^2}$. The geometric inductance is related to the sheet resistance R_s of the superconducting film via the relation $\mathcal{L}_k = \frac{\hbar R_s}{1.76\pi k_B T_c}$, with $\hbar$ and k_B the reduced Planks' and Boltzmann's constants and T_c the superconducting critical temperature of the film. The parameters of our superconducting layers and the result CPW resonators are shown in Table 6.

Table 6 – Design parameters of the CPW resonators.

Metal	Thickness	T_c	R_s	$\mathcal{L}_k$	Z_0	f_r^{sim}	C_c	Q_c
Al	150 nm	1.9 K	0.19 Ω/sq.	6.74 nH/m	50.73 Ω	7.449 GHz	0.9 pF	1.75×10^5
Nb	150 nm	8.7 K	1.00 Ω/sq.	7.65 nH/m	50.81 Ω	7.438 GHz	0.9 pF	1.75×10^5

The total quality factor $Q_t^{-1} = Q_l^{-1} + Q_c^{-1}$ is determined by internal losses (Q_l) and coupling to the drive line (Q_c). The coupling quality factor is controlled by the coupling capacitors C_c, with $Q_c^{-1} = \frac{4}{\pi}(Z_0\omega_r C_c)^2$ for two identical capacitors. The internal quality factor relates to the substrate loss tangent through $Q_l^{-1} = p\tan\delta$, where $p = \frac{\epsilon_{eff}}{\epsilon_{eff}+1}$ is the participation ratio. In the regime $Q_c \gg Q_l$, the total quality factor is governed by internal losses: $Q_t \approx Q_l$.

The VNA transmission signal for a microwave resonator with two identical ports, given by input-output theory[129], follows $|S_{21}|^2 = \left(\frac{Q_t}{Q_c}\right)^2 \frac{1}{1+4Q_t^2\left(\frac{\omega-\omega_r}{\omega_r}\right)^2}$ with phase $\angle S_{21} = -\arctan\left(2Q_T\frac{\omega-\omega_r}{\omega_r}\right)$.

For this experiment, we used two types of diamond substrates from Element Six. The properties of both samples are summarized in Table 7.

Table 7 – Properties of Diamond Samples.

Sample	Supplier	Dimensions [mm]	Type	Surface Roughness	Purity
A (SCLA_0062)	Element Six	6.4 × 6.3 × 0.5	Single crystal large area	Ra < 1 nm	N < 1 ppm
B (SCOP_1460)	Element Six	6.0 × 6.0 × 0.5	Single crystal optical grade (IIA)	Ra < 1 nm	N < 1 ppm B < 0.05 ppm

The fabrication process begins with rigorous surface cleaning through immersion in boiling (180° C) triacid solution (H_2SO_4:HNO_3;$HClO_4$, 1:1:1) using an air-cooled condenser (Radleys Findenser) with silica ball filter to maintain reflux, as shown in Figure 25a. This enables 24-hour cleaning cycles that result with pristine surface as presented in Figure 25b and Figure 25c.

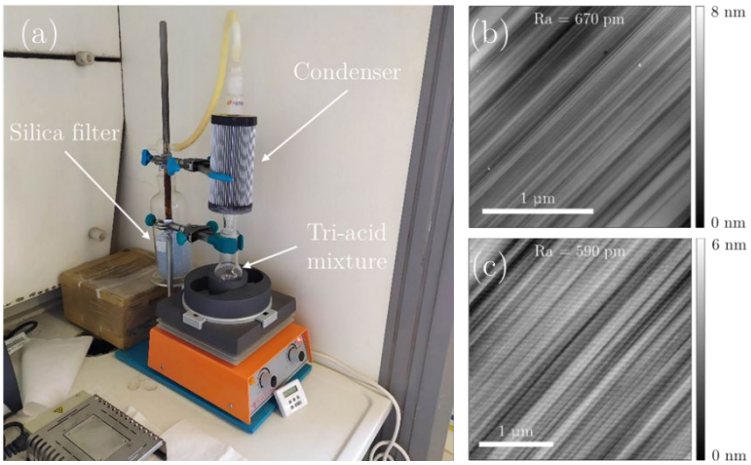

Figure 25 – Surface preparation and characterization | (a) Custom triacid cleaning setup with reflux condenser and silica ball filter enabling extended 24-hour cleaning cycles at 180°C. AFM topography images showing surface quality after cleaning for (b) Sample A and (c) Sample B, both achieving Ra < 1 nm roughness.

Following cleaning, samples are rinsed with deionized water, dried with nitrogen, and baked at 180°C to promote outgassing before transfer to the e-beam evaporator load chamber. Samples remain in the evaporator chamber overnight until reaching 10^{-7} mbar vacuum. To achieve 10^{-8} mbar, titanium is first evaporated as a gettering material for two minutes while the sample surface is protected with a mechanical shutter. The superconducting metal (Nb or Al) is then deposited onto the clean diamond surface. Device patterns are subsequently

defined using direct laser lithography in photoresist, followed by pattern transfer through etching.

For aluminum resonators, we employ AZ1505 photoresist for lithography and transfer the pattern through wet etching with type-A Al-etchant followed by brief AZ726 immersion. The niobium fabrication process is more complex, utilizing AZ1512 photoresist and a multi-step etching approach. The first step involves reactive ion etching with BCl_3-Cl_2 gas, monitored by laser interferometry to prevent diamond damage. The etching is stopped before the Nb layer is completely etched and the remaining thin Nb layer is then removed using triacid for 10 minutes after bubble formation. This approach achieves complete removal of thin etched regions while preserving thick patterned areas, as demonstrated in Figure 26a. Finally, samples are mounted on custom printed circuit boards and connected via wire bonding. Summary of the fabrication steps is given in Table 8.

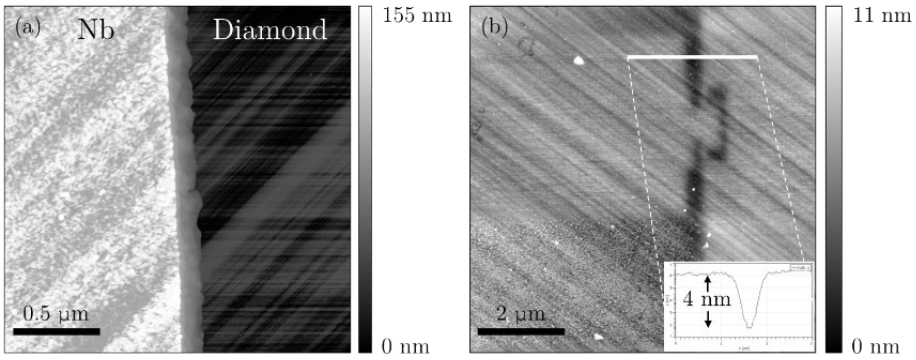

Figure 26 – Etching process outcomes and substrate reuse challenges | (a) AFM micrograph showing clean Nb step profile (150 nm height) achieved through combined RIE and triacid etching, demonstrating selective material removal without diamond substrate damage. (b) Qubit pattern (dark features) etched in the diamond surface, most likely due to oxygen plasma ashing. Inset: Height profile along the white line with 4 nm negative step.

Due to the high cost of diamond substrates, extensive reuse was necessary. We observed persistent device patterns on diamond surfaces even after comprehensive cleaning including triacid treatment, piranha solution, organic solvent sonication, and oxygen plasma ashing. Under AFM, as shown in Figure 26b, we detected that pattern is etched into the diamond. We attribute the etching of the diamond to the oxygen plasma ashing conducted through the qubit mask, as described later.

Table 8 – Fabrication steps of superconducting CPW resonators.

Process	Description
Surface Preparation	

Solvents cleaning	Acetone ultrasonic bath
Acid cleaning	NHO_3:H_2SO_4:$HClO_4$ (1:1:1) at 180° C
Al Resonator Formation	
Metal deposition	Al layer, 150 nm at 0.5 nm s^{-1} (Plassys MEB 550S)
Adhesion promotion	Bake: 180°C for 10 min
	Plasma ashing: O_2N_2, 5min
Spin coating	AZ1505 photoresist: 5000 rpm, 60 s; bake 80° C, 5 min
UV lithography	MLA150: dose = 23 mJ cm^{-2}, $\lambda = 405$ nm
Development	AZ726 developer: 45s; hard bake 120°C for 5min
Metal etching	Al etchant type A: 10min
	AZ726 developer: 1min
Nb Resonator Formation	
Metal deposition	Nb layer, 150 nm at 0.3 nm s^{-1} (Plassys MEB 550S)
Spin coating	AZ1512 photoresist: 5000 rpm, 60 s; bake 100° C, 45 s
UV lithography	MLA150: dose = 40 mJ cm^{-2}, $\lambda = 405$ nm
Development	AZ726 developer: 45s; hard bake 120°C for 5min
Metal etching	RIE: BCl_3-Cl_2 (Versaline SLR 770)
	NHO_3:H_2SO_4:$HClO_4$ (1:1:1): 180° C, 10 min
Final cleaning	
Solvents cleaning	NMP: 80° C, Overnight

Figure 27 shows resonator characterization employed by vector network analyzer (VNA) transmission measurements. The aluminum resonator on Sample A showed measured resonance frequency $f_r = 7.480$ GHz and total quality factor $Q_t = 4.21 \times 10^5$. The total quality factor is larger than the intended coupling quality factor, which indicates we had a design error, hindering the calculation of the internal quality factor. Accordingly, we can only put an upper limit on the loss tangent $\tan\delta < \frac{1}{Q_t} = 2.38 \times 10^{-6}$. The measurement was obtained with average number of photons inside the resonator $\bar{n} \approx 20$.

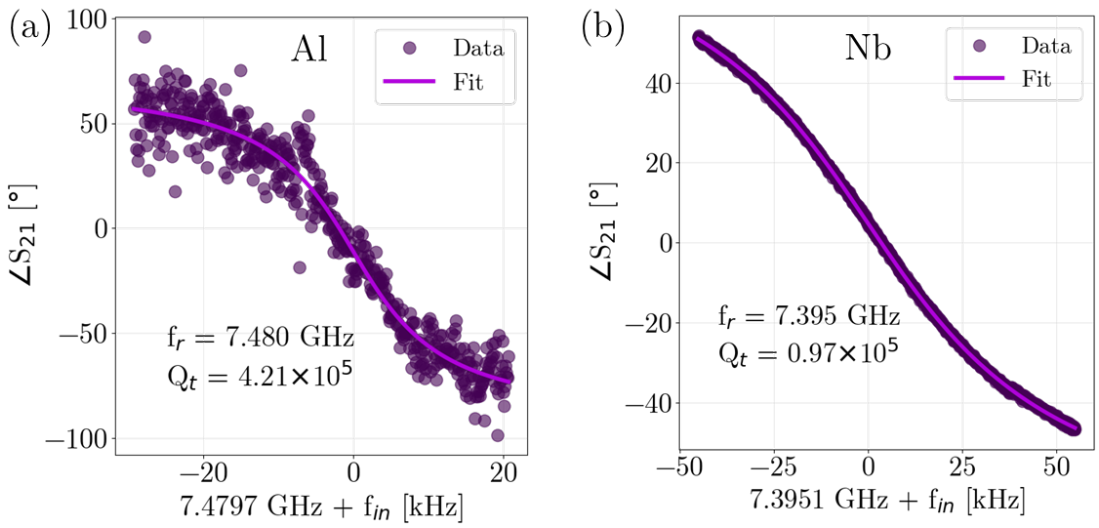

Figure 27 – VNA transmission characterization of $\frac{\lambda}{2}$ CPW resonators | (a) Aluminum resonator on Sample A showing $f_r = 7.480$ GHz with $Q_t = 4.21 \times 10^5$, yielding $\tan\delta < 2.38 \times 10^{-6}$ for the diamond substrate. (b) Niobium resonator on Sample B demonstrating $f_r = 7.395$ GHz with $Q_t = 9.71 \times 10^4$, corresponding to $\tan\delta < 1.03 \times 10^{-5}$.

The niobium resonator on Sample B demonstrated measured resonance frequency $f_r = 7.395$ GHz and total quality factor $Q_t = 9.71 \times 10^4$. The upper bound on the loss tangent is $\tan\delta < 1.15 \times 10^{-5}$.

Table 9 – Superconducting resonators results summary

Sample	f_r	$\lvert f_r - f_r^{sim} \rvert$	Q_t	$\tan\delta$
A	7.480	31 MHz	4.21×10^5	2.38×10^{-6}
B	7.395	43 MHz	9.71×10^4	1.03×10^{-5}

The aluminum resonator on the higher-grade substrate (Sample A) demonstrated superior performance with higher internal quality factor and lower loss tangent. This high internal quality factor ensures minimal additional losses from the readout resonator. While niobium fabrication is more complex, it offers advantages including enhanced SEM visibility for alignment mark location in subsequent qubit fabrication, resistance to piranha solution cleaning enabling device recovery from fabrication failures, and higher critical temperature reducing quasiparticle density. Aluminum provides simpler fabrication and stable native oxide protection, but devices are removed during piranha cleaning required for fabrication error recovery. Additionally, niobium oxidation is less uniform and stable, potentially degrading long-term performance compared to aluminum's superior electrical performance on high-grade substrates.

3.2.2 $\frac{3}{4}\lambda$ Resonator on Silicon

This section presents the design and fabrication of quarter-wave resonators implemented on silicon substrates. The resonator architecture, outlined in the Methodology chapter, comprises a 50-Ω transmission line with a Bragg reflector termination on one end and a ground short on the other, as illustrated in Figure 28. These devices serve dual purposes in our experimental setup: providing selective noise attenuation within a frequency band surrounding the qubit transition while maintaining transmission for control and readout signals, and enabling DC current injection for magnetic flux bias control of the qubit.

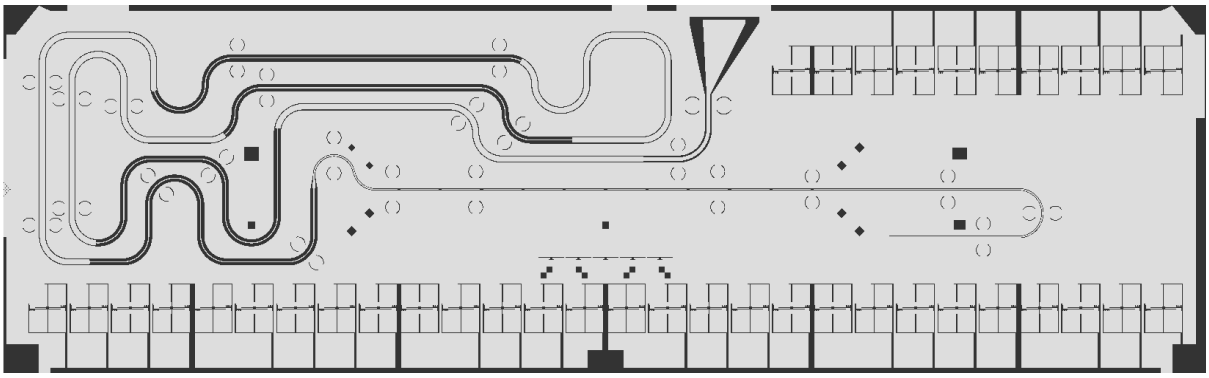

Figure 28 – Layout design of $\frac{3}{4}\lambda$ Bragg resonator on silicon substrate | The 50 Ω transmission line (center) terminates in a four-period impedance-alternating Bragg reflector ($Z_1 = 35\ \Omega$, $Z_2 = 80\ \Omega$) creating a stopband filter, while the opposite end connects to ground. The geometry enables both noise filtering around the qubit frequency and DC flux bias injection.

The substrate material consists of intrinsic silicon wafers with native oxide layers sourced from Virginia Semiconductors, featuring phosphorus impurity density less than 10^{12} cm^{-3}. Each wafer is segmented into 23 mm × 23 mm square sections, with individual sections containing 14 device sites measuring 3 mm × 10 mm, each hosting a single Bragg resonator structure.

Our design parameters target a transmission line length $L = 8.044$ mm, establishing a bare resonance frequency $\frac{\omega_0}{2\pi} \approx 11.09$ GHz. Here, we assume $\epsilon_r^s = 11.7$ for our silicon substrates. The width of the central line and the distance between the central line and the ground please were 10 and 5 μm respectively, yielding a characteristic impedance $Z_0 = 50\ \Omega$.

The Bragg reflector incorporates $m = 4$ impedance doublets with alternating characteristic impedances of $Z_1 = 35\ \Omega$ and $Z_2 = 80\ \Omega$. The low (high) impedance was achieved with center line width of 46 (8) μm and distance to the ground plane of 7 (26) μm. This impedance contrast yields a reflection coefficient magnitude $|r_{interface}| \approx 0.4$ and power reflectivity

$|r_{interface}|^2 \approx$ 15% at each interface. Each impedance section extends $L_B = 3.44$ cm in length. Electromagnetic simulations assuming lossless conditions predict the filter response shown in Figure 29, revealing a stopband centered at 8.58 GHz with nearly complete reflection $|r_B|^2 \approx 99\%$. At the design frequency of 11.09 GHz, the Bragg structure exhibits transmission $|t_B|^2 \approx$ 19% with phase $\angle r_B \approx 85°$. Linear fitting of the phase response near the filter center frequency yields an expected enhancement factor $\gamma = 1.52$.

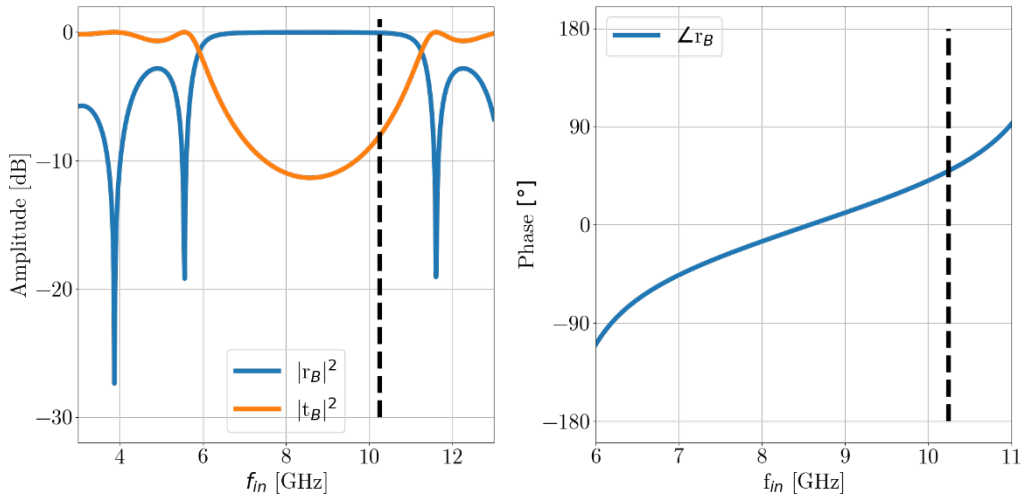

Figure 29 – Simulated response of Bragg resonator | $m = 4$, $Z_1 = 35\ \Omega$, $Z_2 = 80\ \Omega$.

The complete resonator phase response, depicted in Figure 30a, clearly demonstrates the modified phase velocity within the stopband region. The Bragg-modified resonance appears as a sharp phase discontinuity at $\frac{\omega_r}{2\pi} = 10.19$ GHz, with corresponding decay rate $\kappa_C = 82$ MHz and quality factor $Q_C = 780$. Current fluctuation simulations predict maximum values reaching $\delta_I = 30$ nA, as shown in Figure 30b.

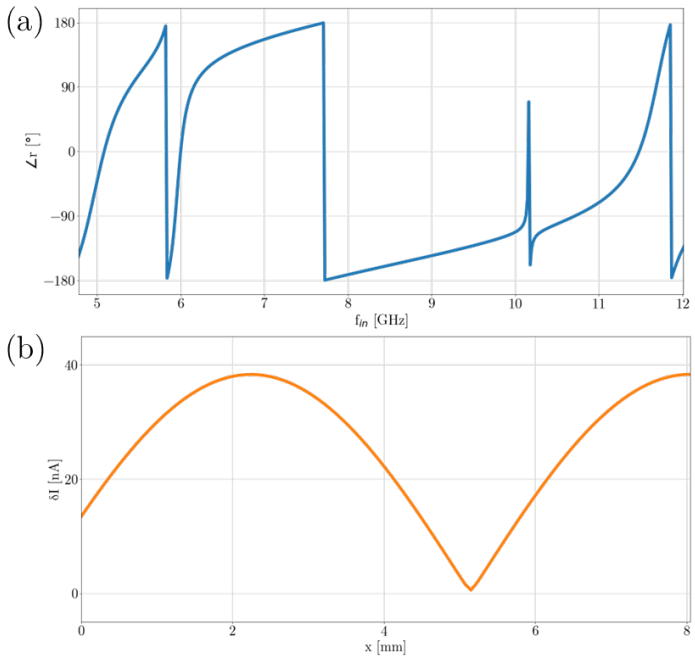

Figure 30 – Simulation of Bragg resonator | (a) Phase response of the reflected signal. (b) Current and voltage fluctuations.

Sample preparation follows a comprehensive surface treatment protocol to ensure optimal conditions for superconducting film adhesion. The process begins with sequential organic solvent cleaning using acetone and isopropyl alcohol to remove surface contaminants and particles. Subsequently, samples undergo aggressive chemical treatment in piranha solution (sulfuric acid and hydrogen peroxide mixture) at 120°C for 15 minutes, effectively eliminating residual organic compounds and metallic impurities. After thorough deionized water rinsing, samples are soaked in isopropyl alcohol, nitrogen-dried, and immediately loaded into the electron-beam evaporation system vacuum chamber. The subsequent metal deposition and photolithographic patterning procedures mirror those established for aluminum devices on diamond substrates, as depicted in the fabrication flow diagram of Figure 31.

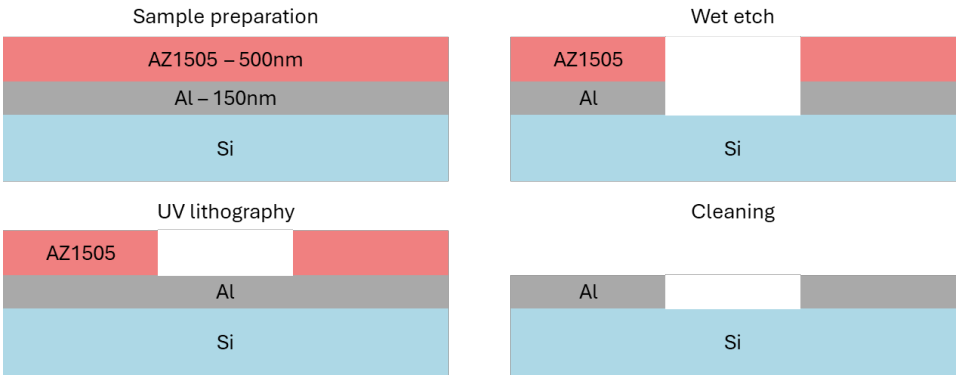

Figure 31 – Fabrication steps of superconducting aluminum devices.

Experimental characterization utilized vector network analyzer reflection measurements, with results presented in Figure 32. The measured resonance frequency was $\frac{\omega_r}{2\pi} = 10.162$ GHz, necessitating a correction to our estimated permittivity value to $\epsilon_r^s = 11.896$. This corresponds to an in-resonator light speed of $c = 118{,}060{,}115$ m·s^{-1}. The experimental decay rate $\kappa_C = 6.24$ MHz yielded a quality factor $Q_C \approx 10^4$.

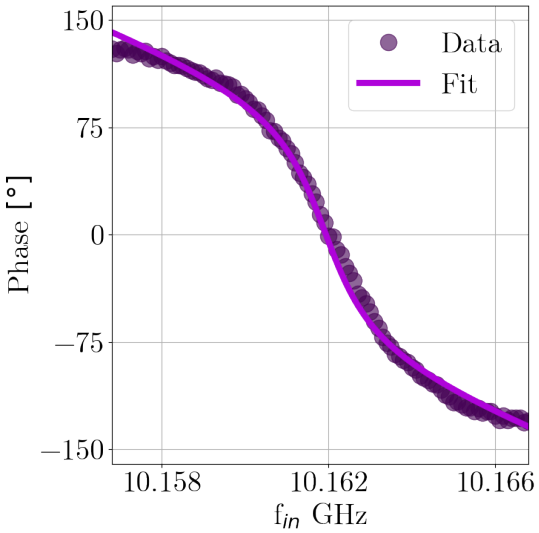

Figure 32 – VNA reflection measurement of the Bragg resonator.

The successful implementation of these Bragg resonators on silicon substrates provides the necessary filtering characteristics for qubit protection while maintaining the required transmission properties for control signal delivery. The close correspondence between simulated and experimental parameters validates our design methodology and fabrication approach, establishing a reliable platform for integration with subsequent qubit devices.

3.3 Flux Qubit Fabrication

Superconducting flux qubits constitute the central elements of this thesis work. This section details the design methodology and fabrication protocols for gradiometer flux qubits implemented on both diamond and silicon substrates.

3.3.1 Josephson Junction Fabrication

The fundamental building block for superconducting qubit devices is the Josephson junction. Our approach employs a geometric design colloquially termed the "telephone" junction, named for its distinctive layout pattern visible in Figure 31. This configuration enables the simultaneous fabrication of two junctions with independently controlled dimensions within a

single device structure. The design incorporates a primary junction characterized by width w_n and height h_n, alongside a smaller secondary junction with reduced dimensions w_α and h_α, providing the asymmetric junction ratio essential for flux qubit operation.

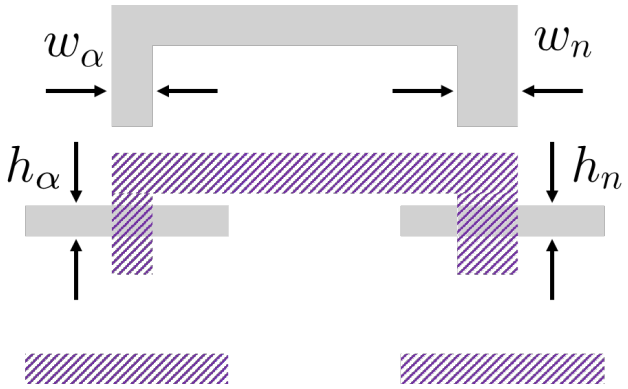

Figure 33 – Schematic layout of the "telephone" Josephson junction design | The characteristic geometry enables fabrication of asymmetric junction pairs. The design yields a primary junction (width w_n, height h_n) and a smaller α-junction (width w_α, height h_α) within a single shadow mask pattern. The telephone shape derives from the distinctive connection geometry required for independent electrical access to both junctions.

Junction fabrication relies on a bilayer aluminum structure consisting of a thin initial layer (20 nm) that undergoes controlled oxidation, followed by deposition of a thicker capping layer (30 nm). The process utilizes the established Dolan shadow evaporation technique, wherein the first aluminum layer is deposited through a suspended mask onto the bare substrate. Following in-situ oxidation to form the tunnel barrier, the second aluminum layer is deposited at a predetermined angle θ relative to the substrate normal, creating an overlap region where the two layers intersect to form the active junction area. The effective junction area follows $A = w(h + 2t)$, where t represents the thickness of the initial superconducting layer. For any given oxidation protocol, this junction area directly determines the characteristic Josephson energy E_J and charging energy E_C parameters.

The fabrication sequence begins with formation of a suspended bridge structure using a trilayer resist stack comprising high-sensitivity electron beam resist (MAA EL7), an intermediate metallic masking layer (60 nm germanium), and low-sensitivity top resist (CSAR), as illustrated in Figure 32. The complete stack undergoes electron beam exposure followed by development of the top resist layer. Reactive ion etching transfers the pattern into the germanium mask, after which a second development step and plasma ashing sequence creates the required undercut profile in the trilayer stack.

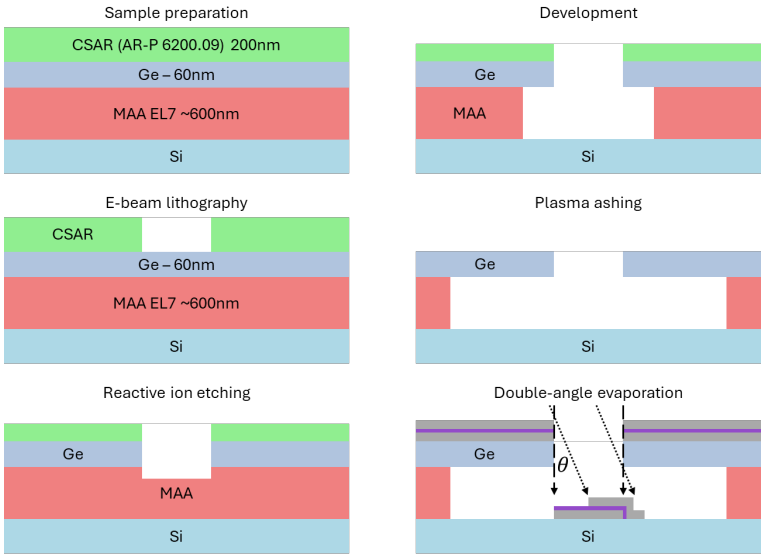

Figure 34 – Trilayer technique for double-angle shadow evaporation fabrication sequence for Josephson junctions.

The prepared sample is then loaded into an electron beam evaporator where the first aluminum layer is deposited at normal incidence while maintaining the substrate at -44°C. The suspended bridge structure casts a shadow onto the substrate, defining the junction region. Without breaking vacuum, controlled oxidation proceeds to form the insulating aluminum oxide barrier on exposed metal surfaces. The oxidation process begins at -10° C and concludes at 4° C under 0.019 mbar oxygen pressure. Subsequently, the second aluminum layer is deposited at an elevated substrate temperature of 9° C and at angle θ relative to the surface normal, creating the overlap region that constitutes the tunnel junction. Final static oxidation at 10 mbar for 10 minutes forms a protective oxide layer over the entire device structure. Following evaporation completion, the resist mask is dissolved using heated N-methyl-2-pyrrolidone (NMP). Additional e-Beam lithography process is used to define a rectangular patch that overlaps both qubit and central line of the resonator. Argon ion milling through the patch ensures good surface contact before aluminum is evaporated to create galvanic contact between the qubits and the resonator. Final cleaning is done by soaking the sample in NMP overnight. The completed device is mounted on a dedicated printed circuit board with wire-bond connections. Summary of the fabrication process steps is given in Table 9.

Table 10 – Complete fabrication protocol for Josephson junctions.

Process	Description
Tri-Layer Formation	
Spin coating	MAA EL7: 2000 rpm, 60 s; bake 180° C for 1 min
	MAA EL7: 2000 rpm, 60 s; bake 180° C for 10 min

Metal deposition	Ge layer: 60 nm at 0.3 nm s^{-1} (Plassys MEB 550S)
Spin coating	CSAR (AR-P 6200.09): 4500 rpm, 60 s; bake 100° C, 5 min
Junctions Formation	
E-beam lithography	Elionix ELS Boden 100: dose = 1300 $\mu C\ cm^{-2}$, I = 1 nA
Development	MIBK:IPA (1:3), 5 min
Metal Etching	RIE: SF_6 20 sccm, P_{rf} = 20 W, laser interferometer calibration (Versaline SLR 770)
Development	MIBK:IPA (1:3), 90 s
Plasma ashing	O_2+N_2, 3.5 min
Metal deposition	First Al layer: 20 nm of Al at 0.3 nm s^{-1}, T = -44° C, θ=0°
	Dynamic oxidation: T_{start} = −10° C, T_{end} = 4° C, P = 0.019 mbar
	Second Al layer: 30 nm of Al at 0.3 nm s^{-1}, T = 9° C, $\theta \neq 0°$
	Static oxidation: 10 min, P = 10 mbar
Cleaning	
Solvents cleaning	NMP: 80° C, Overnight
Re-contact	
Spin coating	MAA EL7: 2000 rpm, 60 s; bake 120° C for 4 min
	PMMA 950A3: 6000 rpm, 60 s; bake 120° C for 4 min
E-beam lithography	Elionix ELS Boden 100: dose = 1000 $\mu C\ cm^{-2}$, I = 10 nA
Development	MIBK:IPA (1:3), 1 min
Ion-milling	Plassys MEB 550S: P<10^{-6} mbar, Ar 20 sccm, 500 V, 17.5 mA
Metal deposition	Plassys MEB 550S: Al 170 nm, 0.5 nm s^{-1}
Cleaning	
Solvents cleaning	NMP: 80° C, Overnight

3.3.2 Josephson Junctions Characterization

Junction characterization required dedicated test structures featuring junctions of varying dimensions. Normal-state resistance measurements using four-probe techniques enabled extraction of the resistance-area product, providing the design parameter necessary for achieving specific normal resistance values. Through the Ambegaokar-Baratoff relationship detailed in the methodology chapter, normal resistance directly correlates with critical current, enabling precise control of qubit parameters through accurate junction dimension control.

Test structures were implemented on both substrate types to establish fabrication parameters. The diamond test array contained six distinct junction geometries with twenty repetitions of each design distributed across the chip area to average spatial fabrication variations. Each site contained a single junction element, yielding 120 total junctions per chip. Figure 33 presents the measured resistance plotted against inverse junction area, demonstrating the expected linear relationship.

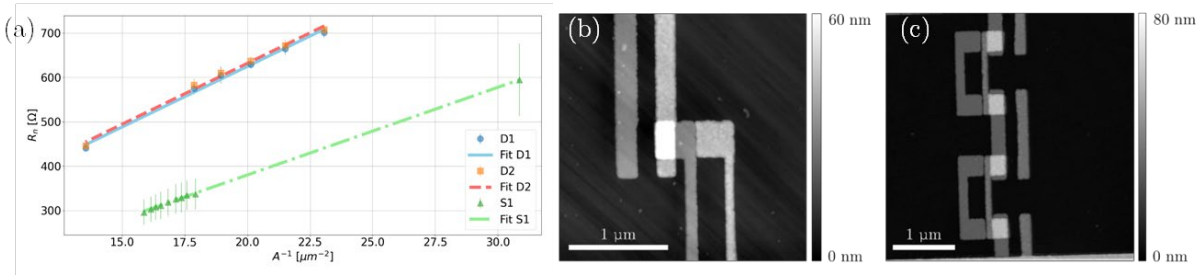

Figure 35 – Josephson junction characterization and substrate comparison | (a) Normal-state resistance versus inverse junction area demonstrating the predicted linear relationship. Dataset D1 (diamond, immediate): $R_n^{A,D} = 27.21 \pm 0.58$ Ω·µm², Dataset D2 (diamond, 24-day aging): $R_n^{A,D} = 27.52 \pm 0.58$ Ω·µm², Dataset S1 (silicon, immediate): $R_n^{A,Si} = 19.77 \pm 0.12$ Ω·µm². AFM topography of completed junctions on (b) diamond and (c) silicon substrates.

Initial measurements immediately following fabrication yielded $R_n^{A,D} = 27.21 \pm 0.58$ Ω·µm² for diamond substrates. To assess temporal stability, devices were stored under ambient laboratory conditions and re-measured after 24 days, producing $R_n^{A,D} = 27.52 \pm 0.58$ Ω·µm². While individual junction resistances increased by approximately 9 Ω, the resistance-area product remained essentially constant, confirming minimal aging effects on junction properties.

Silicon test arrays employed a similar characterization approach with ten junction variants and twenty repetitions per design. Each test site incorporated four individual junctions, resulting in 80 junctions per geometry and 800 total junctions across the full array. Immediate post-fabrication measurements yielded $R_n^{A,Si} = 19.77 \pm 0.12$ Ω·µm² for silicon substrates.

3.3.3 Gradiometer Flux Qubit Fabrication

The gradiometer flux qubit design employed in this work appears in Figure 36. The gradiometer geometry is characterized by its height h and length l parameters, which together determine the total loop area A. The length of each gradiometer arm, measured at the center of the 600 nm wide metal strip, follows $L = h + l - 2w$. The loop area governs the magnetic flux threading the gradiometer structure, while the arm length affects qubit-resonator coupling through its associated inductance.

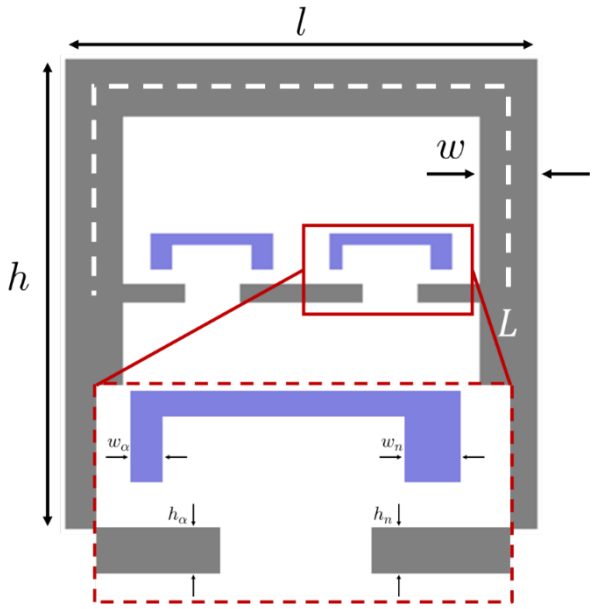

Figure 36 – Gradiometer flux qubit geometry and design parameters | The symmetric gradiometer loop is characterized by height h and length l, yielding total area $A = h \times l$ and arm length $L = h + l - 2w$ (measured at center of strip width w). Inset shows detailed view of asymmetric Josephson junction pair with normal junction (w_n, h_n) and α-junction (w_α, h_α).

To enable identification of individual devices, eleven distinct qubits were designed with parameters summarized in Table 10. x_{qb} represents the position of the qubit along the transmission line of the resonator with respect to the end of the Bragg filter.

Table 11 – Gradiometer flux qubit design matrix.

Parameter	Q_1	Q_2	Q_3	Q_4	Q_5	Q_6	Q_7	Q_8	Q_9	Q_{10}	Q_{11}
$\boldsymbol{h}$ [µm]	5.00	5.15	5.30	5.45	5.60	5.75	5.90	6.05	6.20	6.35	6.50
$\boldsymbol{L}$ [µm]	8.80	8.95	9.10	9.25	9.40	9.55	9.70	9.85	10.00	10.15	10.30
$\boldsymbol{A}$ [µm^2]	19.36	20.02	20.68	21.34	22.00	22.66	23.32	23.98	24.64	25.30	25.96
$\boldsymbol{x_{qb}}$ [µm]	955	1305	1655	2005	2355	2705	3055	3405	3755	4105	4455

The Josephson junction elements within each qubit are characterized by their geometric parameters. Both normal and α junction heights were fixed at $h_n = h_\alpha = 180$ nm, with widths designed as $w_n = 245$ nm and $w_\alpha = 125$ nm.

To assess the fabricated Josephson junctions the experimental chip 28 test structures arranged with four Josephson junctions per array, comprising 18 structures featuring normal junctions and 10 incorporating α junctions.

Room-temperature resistance measurements result with normal resistances of $R_n^N = 710 \pm 38\ \Omega$ for standard junctions and $R_n^\alpha = 1235 \pm 99\ \Omega$ for α junctions, corresponding to $E_J = 201 \pm 11$ GHz and $\alpha = 0.57 \pm 0.06$.

The geometric capacitance of the junctions was simulated using COMSOL Electrostatics (see Figure 37a), following the rational developed in reference 118. The result geometric capacitance is given by Equation 34 with $C_{12} = 0.28216$ fF, $C_{13} = 0.22577$ fF, $C_{14} = 0.27159$ fF, $C_{23} = -0.05037$ fF, $C_{24} = -0.00189$ fF, $C_{34} = -0.05687$ fF.

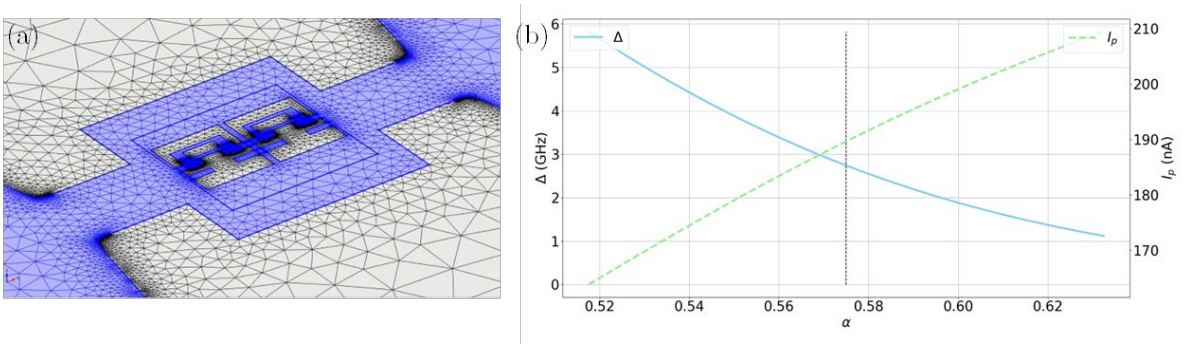

Figure 37 – Simulations of the gradiometer flux qubit | (a) COMSOL model of the gradiometer qubit used to evaluate its geometric capacitance. (b) Energy gap and persistence current from the solution of the full Hamiltonian of the gradiometer flux qubit with $E_J = 201$ GHz and $E_J/E_C \approx 53$ GHz. For the target parameter $\alpha = 0.575$, the energy gap is $\Delta = 2.74$ GHz and the persistent current is $I_p = 190$ nA.

With all design parameters in hand, we numerically solved the full Hamiltonian to extract the energy splitting of the qubit and its persistence current, as shown in Figure 37b. For our design parameters, $E_J = 201$ GHz and $E_J/E_C \approx 53$ GHz, we expect to get $\Delta = 2.74$ GHz and $I_p = 190$ nA.

Figure 38 shows the coupling between the Bragg resonator and the qubit as well as the Purcell decay rate where calculated based on the design parameters and positions x_{qb} of the qubits along the transmission line part of the Bragg resonator that are given in Table 10. Coupling strength is on the range of 30 MHz to 80 GHz while according to Equation 74 the expected Purcell decay rate is on the range of 60-190 kHz.

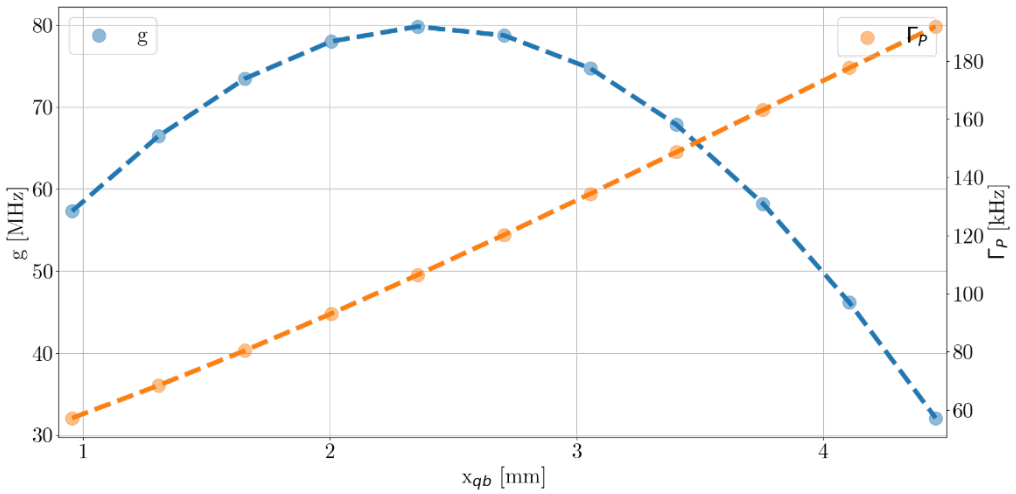

Figure 38 – Simulated coupling strength g and Purcell decay rate Γ_P.

The double-angle evaporation process inherently creates two superconducting loops within the completed device structure, as shown in Figure 39. To prevent unwanted flux trapping in the parasitic loop formed during second-layer deposition, this redundant circuit element must be electrically isolated. This isolation is accomplished through focused ion beam milling to sever the unwanted loop while preserving the primary gradiometer circuit.

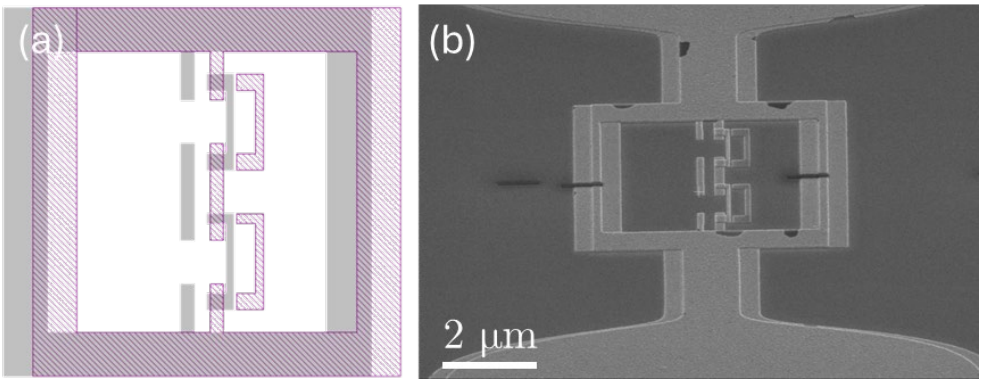

Figure 39 – Completed gradiometer flux qubit structure and parasitic loop removal | (a) Schematic overlay showing first aluminum layer pattern (purple stripes) and second aluminum layer (gray solid) illustrating the double-angle evaporation result. The overlap regions form the active Josephson junctions while creating an unwanted parasitic loop. (b) Tilted SEM image (30° tilt) of finished device after focused ion beam cutting to eliminate the redundant superconducting loop, preventing flux trapping while preserving the primary gradiometer circuit.

4. Experimental System

This chapter presents comprehensive details of the measurement infrastructure employed for characterizing superconducting resonators and flux qubits. The experimental configurations are tailored to accommodate two distinct measurement scenarios: coplanar waveguide

resonator characterization and integrated flux qubit systems incorporating Bragg resonator. Additionally, we describe the implementation and optimization of a traveling wave parametric amplifier (TWPA) readout application.

4.1 Coplanar Waveguide Resonator Characterization Setup

Sample mounting for coplanar waveguide (CPW) resonator measurements utilize PMMA adhesive to secure devices onto microwave-compatible printed circuit boards (PCBs) made from TMM10 ceramics. These boards incorporate precision-etched 50 Ω coplanar waveguide transmission lines that route signals from the device location to SMP connectors, enabling connection to external coaxial infrastructure. Electrical continuity between the sample and board is established through wire bonding, providing zero-resistance pathways for both signal and ground connections.

The complete assembly is housed within a gold-plated copper enclosure engineered for minimal electromagnetic mode volume, thereby reducing parasitic coupling and improving measurement sensitivity. This packaged system operates within a Cryoconcept Hexadry 200 dilution refrigerator featuring low mechanical vibration characteristics. Thermal anchoring to the mixing chamber achieves base temperatures of 15 mK, essential for accessing the quantum regime of superconducting devices.

Microwave characterization employs a Keysight PNA-L N5235 vector network analyzer (VNA) as the primary measurement instrument. Signal routing from room temperature to the cryogenic environment begins with TestPro 4.5 cables connecting the VNA output to copper-nickel composite cables within the refrigerator. These CuNi cables provide the necessary balance between thermal isolation and electrical conductivity while routing signals from ambient temperature to the 4 K thermal stage.

At the intermediate temperature stage, microwave signals undergo controlled attenuation through an XMA -20 dB attenuator before transition to superconducting NbTi coaxial cables for the final connection to the mixing chamber stage. Additional signal conditioning at the base temperature stage incorporates XMA attenuators providing attenuation from -10 dB to -40 dB, depending on the specific experiment.

The signal detection pathway incorporates a shielded double-circulator (QCY-060400CM20, QuinStar Tech.) positioned at the mixing chamber stage to enforce unidirectional signal-flow and minimize reflections. Signal amplification occurs in multiple stages, beginning with a low-noise cryogenic HEMT amplifier (LNF-LNC4_8C) at the 4 K stage, followed by additional room-temperature amplification using a second HEMT amplifier (LNF-LNR1_15A). The conditioned signal returns to the VNA input port for digital processing and analysis. The complete measurement architecture is illustrated in Figure 40, showing the temperature-staged signal routing and conditioning elements.

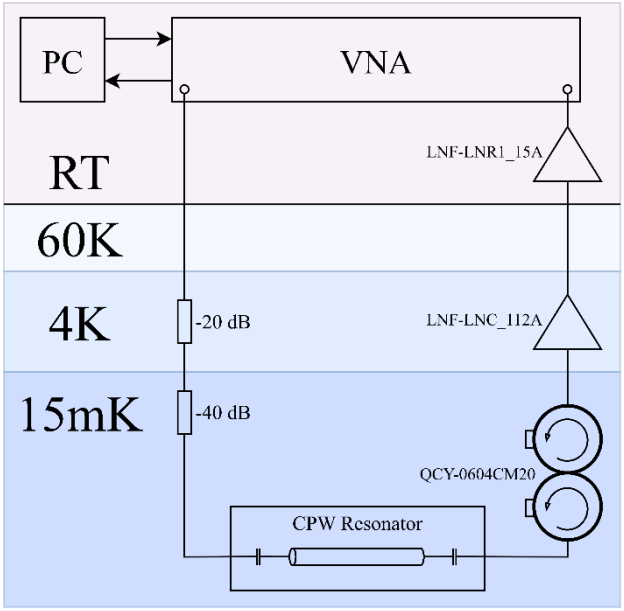

Figure 40 – Measurement infrastructure for CPW resonator characterization | The schematic shows signal routing from room temperature VNA through temperature-staged attenuation and amplification within a dilution refrigerator. Key components include CuNi thermal isolation cables (RT to 4K), superconducting NbTi cables (4K to 15mK), staged HEMT amplification (LNF-LNC4_8C at 4K, LNF-LNR1_15A at RT), and shielded circulators for signal isolation. The CPW resonator sample is housed in a gold-plated copper enclosure thermally anchored to the 15 mK mixing chamber stage.

4.2 Bragg Resonator and Flux Qubit Measurement Configuration

Silicon substrates containing integrated Bragg resonators and gradiometer flux qubits require a more sophisticated experimental arrangement to accommodate both microwave characterization and magnetic flux control. Sample mounting follows similar protocols as described for CPW resonators, utilizing identical PCB technology and wire bonding techniques for device connectivity.

The critical enhancement for flux qubit experiments involves implementation of a custom superconducting magnetic coil system. This coil features a gold-plated copper bobbin wound with 387 meters of NbTi wire embedded in a CuNi stabilizing matrix. The total wire diameter was 0.152 mm. Room temperature coil resistance measures 10.38 kΩ, yielding a current-to-magnetic-field conversion efficiency of 0.3788 G/mA at the sample location.

The coil assembly accommodates multiple sample orientations, enabling magnetic field application either parallel or perpendicular to the substrate surface, as demonstrated in Figure 41. This flexibility proves essential for investigating different coupling mechanisms between external fields and the gradiometer loop structures.

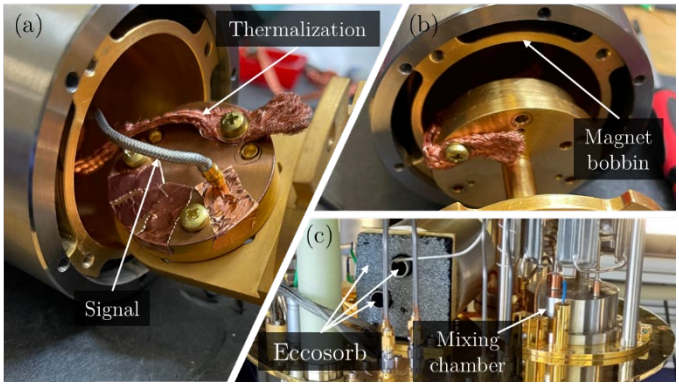

Figure 41 – Custom superconducting magnetic coil system for flux qubit bias control | Flexible sample mounting enables magnetic field orientation parallel (a) or perpendicular (b) to substrate surface, essential for investigating different gradiometer coupling mechanisms. The coil features gold-plated copper bobbin with NbTi-in-CuNi wire. (c) Multi-layer magnetic shielding combines superconducting Ti-64 alloy inner shield with high-permeability CryoPhy outer housing. Eccosorb AN-72 absorbing material seals cable penetrations to prevent electromagnetic leakage while maintaining thermal anchoring to the mixing chamber base temperature.

Magnetic noise suppression employs a multi-layer shielding approach incorporating both superconducting and high-permeability materials. The primary shield consists of a superconducting titanium alloy (Ti-64[130]) enclosure that eliminates low-frequency magnetic fluctuations through flux expulsion. Secondary shielding utilizes high-permeability CryoPhy material (Meca Magnetic) to attenuate residual magnetic noise at higher frequencies. Electromagnetic radiation suppression is achieved through strategic placement of Eccosorb AN-72 absorbing material at potential leakage points.

Current sourcing for magnetic bias control utilizes a BILT BE-2102 precision voltage source coupled to a custom voltage-to-current converter. This converter incorporates a series-

connected capacitor and 1 kΩ precision resistor maintained at constant temperature (37°C) to minimize resistance drift and ensure stable current conversion. Temperature regulation proves critical for maintaining current stability over extended measurement periods.

The DC signal for sample biasing is applied by additional BILT source. The signal goes through multiple filtering stages to achieve the noise levels required for coherent qubit operation. Initial filtering employs an inductive low-pass filter (R = 142 Ω, L = 16 H) at room temperature followed by a Mini-Circuits VLFX 1050 low-pass filter and an XMA -20 dB attenuation at the 4 K stage. Further noise reduction at the mixing chamber stage utilizes a cascaded filter chain including a custom Eccosorb filter (approximately -6 dB/GHz[131]), and a MiniCircuit SLP-1.9+ commercial filter.

For practical implementation, the DC bias current I_{DC} is applied through a T-type attenuator circuit (see Figure 42) to provide impedance matching and signal isolation.

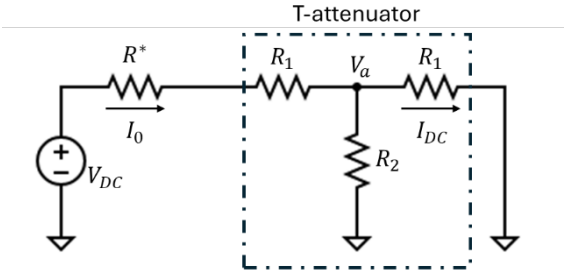

Figure 42 – Circuit diagram of a T-attenuator

The effective resistance R relating the applied voltage V_{DC} to the bias current I_{DC} is:

$$R = \frac{R^*R_1 + R^*R_2 + R_1^2 + 2R_1R_2}{R_2} \tag{100}$$

where R^* is the residual resistance of connecting wires, and $R_1 = R_0\frac{N-1}{N+1}$, $R_2 = \frac{R_0^2-R_1^2}{2R_1}$ are the attenuator resistors. The attenuator parameters are designed to match the system impedance R_0 and provide attenuation factor $N = 10^{\frac{dB}{20}}$. This configuration enables precise control of the qubit operating point while maintaining proper impedance matching for microwave signals.

Microwave signal generation employs dual-source architecture optimized for independent resonator and qubit control. Resonator driving signals originate from a Keysight E8257 analog signal generator, while qubit manipulation employs an R&S SMA100B RF generator. Pulse modulation occurs at intermediate frequencies spanning 10-200 MHz using a Quantum

Machines OPX+ control system connected to MITEQ IRM0618/IRM0408 frequency mixers. Fine amplitude control utilizes a Pulsar AAR-29-479 voltage-controlled attenuator providing continuous adjustment across 0.5-64 dB range.

Signal combination prior to refrigerator entry employs a Pulsar PS2-18-450/9S two-way power divider, enabling simultaneous resonator and qubit addressing. Thermal noise minimization incorporates staged attenuation with XMA -20 dB attenuation at 4 K and XMA -30 dB attenuation at the mixing chamber stage. Additional filtering utilizes a custom[131] impedance-matched copper powder filter providing -10 dB attenuation at 10 GHz. A shielded circulator (QCY_0812, QuinStar Tech.) eliminates reflected signal leakage.

DC and microwave signals are combined at the mixing chamber stage through a Marki BT-0018 bias-T and undergo final filtering through a -3 dB IR filter before sample connection. This configuration enables simultaneous flux biasing and microwave control of the qubit system.

Readout signal processing employs reflection measurements from the Bragg resonator with extensive filtering prior to parametric amplification. The signal processing chain includes a 3 dB IR filter, shielded double circulator (QCY_0812), 8-12 GHz bandpass filter (MicroTronics BPC50406), and DC blocking capacitor. Following TWPA amplification, additional signal conditioning includes circulator isolation and cryogenic HEMT amplification (LNF-LNC1_12A). Room temperature processing incorporates secondary HEMT amplification (LNF-LNR_15A), signal demodulation, and voltage amplification using a Femto HVA-500M-20-B amplifier. Final signal acquisition utilizes the analog inputs of the OPX+ control system. The complete experimental configuration is detailed in Figure 43, illustrating the integration of all signal generation, conditioning, and detection components.

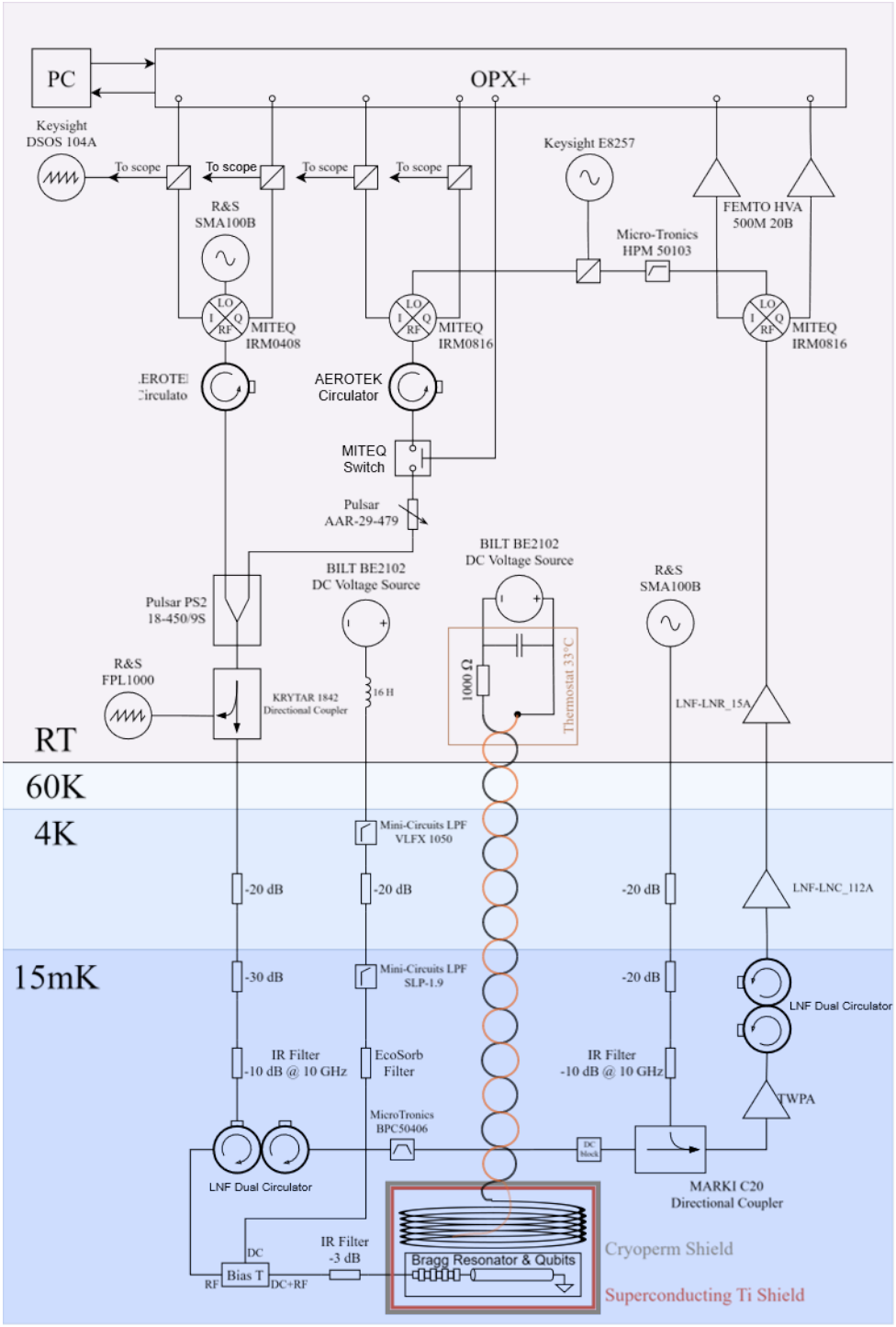

Figure 43 – Experimental configuration for flux qubit characterization with Bragg resonator readout | The system integrates dual-source microwave generation, Quantum Machines OPX+ pulse control, staged cryogenic filtering and attenuation, custom magnetic coil with multi-layer shielding, and traveling wave parametric amplifier. Signal processing includes temperature-staged amplification, extensive filtering chains, and real-time demodulation. The modular design enables simultaneous flux biasing, microwave control, and high-fidelity readout of superconducting flux qubits.

4.3 Traveling Wave Parametric Amplifier Implementation

The reversed Kerr traveling wave parametric amplifier (RKerr-TWPA) used in this work was developed by the research team led by Dr. Nicolas Roch at the Néel Institute in Grenoble. The amplifier is integrated directly into the readout signal path at the mixing chamber base temperature, positioned between the sample filtering chain and the cryogenic HEMT amplifier stage. This placement ensures that the weak reflected signals from the Bragg resonator receive immediate low-noise amplification before encountering additional circuit elements that could degrade the signal-to-noise ratio.

The TWPA requires independent pump signal generation and DC bias control for optimal operation. The pump line utilizes an additional R&S SMA100B signal generator with dedicated signal conditioning including XMA -20 dB attenuators at both 4 K and mixing chamber stages, followed by custom copper powder filtering to minimize noise coupling into the amplification process. DC biasing of the TWPA employs a separate BILT source with precise voltage control to maintain the optimal flux operating point.

TWPA characterization begins with VNA transmission measurements in the absence of a pump. These measurements reveal spurious mode oscillations that vary with applied magnetic flux, as presented in Figure 44a. The optimal operating point for reversed Kerr amplification occurs at the 'half-flux' condition corresponding to minimized spurious mode amplitude. Based on these measurements, we selected $V_{DC} = 0.08$ V as the optimal flux bias point for subsequent operation.

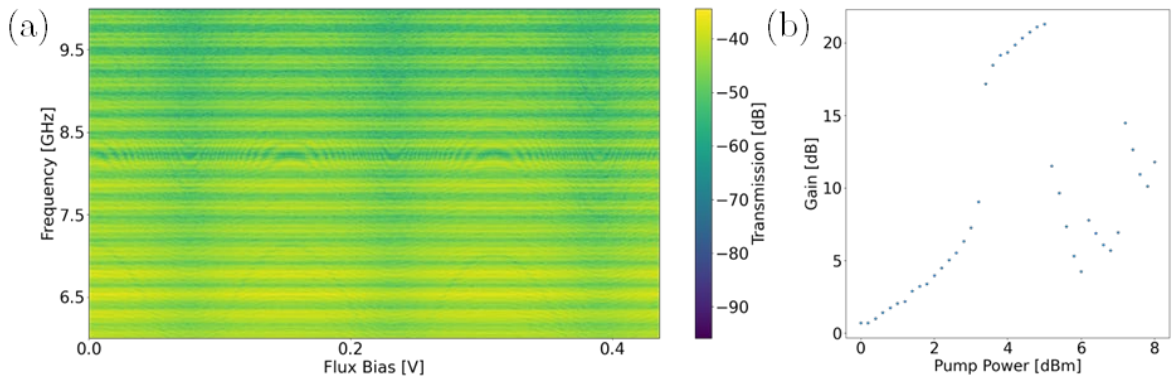

Figure 44 – TWPA characterization and optimization | (a) VNA transmission mapping versus frequency and flux bias showing spurious mode oscillations that determine optimal operating conditions. The 'half-flux' point at $V_{DC} = 0.08$ V corresponds to minimum spurious mode amplitude, providing optimal phase-matching conditions for reversed Kerr amplification. (b)

Parametric gain optimization showing peak gain of 21 dB achieved at pump frequency $f_{pump} = 8.174$ GHz and pump power 5 dBm.

Parametric gain optimization requires systematic characterization of both pump power and frequency to identify conditions yielding maximum signal amplification. The measurement protocol involves VNA transmission measurements using narrow-bandwidth drive signals (10.19 GHz ± 5 MHz) while varying pump parameters. Gain calculation compares average transmitted power with and without pump activation. This optimization procedure identified optimal conditions of $f_{pump} = 8.174$ GHz and 5 dBm pump power, yielding peak gain of 21 dB, as shown in Figure 44b.

5. Results and Discussion

This chapter presents experimental characterization of gradiometer superconducting flux qubits (GFQs) coupled to Bragg resonators on a high resistivity silicon substrate. Detailed device design and fabrication are given in section 3.2.2. The GFQ consists of a figure-eight superconducting loop intersected by three or four Josephson junctions, where the two sub-loops form a gradiometer configuration that cancels homogeneous magnetic field dependence.

Early implementations demonstrated significant capabilities but with notable limitations. The first tunable-gap GFQ achieved gap control up to 12 GHz through tunable α-junctions, though coherence times remained very short[94]. Strong coupling between a tunable GFQ and microwave resonator was subsequently demonstrated, but coherence was still limited to $T_1 = 1.5$ μs and $T_2 = 300$ ns[95]. GFQs also enabled studies of the quantum-to-classical transition in macroscopic systems[96] and investigations of kinetic inductance effects on qubit performance[97].

In this work, we eliminate the need for dedicated flux lines by implementing a Bragg-filter terminated coplanar waveguide resonator. The Bragg filter termination enables DC current application through the resonator's center conductor while simultaneously providing noise suppression through high-frequency signal filtering. Each qubit has a different loop area (see Table 10), thus their anticrossing appears at different values of the bias current. To maximize qubit-resonator coupling strength, the GFQ is galvanically connected directly to the resonator.

We demonstrate quantum coherent operation through spectroscopic analysis, coherence time measurements ($\Gamma_1 = 33$ kHz, $\Gamma_{2,E} = 80$ kHz), and randomized benchmarking protocols ($r_g = 9 \times 10^{-3}$).

5.1 Bragg Resonator Integration and Performance

Figure 45a presents the Bragg resonator device fabricated on a silicon substrate using a 150 nm aluminum superconducting layer, following the fabrication protocols detailed previously. The device features a Bragg filter architecture consisting of $m = 4$ doublets with alternating impedances of $Z_1 = 35\ \Omega$ and $Z_2 = 80\ \Omega$, where each impedance segment has a length of $L_B = 3.44$ mm. This Bragg filter configuration achieves near-perfect reflection with $|r_B|^2 \approx 99\%$ at the stopband center frequency of 8.58 GHz. Beyond the Bragg filter, an 8.044 mm coplanar transmission line accommodates eleven gradiometer flux qubits, which are galvanically connected to the central line, before terminating in a short circuit to ground, with both microwave and DC signals transmitted through the Bragg filter via a single port. Figure 45 displays scanning electron microscopy image of qubit A, showing the completed gradiometer structure after removal of the redundant loop using focused ion beam processing. Comprehensive details regarding sample design and fabrication procedures are provided in Chapter 3.

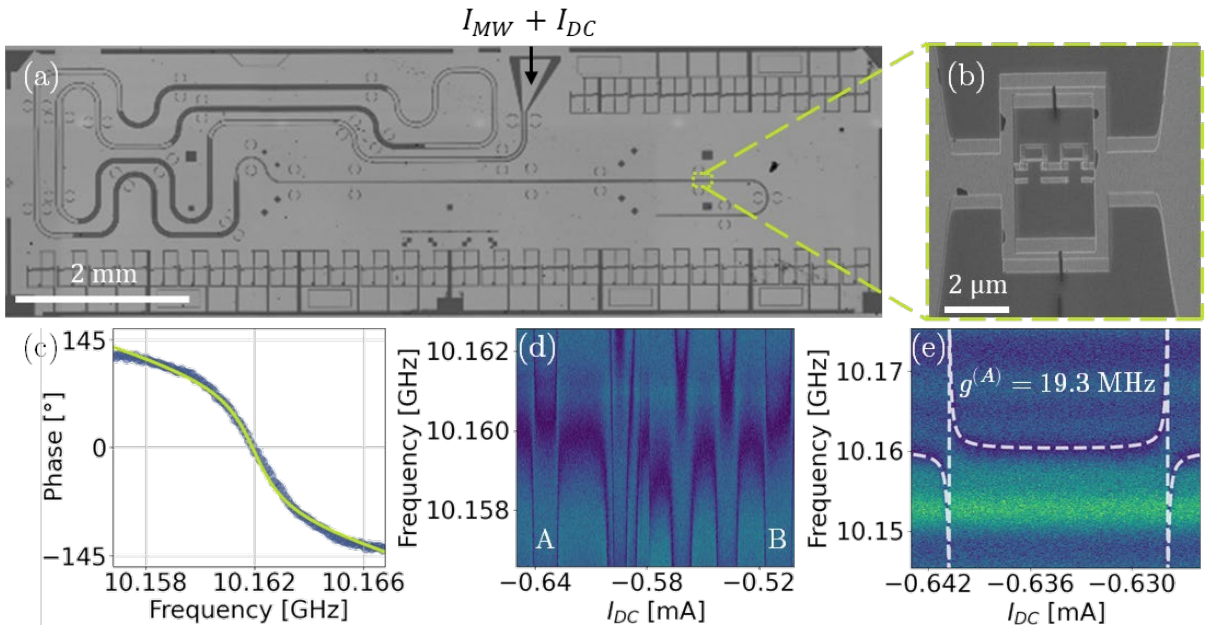

Figure 45 – Circuit implementation | (a) Optical microscopy image of complete device showing quarter-wave Bragg resonator. Eleven GFQs are integrated along the transmission line section. (b) Scanning electron micrograph of qubit A after the focused ion beam cut the parasitic superconducting loop. (c) Vector network analyzer reflection measurement demonstrating

resonator performance with measured frequency $\frac{\omega_r}{2\pi} = 10.162$ GHz, decay rate $\kappa_C = 6$ MHz, and quality factor $Q_C \approx 10^4$, confirming integration without significant loss mechanisms. (d) Resonator spectroscopy versus I_{DC} revealing distinct anticrossing patterns of six qubits and two overlapping signatures, validating flux control through transmission line current injection. (e) Detailed anticrossing analysis for qubit A yielding coupling strength $g^{(A)} = 19.3$ MHz through model fitting.

The experimental system employs dedicated microwave sources to generate local oscillator signals for resonator and qubit control, which are mixed with intermediate frequency pulses from an OPX+ system before being combined and transmitted to the sample housed within a Cryoconcept dilution refrigerator operating at a base temperature of 15 mK. The outgoing signals undergo attenuation and filtering along the transmission path to the sample, while the reflected signals from the sample are amplified through a multi-stage amplification chain consisting of a reversed Kerr traveling wave parametric amplifier (RKerr-TWPA) providing ~21 dB gain positioned at the mixing chamber stage, followed by high electron mobility transistor amplifiers located at 4 K and room temperature. The amplified signals are subsequently demodulated and measured using the OPX+ system at room temperature, with comprehensive details of the experimental setup provided in Chapter 4.

Figure 45c shows vector network analyzer reflection measurements used to characterize the resonator response. The measured resonance frequency of was $\frac{\omega_r}{2\pi} = 10.162$ GHz required correction of our estimated substrate permittivity to $\epsilon_r^{Si} = 11.896$, corresponding to an in-resonator light velocity of $c = 118{,}060{,}115$ m·s^{-1}. The experimental decay rate $\kappa_C = 6$ MHz produced a quality factor $Q_C \approx 10^4$, demonstrating good correspondence with theoretical predictions established in previous chapters.

DC current bias measurements revealed the anticipated anticrossing behavior characteristic of strong qubit-resonator coupling, as demonstrated in Figure 45d. Systematic investigation identified responses from eight of the eleven integrated qubits. Six devices exhibited distinct magnetic flux responses while two displayed overlapping characteristics. This outcome validates our approach using current injection through the Bragg filter and into the resonator transmission line to magnetically bias the qubits.

Of the three unobserved qubits, one sustained damage during the focused ion beam procedure, while the remaining two are believed to operate far detuned from the resonator frequency, rendering them undetectable within our measurement bandwidth. We analyzed the relationship between the design sizes of the qubit loops and the positions of the optimal

flux bias points to assign each pattern to a specific qubit. We found that the qubits appearing in Figure 45d correspond to the designed positions 3 (qubit A) and 8 (qubit B).

Detailed analysis concentrated on qubits A and B, which demonstrated clear anticrossing signatures suitable for quantitative characterization. Figure 45e presents the anticrossing pattern for qubit A, from which we extracted coupling strength $g^{(A)} = 19.3$ MHz through fitting to the established resonator-qubit interaction model. Similar analysis of qubit B yielded coupling strength $g^{(B)} = 21.5$ MHz, indicating comparable interaction strengths across different device positions within the resonator.

5.2 Spectroscopic Characterization and Qubit Parameters

Comprehensive qubit characterization required spectroscopic measurements under variable magnetic bias conditions. The qubit transition frequency follows $\frac{\omega_{qb}}{2\pi} = \sqrt{\Delta^2 + \epsilon^2}$, where $\epsilon = \frac{2I_p}{\hbar}\left(\Phi - \frac{\Phi_0}{2}\right)$, represents the energy offset from the optimal flux point. Here, $\Phi = \frac{\Phi_d}{2}$ with Φ_d the flux difference between the two loops of the GFQ. This relationship enables extraction of the fundamental qubit parameters: energy splitting Δ and persistent current I_p.

Experimental results shown in Figure 46a and b yielded $\Delta^{(A)} = 9.097$ GHz with $I_p^{(A)} = 138$ nA, and $\Delta^{(B)} = 7.226$ GHz with $I_p^{(B)} = 147$ nA. These parameters correspond to Josephson energies $E_J^{(A)} = 194$ GHz and $E_J^{(B)} = 191$ GHz, with asymmetry ratios $\alpha^{(A)} = 0.475$ and $\alpha^{(B)} = 0.499$. The Josephson energy is in good agreement with the expected values from room temperature characterization of the test junctions while the reduced values of α reflect dimensional variations in junction fabrication.

The voltage-to-flux conversions were calibrated through measurements at the optimal flux point $\Phi = \Phi_0/2$. Knowledge of the applied DC voltage at operation V_{DC}^{opt} allowed conversion of arbitrary voltages V_{DC} to magnetic flux using $\Phi = V_{DC}/2V_{DC}^{opt}$ $[\Phi_0]$. We used the relationship given in Equation 40 to calculate the mutual inductance of the qubits per gradiometer loop length $M = 1.00 \pm 0.06$ pH/μm.

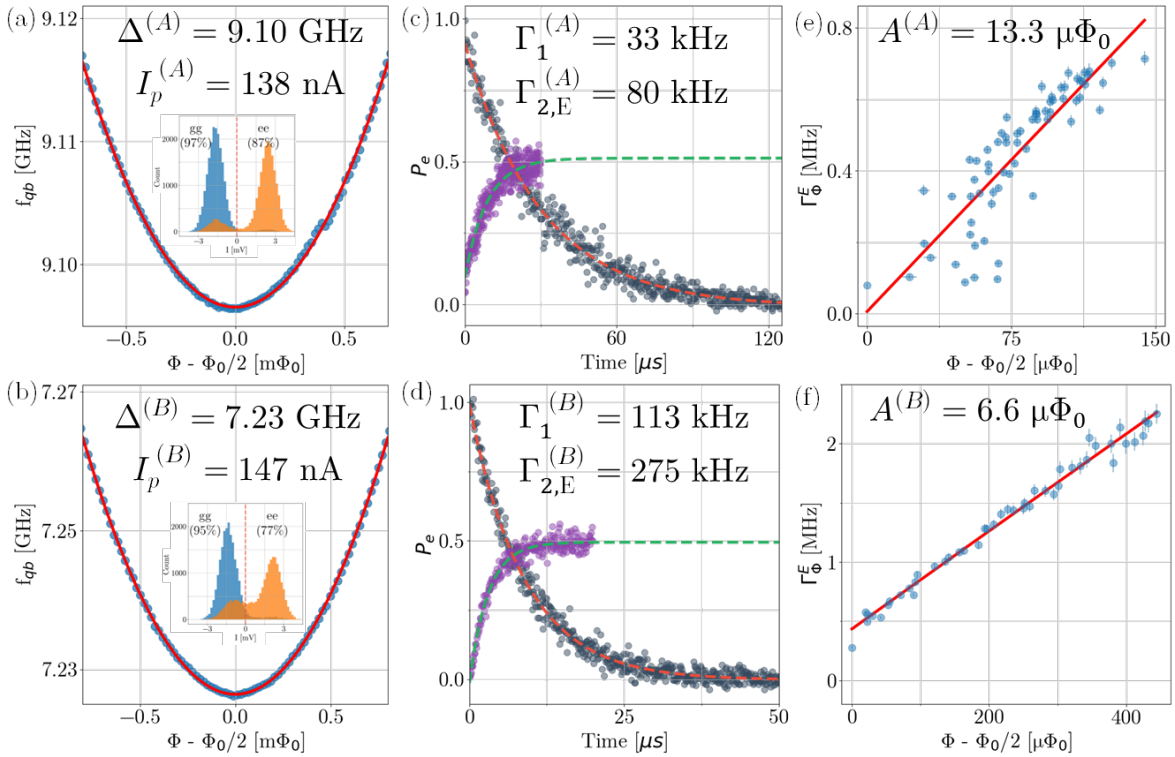

Figure 46 – Comprehensive flux qubit characterization and coherence measurements | (a,b) Spectroscopic determination of qubit parameters showing energy splitting Δ and persistent current I_p for qubit A ($\Delta^{(a)} = 9.097$ GHz, $I_p^{(A)} = 138$ nA) and qubit B ($\Delta^{(B)} = 7.226$ GHz, $I_p^{(B)} = 147$ nA), with theoretical fits confirming gradiometer flux response. (c,d) Coherence time measurements reveal relaxation rate Γ_1 (33 kHz for qubit A, 113 kHz for qubit B) and decoherence rate $\Gamma_{2,E}$ (80 kHz for qubit A, 275 kHz for qubit B) through standard decay and Hahn-Echo protocols respectively. (e,f) Flux noise amplitude extraction from coherence data yielding $A^{(A)} = 13.3\ \mu\Phi_0$ and $A^{(B)} = 6.6\ \mu\Phi_0$.

On the basis of the spectroscopic parameters, we implemented coherent qubit control using tailored microwave pulses. Continuous wave pulses employed tapered-cosine window envelopes to minimize spectral leakage, with pulse durations of 100 ns for qubit A and 16 ns for qubit B, both incorporating 8 ns rise/fall times. Rabi-like calibration procedures determined π-pulse amplitudes by measuring qubit state populations versus drive strength. Half-amplitude pulses generated the required $\pi/2$ rotations for coherence measurements. Frequency and power correction based on the ALLXY method[132] were implemented to increase the fidelity of the gate.

Readout fidelity optimization involved comparing resonator responses between qubit ground states (following extended relaxation periods, $t_{wait} > 5T_1$) and excited states (immediately after π-pulse application). This process generated distinct populations in the resonator's I-Q measurement plane, which were aligned along the I-axis through coordinate rotation. Optimal state discrimination thresholds yielded ground-state fidelities of $f_{gg} = 97\%$ for qubit A and

95% for qubit B. Excited-state fidelities reached $f_{ee} = 87\%$ for qubit A and 77% for qubit B. The origin of the low excited-state fidelity remains unclear, as while readout errors and pulse control issues contribute to the reduced fidelity, they cannot fully account for the observed degradation—the high ground-state measurement fidelity indicates minimal readout error contribution, and randomized benchmarking experiments (described in a subsequent section) show that pulse control errors alone are insufficient to explain the magnitude of the fidelity loss.

In subsequent measurements we used the readout fidelity matrix $R = \begin{bmatrix} f_{ee} & f_{eg} \\ f_{ge} & f_{gg} \end{bmatrix}$, where f_{ij} represents the probability of measuring state j when the qubit was prepared in state i, to improve results visibility. Each measurement yielded probability vectors $P = (p_e, p_g)$, which were corrected through $P_c = PR^{-1}$ to account for finite readout fidelity.

Relaxation time characterization employed standard energy decay measurements, initializing qubits in excited states through π-pulse application and monitoring population decay over variable delay periods. The measured relaxation rates were $\Gamma_1^{(A)} = 33.1 \pm 0.55$ kHz and $\Gamma_1^{(B)} = 113 \pm 1.4$ kHz, as presented in Figure 46c and d respectively. To validate we are not limited by the Purcell decay, we calculated the decay rate using Equation 74. We found $\Gamma_P^{(A)} = 2.109$ kHz, and $\Gamma_P^{(B)} = 0.105$ kHz, assuming $T = 20$ mK. Thus, we can conclude the Purcell effect does not limit the decay rate of the qubits.

Dephasing time measurements utilize Hahn-Echo sequences. The protocol involved ground state initialization, $\pi/2$-pulse application, free evolution for time t/2, π-pulse refocusing, additional free evolution for time t/2, and final $\pi/2$-pulse readout. This approach yielded echo coherence rates $\Gamma_{2,E}^{(A)} = 80 \pm 5$ kHz and $\Gamma_{2,E}^{(B)} = 275 \pm 9$ kHz, demonstrated in Figure 46c and d. Consequently, the pure dephasing rates $\Gamma_\phi^{(A)} = 63 \pm 5$ kHz and $\Gamma_\phi^{(B)} = 219 \pm 9$.

Following established theoretical frameworks detailed in the Flux Qubit Relaxation and Dephasing section, these coherence measurements enabled extraction of flux noise amplitudes $A^{(A)} = 13.3$ $\mu\Phi_0$ and $A^{(B)} = 6.6$ $\mu\Phi_0$, as shown in Figure 46e and f. These values exceed previously measured flux noise levels (~1 $\mu\Phi_0$) in our experimental systems, which we

attribute to residual gallium ions and substrate degradation in the immediate qubit vicinity from focused ion beam processing.

At the optimal point, the decay rate due to second order flux noise (see Equation 82) is given by $\Gamma_{2,E}^{\Phi,(2)} = \frac{57.6}{\Delta/2\pi}\left(\frac{I_p A_{\varphi,E}^{\Phi}}{h}\right)^2$ which equals 262 (58) kHz for qubit A (B). These values exceed the estimated photon noise $\Gamma_{\varphi}^{\bar{n}} = 13\ (3)$ Hz and charge noise $\Gamma_{\varphi}^{C} = 3.203\ (4.281)$ kHz. Therefore, we conclude that flux noise is the dominant decoherence mechanism also at the optimal point.

5.3 Gradiometer Design Validation

Gradiometers suppress uniform magnetic field fluctuations by using two loops with opposite orientations, making them sensitive only to field gradients. This design principle requires precise fabrication to achieve the necessary loop area matching and proper geometric alignment.

The total magnetic flux threading each gradiometer loop combines contributions from two distinct sources according to $\Phi_{t/b} = \Phi_{bias} + \Phi_{ext}$, where $\Phi_{bias} = MI_{DC}/2$ represents flux from bias current in the Bragg resonator transmission line and $\Phi_{ext} = AB_{ext}\cos(\theta_0)$ accounts for external field coupling with A representing the loop area, B_{ext} the external field strength, and θ_0 the angle between the field and loop normal. In experimental conditions, perfect alignment between the sample and external coil is practically impossible, introducing systematic errors that must be accounted for in the differential flux calculation. Consequently, the gradiometer differential flux becomes $\Phi_d = MI_{DC} + \delta AB_{ext}\cos(\theta_0 + \delta\theta)$, where δA represents the inevitable area difference between the two loops and $\delta\theta$ accounts for sample misalignment. For small misalignment angles the cosine term can be approximated as $\cos(\theta_0 + \delta\theta) \approx \cos(\theta_0) - \delta\theta\sin(\theta_0)$ and the differential flux takes the form of $\Phi_d = MI_{DC} + \delta AB_{ext}[\cos(\theta_0) - \delta\theta\sin(\theta_0)]$.

We validated the gradiometer architecture through systematic characterization under controlled external magnetic fields. The validation protocol employed the superconducting coil system described in the Experimental System chapter to generate controlled magnetic fields with both perpendicular and parallel orientations relative to the substrate surface. Sample positioning within the coil enabled application of both perpendicular and parallel

magnetic field orientations relative to the substrate surface, as illustrated in Figure 47a and b respectively.

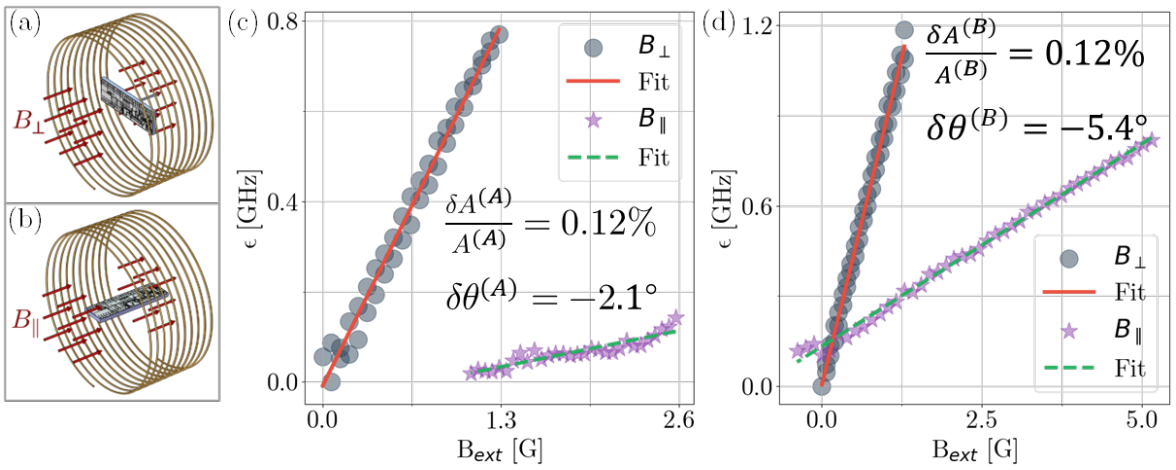

Figure 47 – Gradiometer functionality validation under controlled external magnetic fields | (a,b) Schematic illustrations showing sample orientations for perpendicular ($B_\perp$) and parallel ($B_\parallel$) magnetic field application relative to substrate surface. (c,d) Experimental data and theoretical fits demonstrating gradiometer operation with loop area differences $\delta A/A = 0.12 \pm 0.002\%$ for both qubits. Misalignment angles $\delta\theta^{(A)} = -2.09 \pm 0.03°$ and $\delta\theta^{(B)} = -5.42 \pm 0.06°$ reflect variations in the magnetic field due to the superconducting surface of the chip.

We measured qubit transition frequencies ω_{qb} as functions of external magnetic field to extract the magnetic flux response of each gradiometer loop. The qubit energy offset from the optimal point follows $\epsilon = \sqrt{\omega_{qb}^2 - \Delta^2}$, where Δ represents the energy splitting at zero flux bias.

Figure 47c (d) presents systematic measurements of qubit A (B) with perpendicular ($B_\perp, \theta_0 = 0°, \Phi_d = MI_{DC} + \delta AB_{ext}$) and parallel magnetic fields ($B_\parallel, \theta_0 = 90°, \Phi_d = MI_{DC} - \delta AB_{ext}\delta\theta$). In the perpendicular configuration, the external field couples maximally to both gradiometer loops, making the measurement sensitive to loop area differences δA.

We performed fits to the frequency shift versus field strength data based on equation 38. The perpendicular field measurements for qubit A and qubit B yielded a linear response with slope corresponding to $\frac{\delta A^{(A)}}{A^{(B)}} = \frac{\delta A^{(A)}}{A^{(B)}} = 0.12 \pm 0.002\%$. Here, $A^{(i)}$ is the designed area of qubit i. This result represents a suppression factor of ~800 compared to single-loop devices, significantly reducing sensitivity to homogeneous magnetic fields.

In parallel orientation, the external field should not be coupled to properly aligned gradiometer loops, making the measurement sensitive to the angular misalignment $\delta\theta$.

Systematic fitting of parallel field data revealed misalignment angles of $\delta\theta^{(A)} = -2.09 \pm 0.03°$ and $\delta\theta^{(B)} = -5.42 \pm 0.06°$. We believe these results stem from repulsion of magnetic fields from the superconducting surfaces on the chip.

The comprehensive validation establishes that the gradiometer design achieves its intended functionality of suppressing uniform magnetic field noise while maintaining sensitivity to local flux bias control. The measured fabrication precision and geometric accuracy support the viability of this approach for quantum computing applications requiring enhanced magnetic field immunity.

5.4 Randomized Benchmarking

We evaluated gate performance using randomized benchmarking (RB) protocols to characterize average gate fidelities and identify dominant error sources. Randomized benchmarking provides a robust method for measuring gate performance by averaging over random sequences of quantum operations, thereby isolating systematic errors from state preparation and measurement errors.

5.4.1 Standard Randomized Benchmarking

We characterized the average gate fidelity across the complete Clifford gate set at the optimal flux point. Our protocol generated 25 random sequences of varying lengths, with each sequence containing m Clifford operations followed by an inverse operation to return the qubit to its initial state. We varied the sequence length m from 1 to 200 operations and repeated each measurement 400 times to achieve statistical precision.

The experimental protocol proceeded as follows: (1) initialize the qubit in the ground state, (2) apply a random sequence of m Clifford gates, (3) apply the inverse sequence to return to the ground state, and (4) measure the final qubit state. The sequence fidelity F(m) follows the decay model $F(m) = Ap^m + B$, where p represents the depolarizing parameter, A accounts for measurement contrast, and B represents the background offset.

Figure 48a shows results for qubit A, yielding a depolarizing parameter $p^{(A)} = 0.967 \pm 1 \times 10^{-3}$. Figure 48b presents qubit B results with $p^{(B)} = 0.974 \pm 1 \times 10^{-3}$. We converted these values to average gate error rates using $r_g/1.875 = (1 - p)/2$, accounting for the fact

that each Clifford operation requires 1.875 primitive gates on average. This analysis yielded average gate error rates of $r_g^{(A)} = 0.009 \pm 1 \times 10^{-3}$ and $r_g^{(B)} = 0.0069 \pm 4 \times 10^{-4}$.

To assess whether decoherence limits gate performance, we calculated the expected error rate from pure dephasing: $r^* \sim t_{pulse}\Gamma_\phi$, where $\Gamma_\phi = \Gamma_{2,E} - \frac{1}{2}\Gamma_1$ represents the pure dephasing rate. For qubit A with 100 ns gates, $r^{*,(A)} = 0.007$, while qubit B with 16 ns gates yields $r^{*,(B)} = 0.003$. The measured error rates exceed these decoherence-limited values, indicating that control errors rather than decoherence dominate gate infidelity at the optimal point.

The higher error rate for qubit B despite shorter gate times results from increased sensitivity to control parameter fluctuations. Short, high-amplitude pulses exhibit greater sensitivity to amplitude and frequency errors, explaining why qubit B shows reduced gate fidelity compared to the longer-pulse operation of qubit A.

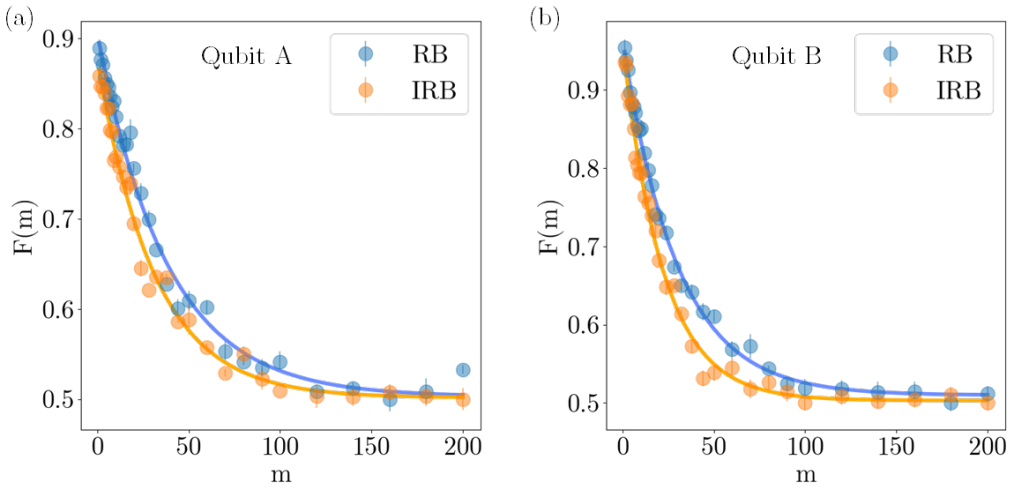

*Figure 48 – Randomized benchmarking at the optimal point | Average Clifford set fidelity F(m) as a function of sequence length m for **(a)** qubit A and **(b)** qubit B. Blue circles represent standard randomized benchmarking (RB) experiments measuring composite Clifford gate performance, while orange triangles show interleaved randomized benchmarking (IRB) results isolating individual $X_{\pi/2}$ gate fidelity. The exponential decay model (solid lines) yields depolarizing parameters $p^{(A)} = 0.967$ (qubit A) and $p^{(B)} = 0.974$ (qubit B) for RB, corresponding to average gate error rates $r_g^{(A)} = 0.009$ and $r_g^{(B)} = 0.0069$ respectively. IRB measurements give individual $X_{\pi/2}$ gate errors of $r_{gate}^{(A)} = 0.006$ and $r_{gate}^{(B)} = 0.003$.*

5.4.2 Interleaved Randomized Benchmarking

We characterized individual gate performance using interleaved randomized benchmarking (IRB). This protocol follows the standard RB procedure but inserts a specific gate ($X_{\pi/2}$ in our

case) after each random Clifford operation. Comparing IRB and RB decay rates isolates the fidelity of the interleaved gate.

The IRB protocol yielded depolarizing parameters of $p_{gate}^{(A)} = 0.955 \pm 2 \times 10^{-3}$ for qubit A and $p_{gate}^{(B)} = 0.968 \pm 2 \times 10^{-3}$ for qubit B. We extracted individual $X_{\pi/2}$ gate error rates of $r_{gate}^{(A)} = 0.006 \pm 1 \times 10^{-3}$ and $r_{gate}^{(B)} = 0.003 \pm 1 \times 10^{-3}$. These values fall within the theoretical bounds [0, 0.032] and [0, 0.033] respectively, as established by the IRB formalism (see Equation 98).

The $X_{\pi/2}$ gate fidelities approach the decoherence limit calculated above, indicating that individual pulse errors primarily stem from decoherence rather than control imperfections. This contrasts with the composite Clifford operations, where control errors become more significant due to error accumulation across multiple primitive gates.

5.4.3 Decoherence And Gate Performance

We investigated the transition between control-limited and decoherence-limited regimes by operating qubits away from the optimal flux point. Magnetic flux bias reduces coherence times, as demonstrated in Figure 46, allowing systematic study of gate performance versus decoherence rates.

Figure 49a presents average gate error rates versus the product $t_{pulse}\Gamma_\phi$ for both qubits.

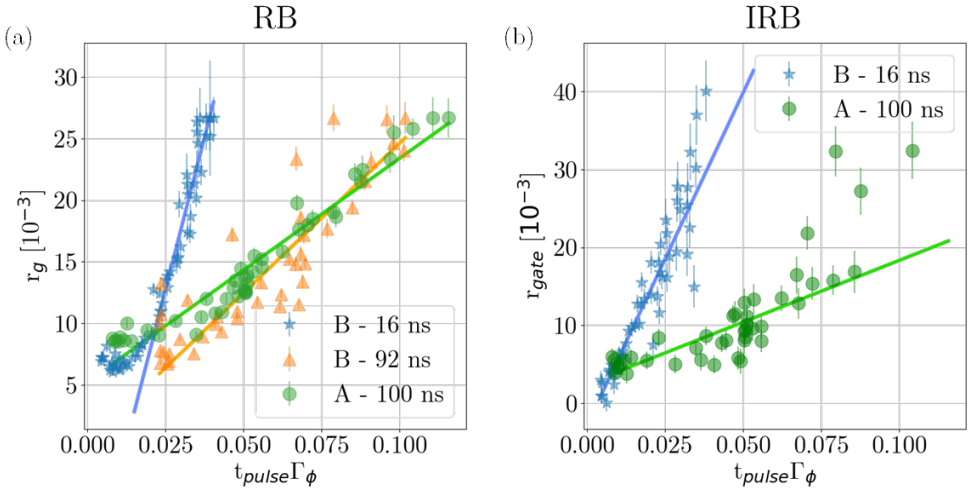

Figure 49 – Effect of decoherence on gate fidelity through flux bias detuning | Average gate error rates from randomized benchmarking experiments versus the product $t_{pulse}\Gamma_\phi$ for different pulse durations and detuning conditions. (a) Standard RB results showing the transition from control-limited to decoherence-limited regimes. For qubit A (green circles, $t_{pulse} = 100\,ns$), gate errors remain constant below $t_{pulse}\Gamma_\phi \approx 0.025$, indicating control parameter uncertainties dominate

performance. Above this threshold, errors increase linearly with proportionality constant $\alpha = 0.18$. Qubit B shows similar behavior with $\alpha = 0.24$ for 92 ns pulses (orange triangles) and $\alpha = 0.99$ for 16 ns pulses (blue stars). (b) Interleaved RB results for individual $X_{\pi/2}$ gates showing decoherence-limited behavior across all measured ratios. Linear fits yield $\alpha = 0.16$ (qubit A, 100 ns) and $\alpha = 0.85$ (qubit B, 16 ns). The smaller proportionality constants compared to composite Clifford operations reflect the reduced complexity of single-gate sequences.

Two distinct regimes emerge:

Decoherence-limited regime ($t_{pulse}\Gamma_\phi > 0.025$): Gate errors increase linearly with the product $t_{pulse}\Gamma_\phi$ according to $r_g = \alpha t_{pulse}\Gamma_\phi + c$. We measured proportionality constants $\alpha = 0.259 \pm 0.007$ (qubit A, 100 ns pulses), $\alpha = 0.251 \pm 0.008$ (qubit B, 92 ns pulses), and $\alpha = 0.99 \pm 0.08$ (qubit B, 16 ns pulses).

Constant fidelity regime ($t_{pulse}\Gamma_\phi < 0.025$): Gate errors remain approximately constant despite varying coherence times. Control parameter uncertainties (amplitude, frequency, phase) dominate the error budget. The error floor reflects systematic imperfections in pulse calibration and environmental stability. Moreover, we believe that in this regime 1/f noise is dominant. Subsequently, the assumption that errors do not depend on the gate position in the sequence (that is, time dependent) is not valid. This can affect the RB model and results.

The transition occurs when the product of pulse length and recoherence rate become comparable to 0.025. Below this threshold, gates complete before significant decoherence occurs, and control errors dominate. Above this threshold, decoherence during gate execution becomes the primary error source.

Figure 49b shows IRB results, where $X_{\pi/2}$ gate errors exhibit decoherence-limited behavior across all measured ratios. Linear fits yield $\alpha = 0.16 \pm 0.02$ (qubit A, 100 ns) and $\alpha = 0.85 \pm 0.04$ (qubit B, 16 ns). The smaller proportionality constants compared to composite Clifford operations reflect lower sensitivity of the $X_{\pi/2}$ gate compared to the average sensitivity of the entire set used to construct the Clifford group.

The counterintuitive result that shorter pulses show greater sensitivity to decoherence arises from the averaging effect of longer gate sequences. During RB experiments, qubits undergo random rotations on the Bloch sphere, effectively averaging over static field inhomogeneities and low-frequency noise sources. This averaging mechanism resembles dynamical decoupling sequences like Hahn-Echo experiments.

Longer pulse durations provide extended averaging windows, reducing the impact of noise. Conversely, short pulses cannot average over noise fluctuations occurring on comparable time scales, leading to increased sensitivity to decoherence effects.

The analysis reveals three primary error sources: (1) systematic control errors affecting all gates, (2) decoherence during gate execution, and (3) noise averaging effects that depend on gate duration. Understanding these mechanisms enables targeted improvements through enhanced control calibration, reduced gate times, and optimized pulse shapes that minimize sensitivity to environmental fluctuations.

6. Conclusion

6.1 Summary of Research Contributions

The central challenge addressed by this dissertation was the architectural realization of a hybrid mechanical-superconducting quantum processor. The primary thesis posited that by successfully coupling a high-coherence mechanical resonator to a superconducting flux qubit, one could establish a powerful platform for quantum transduction and computation. The work detailed herein has successfully laid the experimental and theoretical groundwork for this goal, culminating in three significant, self-contained contributions.

First, we demonstrated the successful fabrication and preparatory characterization of the two key, disparate components required for the hybrid system: diamond nanobeams and silicon membranes (mechanical resonators) and the gradiometer flux qubit architecture (superconducting element).

Second, we achieved the first experimental realization of a gradiometer flux qubit integrated with cQED readout. Crucially, this architecture delivered a new benchmark in coherence: our qubits exhibited a low relaxation rate ($\Gamma_1 = 33$ kHz) and the best-reported dephasing rate ($\Gamma_2 = 80$ kHz) for gradiometer flux qubits to date. This high coherence confirms the viability of the architecture for future quantum experiments.

Third, we performed a quantitative study, based on randomized benchmarking measurements, characterizing the relationship between single-qubit gate fidelity and coherence time. This investigation identified two distinct operational regimes: a coherence-dependent regime and a constant fidelity regime. The transition threshold between these two

was empirically determined ($t_{pulse}\Gamma_{\phi} = 0.025$), providing essential design guidance for optimizing gate operations in future processors.

6.2 Scientific Significance and Technological Impact

The results of this dissertation represent a substantial advancement in the development of hybrid superconducting architectures. The successful implementation of a gradiometer flux qubit utilizing cQED readout establishes a pioneering platform. The gradiometer, which senses a magnetic field gradient rather than a uniform field, is inherently more robust against common-mode magnetic noise, providing the critical stability needed for high-fidelity operations.

The record-setting coherence metrics achieved—specifically the dephasing rate—set a new standard of performance for gradiometer flux qubits. This is pivotal, as the gradiometer design is essential for achieving the required magnetic coupling to the mechanical resonator, which is the ultimate goal of the hybrid system.

Furthermore, the architecture's intrinsic ability to hinder qubit-qubit crosstalk marks a significant step towards scalability. By mitigating parasitic interactions between neighboring qubits, the gradiometer design addresses one of the most persistent and difficult challenges in building multi-qubit processors. Our findings confirm that this system is not merely a path to quantum transduction but also an intrinsically superior architectural choice for larger-scale superconducting quantum circuit integration.

6.3 Limitations and Caveats

While the experimental demonstration of high-coherence gradiometer flux qubits is robust, the current work is subject to specific constraints. The conclusions regarding qubit performance are derived from measurements of a relatively small number of qubits, which limits the statistical generalization of the results across fabrication batches.

A significant experimental caveat stems from the dominant environmental noise, where the system performance was primarily limited by 1/f flux noise. This noise source remains the principal constraint on ultimate coherence. Additionally, the standard randomized

benchmarking model used for gate characterization does not intrinsically account for or filter the effects of this dominant 1/f noise, meaning the characterized gate error may not fully isolate the noise-independent performance of the underlying quantum gates.

6.4 Outlook and Future Research Trajectories

The successful foundation established by this research immediately suggests several high-impact research directions that are both concrete and actionable:

Refined Gradiometer Design and Noise Mitigation: The most immediate and critical future step is to develop and test an improved gradiometer design that removes the necessity of Focused Ion Beam fabrication steps. Eliminating this process is projected to substantially reduce materials-related defects and intrinsic flux noise, pushing the coherence limits even further toward the coherence-independent regime.

Integration and Demonstration of Hybrid Coupling: The logical next phase is the execution of the primary thesis goal: the direct integration of the high-coherence gradiometer flux qubit with the prepared mechanical resonators. This requires demonstrating and characterizing the coherent quantum coupling between the superconducting and mechanical degrees of freedom, the fundamental building block of a quantum transducer.

Advanced Metrology for 1/f Noise: New experimental protocols should be implemented to more accurately characterize gate fidelity under non-Markovian noise conditions. Specifically, applying advanced quantum metrology techniques that explicitly model or filter the effects of the dominant 1/f noise will provide a clearer picture of the intrinsic gate error, leading to more targeted optimization strategies.

Multi-Qubit Processor Feasibility: Future work should leverage the crosstalk suppression the gradiometer architecture and focus on the design and experimental testing of a small-scale multi gradiometer flux qubit processor. This trajectory will directly explore the scalability advantages identified in this dissertation and validate the architecture's potential for complex quantum algorithms.

7. References

1. Schrödinger, E. Die gegenwärtige Situation in der Quantenmechanik. *Naturwissenschaften* **23**, 807–812 (1935).
2. Haroche, S. & Raimond, J.-M. *Exploring the Quantum: Atoms, Cavities, and Photons*. (Oxford University Press, 2006). doi:10.1093/acprof:oso/9780198509141.001.0001.
3. Leggett, A. J. Macroscopic Quantum Systems and the Quantum Theory of Measurement. *Prog. Theor. Phys. Suppl.* **69**, 80–100 (1980).
4. Poot, M. & van der Zant, H. S. J. Mechanical systems in the quantum regime. *Phys. Rep.* **511**, 273–335 (2012).
5. Vool, U. & Devoret, M. Introduction to quantum electromagnetic circuits. *Int. J. Circuit Theory Appl.* **45**, 897–934 (2017).
6. Arute, F. *et al.* Quantum supremacy using a programmable superconducting processor. *Nature* **574**, 505–510 (2019).
7. King, A. D. *et al.* Beyond-classical computation in quantum simulation. *Science* **388**, 199–204 (2025).
8. Gao, D. *et al.* Establishing a New Benchmark in Quantum Computational Advantage with 105-qubit Zuchongzhi 3.0 Processor. *Phys. Rev. Lett.* **134**, 090601 (2025).
9. Krantz, P. *et al.* A quantum engineer's guide to superconducting qubits. *Appl. Phys. Rev.* **6**, 021318 (2019).
10. Kjaergaard, M. *et al.* Superconducting Qubits: Current State of Play. *Annu. Rev. Condens. Matter Phys.* **11**, 369–395 (2020).
11. Siddiqi, I. Engineering high-coherence superconducting qubits. *Nat. Rev. Mater.* **6**, 875–891 (2021).

12. Ezratty, O. Perspective on superconducting qubit quantum computing. *Eur. Phys. J. A* **59**, 94 (2023).

13. Acharya, R. *et al.* Quantum error correction below the surface code threshold. *Nature* **638**, 920–926 (2025).

14. Gyenis, A. *et al.* Moving beyond the Transmon: Noise-Protected Superconducting Quantum Circuits. *PRX Quantum* **2**, 030101 (2021).

15. Lee, N. R. A. Strong Dispersive Coupling Between a Mechanical Resonator and a Fluxonium Superconducting Qubit. *PRX Quantum* **4**, (2023).

16. Catalini, L. Soft-Clamped Phononic Dimers for Mechanical Sensing and Transduction. *Phys. Rev. Appl.* **14**, (2020).

17. Gerashchenko, K. *et al.* Probing the quantum motion of a macroscopic mechanical oscillator with a radio-frequency superconducting qubit. Preprint at https://doi.org/10.48550/arXiv.2505.21481 (2025).

18. Seis, Y. *et al.* Ground state cooling of an ultracoherent electromechanical system. *Nat. Commun.* **13**, 1507 (2022).

19. Aspelmeyer, M., Kippenberg, T. J. & Marquardt, F. Cavity optomechanics. *Rev. Mod. Phys.* **86**, 1391–1452 (2014).

20. Penrose, R. On Gravity's role in Quantum State Reduction. *Gen. Relativ. Gravit.* **28**, 581–600 (1996).

21. Kippenberg, T. J. & Vahala, K. J. Cavity Optomechanics: Back-Action at the Mesoscale. *Science* **321**, 1172–1176 (2008).

22. Engelsen, N. J., Beccari, A. & Kippenberg, T. J. Ultrahigh-quality-factor micro- and nanomechanical resonators using dissipation dilution. *Nat. Nanotechnol.* **19**, 725–737 (2024).

23. Chu, Y. & Gröblacher, S. A perspective on hybrid quantum opto- and electromechanical systems. *Appl. Phys. Lett.* **117**, 150503 (2020).

24. Kini Manjeshwar, S. *et al.* Suspended photonic crystal membranes in AlGaAs heterostructures for integrated multi-element optomechanics. *Appl. Phys. Lett.* **116**, 264001 (2020).

25. Chu, Y. *et al.* Quantum acoustics with superconducting qubits. *Science* **358**, 199–202 (2017).

26. Franse, W. J. M., Potts, C. A., Bittencourt, V. A. S. V., Metelmann, A. & Steele, G. A. High-coherence quantum acoustics with planar superconducting qubits. *Appl. Phys. Lett.* **125**, 183501 (2024).

27. Wu, H. *et al.* Reducing intrinsic energy dissipation in diamond-on-diamond mechanical resonators toward one million quality factor. *Phys. Rev. Mater.* **2**, 090601 (2018).

28. Joe, G. *et al.* High Q-Factor Diamond Optomechanical Resonators with Silicon Vacancy Centers at Millikelvin Temperatures. *Nano Lett.* **24**, 6831–6837 (2024).

29. Naing, T. L., Rocheleau, T. O., Ren, Z., Li, S.-S. & Nguyen, C. T.-C. High- Q UHF Spoke-Supported Ring Resonators. *J. Microelectromechanical Syst.* **25**, 11–29 (2016).

30. Stockill, R. *et al.* Ultra-low-noise microwave to optics conversion in gallium phosphide. *Nat. Commun.* **13**, 6583 (2022).

31. Jiang, W. *et al.* Lithium niobate piezo-optomechanical crystals. *Optica* **6**, 845–853 (2019).

32. Bereyhi, M. J. *et al.* Hierarchical tensile structures with ultralow mechanical dissipation. *Nat. Commun.* **13**, 3097 (2022).

33. Rossi, M., Mason, D., Chen, J., Tsaturyan, Y. & Schliesser, A. Measurement-based quantum control of mechanical motion. *Nature* **563**, 53–58 (2018).

34. Guo, J. & Gröblacher, S. Integrated optical-readout of a high-Q mechanical out-of-plane mode. *Light Sci. Appl.* **11**, 282 (2022).

35. Ghadimi, A. H. *et al.* Elastic strain engineering for ultralow mechanical dissipation. *Science* **360**, 764–768 (2018).

36. Bereyhi, M. J. *et al.* Perimeter Modes of Nanomechanical Resonators Exhibit Quality Factors Exceeding ${10}^{9}$ at Room Temperature. *Phys. Rev. X* **12**, 021036 (2022).

37. Shin, D. *et al.* Spiderweb Nanomechanical Resonators via Bayesian Optimization: Inspired by Nature and Guided by Machine Learning. *Adv. Mater.* **34**, 2106248 (2022).

38. Reinhardt, C., Müller, T., Bourassa, A. & Sankey, J. C. Ultralow-Noise SiN Trampoline Resonators for Sensing and Optomechanics. *Phys. Rev. X* **6**, 021001 (2016).

39. Kermany, A. R. *et al.* Microresonators with Q-factors over a million from highly stressed epitaxial silicon carbide on silicon. *Appl. Phys. Lett.* **104**, 081901 (2014).

40. Borrielli, A. *et al.* Low-Loss Optomechanical Oscillator for Quantum-Optics Experiments. *Phys. Rev. Appl.* **3**, 054009 (2015).

41. MacCabe, G. S. *et al.* Nano-acoustic resonator with ultralong phonon lifetime. *Science* **370**, 840–843 (2020).

42. Wu, G., Xu, D., Xiong, B. & Wang, Y. High Q Single Crystal Silicon Micromechanical Resonators With Hybrid Etching Process. *IEEE Sens. J.* **12**, 2414–2415 (2012).

43. Beccari, A. *et al.* Strained crystalline nanomechanical resonators with quality factors above 10 billion. *Nat. Phys.* **18**, 436–441 (2022).

44. Elshaari, A. W., Pernice, W., Srinivasan, K., Benson, O. & Zwiller, V. Hybrid integrated quantum photonic circuits. *Nat. Photonics* **14**, 285–298 (2020).

45. Clerk, A. A., Lehnert, K. W., Bertet, P., Petta, J. R. & Nakamura, Y. Hybrid quantum systems with circuit quantum electrodynamics. *Nat. Phys.* **16**, 257–267 (2020).

46. Kubo, Y. *et al.* Hybrid Quantum Circuit with a Superconducting Qubit Coupled to a Spin Ensemble. *Phys. Rev. Lett.* **107**, 220501 (2011).

47. Blais, A., Huang, R.-S., Wallraff, A., Girvin, S. M. & Schoelkopf, R. J. Cavity quantum electrodynamics for superconducting electrical circuits: An architecture for quantum computation. *Phys. Rev. A* **69**, 062320 (2004).

48. Chan, J. *et al.* Laser cooling of a nanomechanical oscillator into its quantum ground state. *Nature* **478**, 89–92 (2011).

49. Teufel, J. D. *et al.* Sideband cooling of micromechanical motion to the quantum ground state. *Nature* **475**, 359–363 (2011).

50. Rocheleau, T. *et al.* Preparation and detection of a mechanical resonator near the ground state of motion. *Nature* **463**, 72–75 (2010).

51. Palomaki, T. A., Harlow, J. W., Teufel, J. D., Simmonds, R. W. & Lehnert, K. W. Coherent state transfer between itinerant microwave fields and a mechanical oscillator. *Nature* **495**, 210–214 (2013).

52. Muhonen, J. T., La Gala, G. R., Leijssen, R. & Verhagen, E. State Preparation and Tomography of a Nanomechanical Resonator with Fast Light Pulses. *Phys. Rev. Lett.* **123**, 113601 (2019).

53. Kotler, S. *et al.* Direct observation of deterministic macroscopic entanglement. *Science* **372**, 622–625 (2021).

54. Palomaki, T. A., Teufel, J. D., Simmonds, R. W. & Lehnert, K. W. Entangling Mechanical Motion with Microwave Fields. *Science* **342**, 710–713 (2013).

55. Marquardt, F., Chen, J. P., Clerk, A. A. & Girvin, S. M. Quantum Theory of Cavity-Assisted Sideband Cooling of Mechanical Motion. *Phys. Rev. Lett.* **99**, 093902 (2007).

56. Zhao, H., Chen, W. D., Kejriwal, A. & Mirhosseini, M. Quantum-enabled microwave-to-optical transduction via silicon nanomechanics. *Nat. Nanotechnol.* **20**, 602–608 (2025).

57. Chegnizadeh, M. *et al.* Quantum collective motion of macroscopic mechanical oscillators. *Science* **386**, 1383–1388 (2024).

58. Youssefi, A., Kono, S., Chegnizadeh, M. & Kippenberg, T. J. A squeezed mechanical oscillator with millisecond quantum decoherence. *Nat. Phys.* **19**, 1697–1702 (2023).

59. Blencowe, M. P. & Buks, E. Quantum analysis of a linear dc SQUID mechanical displacement detector. *Phys. Rev. B* **76**, 014511 (2007).

60. Etaki, S. *et al.* Motion detection of a micromechanical resonator embedded in a d.c. SQUID. *Nat. Phys.* **4**, 785–788 (2008).

61. Rodrigues, I. C., Bothner, D. & Steele, G. A. Coupling microwave photons to a mechanical resonator using quantum interference. *Nat. Commun.* **10**, 5359 (2019).

62. Schmidt, P. *et al.* Sideband-resolved resonator electromechanics based on a nonlinear Josephson inductance probed on the single-photon level. *Commun. Phys.* **3**, 233 (2020).

63. Zhong, H.-S. *et al.* Quantum computational advantage using photons. *Science* **370**, 1460–1463 (2020).

64. Chamberland, C. *et al.* Building a Fault-Tolerant Quantum Computer Using Concatenated Cat Codes. *PRX Quantum* **3**, 010329 (2022).

65. Pezzè, L., Smerzi, A., Oberthaler, M. K., Schmied, R. & Treutlein, P. Quantum metrology with nonclassical states of atomic ensembles. *Rev. Mod. Phys.* **90**, 035005 (2018).

66. Joo, J., Munro, W. J. & Spiller, T. P. Quantum Metrology with Entangled Coherent States. *Phys. Rev. Lett.* **107**, 083601 (2011).

67. Rabl, P. Photon Blockade Effect in Optomechanical Systems. *Phys. Rev. Lett.* **107**, 063601 (2011).

68. Liao, J.-Q., Huang, J.-F., Tian, L., Kuang, L.-M. & Sun, C.-P. Generalized ultrastrong optomechanical-like coupling. *Phys. Rev. A* **101**, 063802 (2020).

69. Dare, K. *et al.* Ultrastrong linear optomechanical interaction. *Phys. Rev. Res.* **6**, L042025 (2024).

70. Kurizki, G. *et al.* Quantum technologies with hybrid systems. *Proc. Natl. Acad. Sci.* **112**, 3866–3873 (2015).

71. LaHaye, M. D., Suh, J., Echternach, P. M., Schwab, K. C. & Roukes, M. L. Nanomechanical measurements of a superconducting qubit. *Nature* **459**, 960–964 (2009).

72. Schrieffer, J. R. & Wolff, P. A. Relation between the Anderson and Kondo Hamiltonians. *Phys. Rev.* **149**, 491–492 (1966).

73. Pirkkalainen, J.-M. Mechanical Resonators Coupled to Superconducting Circuits. (Aalto University, 2014).

74. Ma, X., Viennot, J. J., Kotler, S., Teufel, J. D. & Lehnert, K. W. Non-classical energy squeezing of a macroscopic mechanical oscillator. *Nat. Phys.* **17**, 322–326 (2021).

75. Koch, J. *et al.* Charge-insensitive qubit design derived from the Cooper pair box. *Phys. Rev. A* **76**, 042319 (2007).

76. Pirkkalainen, J.-M. *et al.* Hybrid circuit cavity quantum electrodynamics with a micromechanical resonator. *Nature* **494**, 211–215 (2013).

77. Rouxinol, F. *et al.* Measurements of nanoresonator-qubit interactions in a hybrid quantum electromechanical system. *Nanotechnology* **27**, 364003 (2016).

78. Manenti, R. *et al.* Circuit quantum acoustodynamics with surface acoustic waves. *Nat. Commun.* **8**, 975 (2017).

79. Chou, M.-H. *et al.* Deterministic multi-phonon entanglement between two mechanical resonators on separate substrates. *Nat. Commun.* **16**, 1450 (2025).

80. Wollack, E. A. *et al.* Quantum state preparation and tomography of entangled mechanical resonators. *Nature* **604**, 463–467 (2022).

81. Chu, Y. *et al.* Creation and control of multi-phonon Fock states in a bulk acoustic-wave resonator. *Nature* **563**, 666–670 (2018).

82. Hofheinz, M. *et al.* Synthesizing arbitrary quantum states in a superconducting resonator. *Nature* **459**, 546–549 (2009).

83. Mirrahimi, M. *et al.* Dynamically protected cat-qubits: a new paradigm for universal quantum computation. *New J. Phys.* **16**, 45014 (2014).

84. Leghtas, Z. *et al.* Hardware-efficient autonomous quantum memory protection. *Phys. Rev. Lett.* **111**, 120501 (2013).

85. Bild, M. *et al.* Schrödinger cat states of a 16-microgram mechanical oscillator. *Science* **380**, 274–278 (2023).

86. Blais, A., Huang, R. S., Wallraff, A., Girvin, S. M. & Schoelkopf, R. J. Cavity quantum electrodynamics for superconducting electrical circuits: An architecture for quantum computation. *Phys. Rev. - At. Mol. Opt. Phys.* **69**, 062320 (2004).

87. Paik, H. *et al.* Observation of high coherence in Josephson junction qubits measured in a three-dimensional circuit QED architecture. *Phys. Rev. Lett.* **107**, 240501 (2011).

88. Kirchmair, G. *et al.* Observation of quantum state collapse and revival due to the single-photon Kerr effect. *Nature* **495**, 205–209 (2013).

89. Nigg, S. E. *et al.* Black-box superconducting circuit quantization. *Phys. Rev. Lett.* **108**, 240502 (2012).

90. Schuster, D. I. *et al.* Resolving photon number states in a superconducting circuit. *Nature* **445**, 515–518 (2007).

91. Vlastakis, B. *et al.* Deterministically encoding quantum information using 100-photon Schrödinger cat states. *Science* **342**, 607–610 (2013).

92. Sun, L. *et al.* Tracking photon jumps with repeated quantum non-demolition parity measurements. *Nature* **511**, 444–448 (2014).

93. Ofek, N. *et al.* Extending the lifetime of a quantum bit with error correction in superconducting circuits. *Nature* **536**, 441–445 (2016).

94. Paauw, F. G., Fedorov, A., Harmans, C. J. P. M. & Mooij, J. E. Tuning the Gap of a Superconducting Flux Qubit. *Phys. Rev. Lett.* **102**, 090501 (2009).

95. Fedorov, A. *et al.* Strong Coupling of a Quantum Oscillator to a Flux Qubit at Its Symmetry Point. *Phys. Rev. Lett.* **105**, 060503 (2010).

96. Fedorov, A., Macha, P., Feofanov, A. K., Harmans, C. J. P. M. & Mooij, J. E. Tuned Transition from Quantum to Classical for Macroscopic Quantum States. *Phys. Rev. Lett.* **106**, 170404 (2011).

97. Schwarz, M. J. *et al.* Gradiometric flux qubits with a tunable gap. *New J. Phys.* **15**, 045001 (2013).

98. Bautze, T. *et al.* Superconducting nano-mechanical diamond resonators. *Carbon* **72**, 100–105 (2014).

99. Tao, Y., Boss, J. M., Moores, B. A. & Degen, C. L. Single-crystal diamond nanomechanical resonators with quality factors exceeding one million. *Nat. Commun.* **5**, 3638 (2014).

100. Li, X., Lekavicius, I., Noeckel, J. & Wang, H. Ultracoherent Gigahertz Diamond Spin-Mechanical Lamb Wave Resonators. *Nano Lett.* **24**, 10995–11001 (2024).

101. Dang, C. *et al.* Achieving large uniform tensile elasticity in microfabricated diamond. *Science* **371**, 76–78 (2021).

102. Yeheskel, O. & Gefen, Y. The effect of the α phase on the elastic properties of Si3N4. *Mater. Sci. Eng.* **71**, 95–99 (1985).

103. Hopcroft, M. A., Nix, W. D. & Kenny, T. W. What is the Young's Modulus of Silicon? *J. Microelectromechanical Syst.* **19**, 229–238 (2010).

104. Field, J. E. The mechanical and strength properties of diamond. *Rep. Prog. Phys.* **75**, 126505 (2012).

105. Murray, C. E. Material matters in superconducting qubits. *Mater. Sci. Eng. R Rep.* **146**, 100646 (2021).

106. Singiresu, S. R. *Mechanical Vibrations*. (Addison Wesley Boston, MA, 1995).

107. Judge, J. A., Photiadis, D. M., Vignola, J. F., Houston, B. H. & Jarzynski, J. Attachment loss of micromechanical and nanomechanical resonators in the limits of thick and thin support structures. *J. Appl. Phys.* **101**, 013521 (2007).

108. Tilli, M. *et al. Handbook of Silicon Based MEMS Materials and Technologies*. (Elsevier, 2020).

109. Ghaffari, S. *et al.* Quantum Limit of Quality Factor in Silicon Micro and Nano Mechanical Resonators. *Sci. Rep.* **3**, 3244 (2013).

110. Wu, G., Xu, D., Xiong, B. & Wang, Y. A high Q micromachined single crystal silicon bulk mode resonator with pre-etched cavity. *Microsyst. Technol.* **18**, 25–30 (2012).

111. Garrett, S. L. Membranes, Plates, and Microphones. in *Understanding Acoustics: An Experimentalist's View of Sound and Vibration* (ed. Garrett, S. L.) 283–330 (Springer International Publishing, Cham, 2020). doi:10.1007/978-3-030-44787-8_6.

112. Zalalutdinov, M. K. *et al.* Ultrathin Single Crystal Diamond Nanomechanical Dome Resonators. *Nano Lett.* **11**, 4304–4308 (2011).

113. Mooij, J. E. *et al.* Josephson Persistent-Current Qubit. *Science* **285**, 1036–1039 (1999).

114. Orlando, T. P. *et al.* Superconducting persistent-current qubit. *Phys. Rev. B* **60**, 15398–15413 (1999).

115. Bal, M., Deng, C., Orgiazzi, J.-L., Ong, F. R. & Lupascu, A. Ultrasensitive magnetic field detection using a single artificial atom. *Nat. Commun.* **3**, 1324 (2012).

116. Chang, T. *et al.* Reproducibility and Gap Control of Superconducting Flux Qubits. *Phys. Rev. Appl.* **18**, 064062 (2022).

117. Toida, H. *et al.* Electron paramagnetic resonance spectroscopy using a single artificial atom. *Commun. Phys.* **2**, 33 (2019).

118. Chang, T., Stern, M., Bar-Ilan University degree granting institution, & Bar-Ilan University. Department of Physics. Towards coupling superconducting flux qubits to single bismuth donors in silicon / Tikai Chang. (Bar-Ilan University, 2022).

119. Parker, D. J. Degenerate Parametric Amplification via Three-Wave Mixing Using Kinetic Inductance. *Phys. Rev. Appl.* **17**, (2022).

120. Stern, M. Introduction to Superconducting Quantum Circuits. in *New Trends and Platforms for Quantum Technologies* (eds. Aguado, R., Citro, R., Lewenstein, M. & Stern, M.) 61–132 (Springer Nature Switzerland, Cham, 2024). doi:10.1007/978-3-031-55657-9_2.

121. Knill, E. *et al.* Randomized benchmarking of quantum gates. *Phys. Rev. A* **77**, 012307 (2008).

122. Magesan, E., Gambetta, J. M. & Emerson, J. Scalable and Robust Randomized Benchmarking of Quantum Processes. *Phys. Rev. Lett.* **106**, 180504 (2011).

123. Gottesman, D. The Heisenberg Representation of Quantum Computers. Preprint at https://doi.org/10.48550/arXiv.quant-ph/9807006 (1998).

124. Aaronson, S. & Gottesman, D. Improved simulation of stabilizer circuits. *Phys. Rev. A* **70**, 052328 (2004).

125. Silva, A. & Greplova, E. Hands-on introduction to randomized benchmarking. *SciPost Phys. Lect. Notes* 097 (2025) doi:10.21468/SciPostPhysLectNotes.97.

126. Magesan, E. *et al.* Efficient Measurement of Quantum Gate Error by Interleaved Randomized Benchmarking. *Phys. Rev. Lett.* **109**, 080505 (2012).

127. Burek, M. J. *et al.* Free-Standing Mechanical and Photonic Nanostructures in Single-Crystal Diamond. *Nano Lett.* **12**, 6084–6089 (2012).

128. Göppl, M. *et al.* Coplanar waveguide resonators for circuit quantum electrodynamics. *J. Appl. Phys.* **104**, 113904 (2008).

129. Palacios-Laloy, A. Superconducting qubit in a resonator : test of the Leggett-Garg inequality and single-shot readout Agustín. *PhD Thesis* (2010).

130. Ridgeon, F. J. *et al.* Superconducting Properties of Titanium Alloys (Ti-64 and Ti-6242) for Critical Current Barrels. *IEEE Trans. Appl. Supercond.* **27**, 1–5 (2017).

131. Cohen, T. Tunable flux qubits with long coherence times. (Bar-Ilan University, 2021).

132. Reed, M. Entanglement and Quantum Error Correction with Superconducting Qubits. Preprint at https://doi.org/10.48550/arXiv.1311.6759 (2013).

8. Appendices

8.1 List of The Clifford Group Operations

1. I	7. $Y_{-\pi/2}$	13. $X_{\pi/2}Y_{\pi/2}$	19. $X_{\pi/2}Y_{\pi}$
2. X_{π}	8. $X_{\pi}Y_{\pi}$	14. $X_{-\pi/2}Y_{\pi/2}$	20. $X_{-\pi/2}Y_{\pi}$
3. Y_{π}	9. $Y_{\pi/2}X_{\pi/2}$	15. $X_{\pi/2}Y_{-\pi/2}$	21. $X_{\pi/2}Y_{\pi/2}X_{-\pi/2}$
4. $X_{\pi/2}$	10. $Y_{-\pi/2}X_{\pi/2}$	16. $X_{-\pi/2}Y_{-\pi/2}$	22. $X_{\pi/2}Y_{-\pi/2}X_{-\pi/2}$
5. $Y_{\pi/2}$	11. $Y_{\pi/2}X_{-\pi/2}$	17. $Y_{\pi/2}X_{\pi}$	23. $X_{\pi/2}Y_{\pi/2}X_{\pi/2}$
6. $X_{-\pi/2}$	12. $Y_{-\pi/2}X_{-\pi/2}$	18. $Y_{-\pi/2}X_{\pi}$	24. $X_{-\pi/2}Y_{\pi/2}X_{-\pi/2}$

8.2 Bragg Filter Simulation Python Script

```
# %% Imports
import numpy as np
```

```
from scipy.constants import constants

# $$ Functions
def phase_accumulation(omega, x, kappa, c):
    t = x / c
    return omega * t + 1j * kappa * t


def interface(z1, z2):
    r = (z2 - z1) / (z1 + z2)
    t = 2 * np.sqrt(z2 * z1) / (z1 + z2)
    return np.matrix(
        [[r, t],
         [t, -r]]
    )


def transmission_line(omega, L, kappa, c):
    phi = phase_accumulation(omega, L, kappa, c=c)
    r = 0
    t = np.exp(1j * phi)
    return np.matrix(
        [[r, t],
         [t, r]]
    )


def two_elements_chain(s1, s2):
    r1_backward = s1.A[0][0]
    r1_forward = s1.A[1][1]

    t1_backward = s1.A[0][1]
    t1_forward = s1.A[1][0]
```

```
    r2_backward = s2.A[0][0]
    r2_forward = s2.A[1][1]

    t2_backward = s2.A[0][1]
    t2_forward = s2.A[1][0]

    r_backward = r1_backward + (t1_forward * t1_backward *
r2_backward) / (1 - r1_forward * r2_backward)
    r_forward = r2_forward + (t2_backward * t2_forward *
r1_forward) / (1 - r1_forward * r2_backward)

    t_forward = (t1_forward * t2_forward) / (1 - r1_forward *
r2_backward)
    t_backward = (t2_backward * t1_backward) / (1 - r1_forward
* r2_backward)
    return np.matrix(
        [[r_backward, t_backward],
         [t_forward, r_forward]]
    )


def bragg_filter(omega, L, z1, z2, m, z0=50, kappa=0,
c=constants.c):
    phi = transmission_line(omega, L, kappa, c)
    n = 2 * m - 1
    for i in range(n):
        s_temp = (-1)**i * two_elements_chain(phi,
interface(z1, z2))

        if i == 0:
            s = two_elements_chain(interface(z0, z1), s_temp)
        else:
            s = two_elements_chain(s, s_temp)
```

```
    s = two_elements_chain(s, phi)
    return two_elements_chain(s, interface(z2, z0))


# %% Si parameters
epsilon_Si = 11.7
epsilon_r = (1 + epsilon_Si) / 2
c_eff = constants.c / np.sqrt(epsilon_r)

# %% Bragg parameters
m_doublets = 4  # range(1, 13)  # Number of l-h doublets
Z_l = 35  # Ohm
Z_h = 80  # Ohm
L_bragg = 3438e-6  # m

wl_Bragg = L_bragg * 4  # m
f_Bragg = c_eff / wl_Bragg  # Hz
# %% Bragg-CPW-short
omega = np.linspace(0.2 * 2 * np.pi * f_Bragg, 1.8 * 2 * np.pi
* f_Bragg, 1001, endpoint=True)

r_tot, t_tot = [], []

r_Bragg, r_prime_Bragg, t_Bragg = [], [], []

r_CPW, t_CPW = [], []

r_Short, t_Short = [], []

for omega_ in omega:
    bragg = bragg_filter(omega_, L_bragg, Z_l, Z_h,
m_doublets, c=c_eff)

    r_Bragg.append(bragg.A[0][0])
```

```
r_prime_Bragg.append(bragg.A[1][1])
t_Bragg.append(bragg.A[1][0])
```

8.3 List of Publications

1. Holzman, I., Chang, T., George, N., Ginossar, E. & Stern, M. (2025). Gradiometer flux qubit in circuit QED architecture. *Under preparation*.
2. Chang, T., Holzman, I., Lim, S. Q., Holmes, D., Johnson, B. C., Jamieson, D. N., & Stern, M. (2024). Strong coupling of a superconducting flux qubit to single bismuth donors. *arXiv preprint arXiv:2411.02852*.
3. Chelly, R. A., Chang, T., Holzman, I., Cohen, T., Kantorovitsch, J., & Stern, M. (2023). Variance properties of the microwave absorption spectrum of an ensemble of nitrogen vacancy centers in diamond. *Europhysics Letters*, *144*(5), 56002.
4. Chang, T., Cohen, T., Holzman, I., Catelani, G., & Stern, M. (2023). Tunable superconducting flux qubits with long coherence times. *Physical Review Applied*, *19*(2), 024066.
5. Chang, T., Holzman, I., Cohen, T., Johnson, B. C., Jamieson, D. N., & Stern, M. (2022). Reproducibility and gap control of superconducting flux qubits. *Physical Review Applied*, *18*(6), 064062.

תקציר

חקר תופעות קוונטיות מקרוסקופיות הוא גבול מרתק בפיזיקה המודרנית, שמניע הן חקירות יסודיות של טבע מכניקת הקוונטים והן פיתוח טכנולוגיות קוונטיות חדשניות. בעוד שקיוביטים על-מוליכים הגיחו כפלטפורמה מובילה למחשוב קוונטי בזכות פעולתם המהירה וצימודם החזק לשדות מיקרוגל, הם מתמודדים עם מגבלות כמו זמני קוהרנטיות קצרים ודיבור צולב. לעומת זאת, מהודים מכניים מציעים תכונות קוהרנטיות יוצאות דופן, עם גורמי איכות שלרוב עולים על 10^6. עם זאת, הליניאריות המובנית שלהם והצימוד החלש לשדות בקרה חיצוניים מציבים אתגרים משמעותיים לשימוש בהם כקיוביטים. מערכות קוונטיות היברידיות, המשלבות את היתרונות המשלימים של פלטפורמות פיזיות שונות תוך מזעור המגבלות האישיות שלהן, מציעות פתרון מבטיח לאתגרים אלה.

עבודת גמר זו מציגה גישה חדשנית למימוש מערכת קוונטית היברידית על ידי הצעה של אינטראקציות חדשניות בתיווך שטף מגנטי בין קיוביטי שטף על-מוליכים למהודים מכניים. אנו מציעים תוכנית צימוד המשלבת קיוביטי שטף על-מוליכים בתצורת גרדיומטר עם מהודים מכניים דרך אינטראקציות של שטף מגנטי תחת שדות מגנטיים מקבילים. גישה זו עוקפת את מגבלות הצימוד של מערכות אופטו-מכניות ואלקטרו-מכניות קונבנציונליות על ידי ניצול הרגישות המשופרת של קיוביטי השטף, תוך מינוף תכונות הקוהרנטיות יוצאות הדופן של המהודים המכניים. העבודה מתחילה בתכנון וייצור של מהודים מכניים באיכות גבוהה תוך שימוש הן בממברנות סיליקון והן בננו-קורות יהלום. כדי להתחבר ביעילות למהודים אלו, פותח קיוביט שטף בתצורת גרדיומטר, שכן תכנונו מבטל את ההשפעות המזיקות של שדות מגנטיים אחידים שיכולים להפריע למנגנון הצימוד. מכיוון שתצורת הגרדיומטר של הקיוביט הופך אותו ללא רגיש לשדות מגנטיים חיצוניים אחידים, לא ניתן למגנט אותו באמצעות סליל חיצוני. לכן, פיתחנו מהוד שמסתיים בסורג בראג (Bragg) המאפשר יישום זרם ישר עבור יצירת שטף מגנטי מקומי, ובכך מאפשר את המגנוט של הקיוביט.

עם רכיבים אינדיבידואליים אלה שיוצרו ואופיינו, ליבת המחקר כוללת הדגמה של מנגנון אינטראקציה חזק בין קיוביטי השטף לבין המהודים שהסתיימו בסורג בראג. באמצעות מדידות ספקטרוסקופיות שיטתיות, חולצו עוצמות צימוד של כ-20 מגה-הרץ, מה שמדגים צימוד חזק בין שתי המערכות. קיוביטי השטף הראו פעולה קוהרנטית קוונטית עם זמני הרפיה של עד 30 מיקרו-שניות וזמני קוהרנטיות (echo) של עד 12 מיקרו-שניות. המגבלה העיקרית זוהתה כרעש שטף המיוחס לזיהום שנגרם כתוצאה מהייצור של הקיוביט וצימוד לקו תמסורת ישיר.

בעוד שהצימוד הניסיוני מהוד מכני לקיוביט שטף לא הודגם, הרכיבים הבודדים והמסגרת התיאורטית מקימים את הבסיס ליישום מערכות קוונטיות היברידיות שיוכלו למנף את הקוהרנטיות המעולה של מהודים מכניים תוך מתן אפשרות להנדסת מצב קוונטי לא ליניארית באמצעות קיוביטי שטף על-מוליכים.

תוכן עניינים

עבודה זו נעשתה בהדרכתו של

ד"ר מיכאל שטרן

מן המחלקה לפיזיקה של אוניברסיטת בר-אילן

לקראת צימוד של מהוד מכאני עם קיוביט שטף מוליך-על

חיבור לשם קבלת התואר "דוקטור לפילוסופיה"

מאת:

איתמר הולצמן

המחלקה לפיזיקה

הוגש לסנט של אוניברסיטת בר-אילן

רמת גן תשרי, תשפ"ו